

REPORT DOCUMENTATION PAGE

Form Approved
OMB No. 0704-0188

Public reporting burden for this collection of information is estimated to average 1 hour per response, including the time for reviewing instructions, searching existing data sources, gathering and maintaining the data needed, and completing and reviewing the collection of information. Send comments regarding this burden estimate or any other aspect of this collection of information, including suggestions for reducing this burden, to Washington Headquarters Services, Directorate for Information Operations and Reports, 1215 Jefferson Davis Highway, Suite 1204, Arlington, VA 22202-4302, and to the Office of Management and Budget, Paperwork Reduction Project (0704-0188), Washington, DC 20503.

1. AGENCY USE ONLY (Leave blank)	2. REPORT DATE <i>May 95</i>	3. REPORT TYPE AND DATES COVERED
----------------------------------	---------------------------------	----------------------------------

4. TITLE AND SUBTITLE <i>Observations of Supersonic Flat Plate Noses</i>	5. FUNDING NUMBERS
---	--------------------

6. AUTHOR(S) <i>Michael Francis Smith</i>
--

7. PERFORMING ORGANIZATION NAME(S) AND ADDRESS(ES) AFIT Students Attending: <i>Texas - Austin</i>	8. PERFORMING ORGANIZATION REPORT NUMBER <i>95-147</i>
---	---

9. SPONSORING / MONITORING AGENCY NAME(S) AND ADDRESS(ES) DEPARTMENT OF THE AIR FORCE AFIT/CI 2950 P STREET, BLDG 125 WRIGHT-PATTERSON AFB OH 45433-7765	10. SPONSORING / MONITORING AGENCY REPORT NUMBER
--	--

11. SUPPLEMENTARY NOTES

12a. DISTRIBUTION / AVAILABILITY STATEMENT Approved for Public Release IAW AFR 190-1 Distribution Unlimited BRIAN D. Gauthier, MSgt, USAF Chief Administration	12b. DISTRIBUTION CODE
--	------------------------

13. ABSTRACT (Maximum 200 words)

19960124 069

14. SUBJECT TERMS	15. NUMBER OF PAGES <i>101</i>
	16. PRICE CODE

17. SECURITY CLASSIFICATION OF REPORT	18. SECURITY CLASSIFICATION OF THIS PAGE	19. SECURITY CLASSIFICATION OF ABSTRACT	20. LIMITATION OF ABSTRACT
---------------------------------------	--	---	----------------------------

© Copyright by Michael Francis Smith 1995

All rights reserved

**OBSERVATIONS OF SUPERSONIC
FLAT PLATE WAKES**

by

Michael Francis Smith, B.S.

Thesis

Presented to the Faculty of the Graduate School
of the University of Texas at Austin
in Partial Fulfillment
of the Requirements
for the Degree of

Master of Science in Engineering

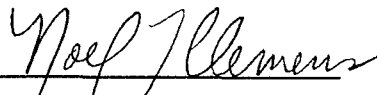
The University of Texas at Austin

May 1995

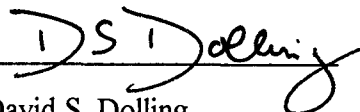
**OBSERVATIONS OF SUPERSONIC
FLAT PLATE WAKES**

APPROVED BY

SUPERVISING COMMITTEE:



Noel T. Clemens



David S. Dolling

DEDICATION

This thesis is dedicated to my wife Karen. Her endless patience and love through this undertaking was immeasurable. She is truly a crown jewel.

ACKNOWLEDGMENTS

The people who contributed to this research were: Eric Lachney, who designed the test section of the wind tunnel, Thomas Sanders and John Fernandez, who designed the pressure measurement system, and Noel Clemens whose guidance helped turn moments of confusion into clarity.

ABSTRACT

OBSERVATIONS OF SUPERSONIC FLAT PLATE WAKES

by

Michael Francis Smith, M.S.E.

The University of Texas at Austin, 1995

SUPERVISOR: Noel T. Clemens

Observations were made of supersonic flat plate wakes at Mach 3 for both initially laminar and turbulent boundary layer cases by using planar laser Mie scattering. These were then compared with pitot probe and side wall pressure measurements of the wake. Flow visualization experiments included side, plan and end views of the wake.

The laminar case generated a supersonic laminar wake that showed an extremely detailed large scale structure including spanwise and streamwise vorticity. Instabilities in the wake caused transition to occur which resulted in the breakdown of the large structure. Due to refraction of the images, only far end views were possible looking upstream, while the side and plan views include both far and close up views. The observations confirmed results seen for the incompressible case and have striking similarities. The observations also confirmed numerical predictions for the supersonic laminar case. The turbulent case showed no large scale structure anywhere in the wake and was observed to be completely random.

TABLE OF CONTENTS

List of Tables.....	ix
List of Figures	x
List of Symbols.....	xv
List of Abbreviations	xvii
Chapter 1: INTRODUCTION	1
1.1 Background and Motivation.....	1
1.2 Literature Survey	1
1.2.1 Categories of Wakes	2
1.2.2 Transition	3
1.2.3 Regions of the Wake	6
1.2.4 Incompressible Wakes	6
1.2.5 Compressible Wakes	12
Chapter 2: PLMS THEORY	16
2.1 Mie Theory	16
2.2 Condensation and Evaporation	19
2.3 Particle Size: An Issue	20
Chapter 3: EXPERIMENTAL FACILITY AND PROCEDURE	22
3.1 Wind Tunnel	22
3.1.1 Overall Design	22
3.1.2 Test Section	22
3.2 Pressure Measurements.....	25
3.2.1 Side Wall Pressure Measurement Set-up and Procedure.....	25

3.2.2 Pitot Probe Set-up and Procedure	26
3.3 PLMS Set-up and Procedure	27
3.4 Image Processing	30
Chapter 4: EXPERIMENTAL RESULTS AND DISCUSSION	33
4.1 Pressure Measurements	33
4.1.1 Side Wall Pressure Measurements	34
4.1.2 Pitot Probe Measurements	35
4.1.2.1 Boundary Layer Pressure Measurements	35
4.1.2.2. Wake Measurements	36
4.2 PLMS	38
4.2.1 Low Re	39
4.2.1.1 Side View Images	39
4.2.1.2 Plan View Images	43
4.2.1.3 End View Images	46
4.2.2 High Re	47
4.2.2.1 Side View Images	47
4.2.2.2 Plan View Images	48
4.2.2.3 End View Images	48
Chapter 5: CONCLUSION	49
BIBLIOGRAPHY	99
VITA	101

LIST OF TABLES

Table 1	Low Re case with $U_{\infty} = 612$ m/s and $a_{\infty} = 203$ m/s	51
Table 2	High Re case with $U_{\infty} = 635$ m/s and $a_{\infty} = 190$ m/s	51

LIST OF FIGURES

Figure 1.1	Stability of a ball	52
Figure 1.2	Illustration of the vortices in the Kelvin-Helmholtz instability theory. Side view of the plate	52
Figure 1.3	Mean velocity profiles of a laminar flat plate wake	53
Figure 1.4	Vorticity of a laminar flat plate wake	53
Figure 1.5	Side view showing Karman vortex street.....	54
Figure 1.6	Development of a closed vortex loop.....	54
Figure 2	Theoretical plots of ethanol vapor pressure and ethanol saturation pressure for the present experiments	55
Figure 3.1	Schematic of the wind tunnel facility.....	56
Figure 3.2	The vacuum tank of the wind tunnel facility	56
Figure 3.3	Photograph of the wind tunnel test section with the side wall removed	57
Figure 3.4	Drawing of the tapered plate with coordinate directions shown....	58
Figure 3.5	Side wall window with ports used in side wall pressure measurements.....	58
Figure 3.6	Photograph of the side wall and pitot probe measurement system set-up	59
Figure 3.7	Ethanol injection system	59
Figure 3.8	PLMS imaging set-up (side view set-up shown).....	60
Figure 3.9	Photograph of the Nd:Yag laser that produced the 532 nm beam for PLMS	60

Figure 3.10	Fields of view for images acquired from the side.....	61
Figure 3.11	Schematic of the test section for acquisition of side view images..	62
Figure 3.12	Photograph of the Nd:Yag laser, optics, and camera shown for acquiring end view images.....	63
Figure 3.13	Photograph of camera placement for acquiring end views	63
Figure 3.14	Double exposure photograph of the laser sheet entering the test section for end views.....	64
Figure 4.1	Low Re side wall pressure measurements	65
Figure 4.2	High Re side wall pressure measurements	65
Figure 4.3	Low Re, laminar boundary layer pitot pressure measurements and corresponding velocity profile at $x = -0.94$	66
Figure 4.4	High Re, turbulent boundary layer pitot pressure measurements and corresponding velocity profile at $x = -0.94$	67
Figure 4.5	Low Re, Pitot pressure measurements and corresponding velocity profile of the wake at $x = 1.98$ cm	68
Figure 4.6	Low Re, Pitot pressure measurements and corresponding velocity profile of the wake at $x = 5.08$ cm	69
Figure 4.7	Low Re, Pitot pressure measurements and corresponding velocity profile of the wake at $x = 8.13$ cm	70
Figure 4.8	Low Re, high resolution Pitot pressure measurements and corresponding velocity profile of the wake at $x = 0.69$ cm.....	71
Figure 4.9	Low Re, high resolution Pitot pressure measurements and corresponding velocity profile of the wake at $x = 1.98$ cm.....	72

Figure 4.10	Low Re, high resolution Pitot pressure measurements and corresponding velocity profile of the wake at $x = 5.08$ cm.....	73
Figure 4.11	Low Re, high resolution Pitot pressure measurements and corresponding velocity profile of the wake at $x = 8.13$ cm.....	74
Figure 4.12	Plotted normalized scales show self-similarity of the low Re wake for $x > 5.08$ cm.....	75
Figure 4.13	High Re, Pitot pressure measurements and corresponding velocity profile of the wake at $x = 1.98$ cm	76
Figure 4.14	High Re, Pitot pressure measurements and corresponding velocity profile of the wake at $x = 5.08$ cm	77
Figure 4.15	High Re, Pitot pressure measurements and corresponding velocity profile of the wake at $x = 8.13$ cm	78
Figure 4.16	High Re, high resolution Pitot pressure measurements and corresponding velocity profile of the wake at $x = 0.69$ cm.....	79
Figure 4.17	High Re, high resolution Pitot pressure measurements and corresponding velocity profile of the wake at $x = 5.08$ cm.....	80
Figure 4.18	High Re, high resolution Pitot pressure measurements and corresponding velocity profile of the wake at $x = 8.13$ cm.....	81
Figure 4.19	Mrel vs x/θ and eddy shocklets existence in the wake.....	82
Figure 4.20	Plotted normalized scales show self-similarity of the high Re wake	82
Figure 4.21	Far view taken from the side.....	83
Figure 4.22	Low Re, close up view taken from the side showing $x = 0.13$ to 6.22 cm.....	84

Figure 4.23	Low Re time averaged far view taken from the side. X is from 0.58 to 4.45 cm.....	85
Figure 4.24	Low Re case, temperature profile across the wake at x = 0.69 cm.	85
Figure 4.25	Low Re close up image taken from the side.	86
Figure 4.26	Schematic of eddy shocklets seen in side view images.....	86
Figure 4.27	Low Re, plan view with laser sheet level cutting the wake centerline. X is from -0.25 to 5 cm.....	87
Figure 4.28	Low Re, far plan view for x = 4.8 to 10.1 cm.....	87
Figure 4.29	Low Re, close up plan view at the wake centerline.....	88
Figure 4.30	Low Re, close up plan view at the wake centerline.....	89
Figure 4.31	Low Re, far plan view with the inclined laser sheet.	89
Figure 4.32	Low Re, close up plan view for the inclined laser sheet.	90
Figure 4.33	Low Re, close up plan view for the inclined laser sheet.....	90
Figure 4.34	Low Re, far plan view average with the inclined laser sheet	91
Figure 4.35	Schematic of third large scale structure in Fig. 4.32.	91
Figure 4.36	Low Re, close up plan view with the inclined laser sheet.....	92
Figure 4.37	Low Re, close up plan view with the inclined laser sheet.....	92
Figure 4.38	Low Re, end view at x = 0.25 cm.	93
Figure 4.39	Low Re, end view at x = 2 cm	94
Figure 4.40	Low Re, end view at x = 2 cm	94
Figure 4.41	High Re, far side view	95
Figure 4.42	High Re, close up side view	95
Figure 4.43	High Re, time averaged far side view	96

Figure 4.44	High Re, far plan view.....	96
Figure 4.45	High Re, far plan view.....	97
Figure 4.46	High Re, end view at $x = 2$ cm.....	97
Figure 4.47	High Re, end view at $x = 4$ cm.....	98

LIST OF SYMBOLS

a	Radius of a particle
b	Half-width of the wake
C_{sca}	Cross-sectional scattering efficiency
c	Speed of light in a specific medium
c_o	Speed of light in a vacuum
E_i	Incident laser energy flux
I	Intensity of light
I_o	Intensity of the incident light
$I_{scat//}$	Intensity of scattered light polarized parallel to the scattering plane
$I_{scat\perp}$	Intensity of scattered light polarized perpendicular to the scattering plane
k	Wave number
M	Mach number
M_{rel}	Relative Mach number
N	Index of refraction of a medium
n	Number density
P_o	Plenum total pressure, freestream total pressure
P_∞	Freestream static pressure
Re	Reynolds number
r	Radial distance
U	Velocity in the x direction

U_c	Velocity at the wake centerline
U_{def}	Velocity deficit in the wake
V	Probe volume
δ	Wake thickness
λ	Wavelength
∞	Infinity, freestream condition
ρ	Mass density
ω	Frequency
χ	Non dimensional size parameter used in Mie theory
θ	Momentum thickness, directional angle in scattering
$\bar{\omega}$	Vorticity
Ω	Solid angle subtended by an individual pixel on a detector
μ_∞	freestream viscosity

LIST OF ABBREVIATIONS

abs	Absolute
atm	atmosphere
kPa	kilopascals
nm	Nanometer
PLMS	Planar laser Mie scattering
2D	Two dimensional
3D	Three dimensional

CHAPTER 1

INTRODUCTION

1.1 Background and Motivation

In the field of fluid mechanics a great deal remains to be learned about supersonic wakes. In particular, one area is the structure of transitional and turbulent supersonic flat plate wakes, and the instabilities suspected of driving the development of the structure. The most basic flow configuration is the wake of a flat plate. Recently much research has been compiled about flat plate wakes with bluff trailing edges but little has been done on flat plate wakes themselves. There has also been substantial research conducted on wakes of supersonic axisymmetric bodies and incompressible wakes of a flat plates. By comparison, there has been very little experimental work done on supersonic flat plate wakes.

As a result, little is known about the structure of flat plate wakes, the mechanisms controlling the development of the wake, or the character of the wake turbulence. This thesis involves experiments for both laminar and turbulent wakes in a supersonic flow. The goal of this thesis is to provide a qualitative basis for understanding the structure of a supersonic wake. Such information will hopefully provide insight on the physical processes in the flow field.

1.2 Literature Survey

1.2.1 Categories of Wakes

When considering wakes there are four different categories that the topic may be broken down into: laminar incompressible wakes, turbulent incompressible wakes, laminar compressible wakes, and turbulent compressible wakes. The term incompressible denotes that the density changes in the flow are negligible. Flows whose Mach number is less than 0.3 are generally considered incompressible and those greater than 0.3 are considered compressible. The compressibility of a wake is based on the relative Mach number, M_{rel} , defined as

$$M_{rel} = \frac{U_{\infty} - U_c}{a_{\infty}}$$

where

U_{∞} is the freestream velocity

U_c is the velocity at the wake centerline

a_{∞} is the freestream speed of sound

From this definition it is possible to have both incompressible and compressible subsonic wakes. Supersonic wakes may be effectively incompressible even though the flow is compressible.

Laminar and turbulent refer to the state of the wake. The initial state of the wake depends on the type of boundary layer at the plate's trailing edge regardless of whether the flow is incompressible or compressible. A plate with a laminar boundary layer will initially have a laminar wake and a plate with a turbulent

boundary layer will have a turbulent wake.

1.2.2 Transition

However, the initial state of the wake is not necessarily the final state. A laminar wake may transition and become turbulent. Transition is the state of the wake between the laminar and turbulent states. Transition may occur slowly over a particular distance or it may take place so rapidly that it seems instantaneous. In nature, most laminar wakes transition and become turbulent.

Transition of a laminar wake to a turbulent wake is still not completely understood. To date, most research on wake transition has dealt with incompressible flows. Transition is caused by flow instabilities. These instabilities are caused by perturbations that either grow or diminish temporally or spatially. The classical description of instability is that of a ball shown in Fig. 1.1 for four different situations. In Case 1 if the ball is perturbed it will return to its original position and therefore is considered stable. In Case 2 the ball is neutrally stable. In Case 3, the ball may or may not return to its original position depending on the size of the perturbation so it is conditionally stable. Lastly, in Case 4 the ball is definitely unstable because a perturbation of any size will cause it to move from its original position and never return, so it is unstable.

The perturbations have been analyzed as waves, since any function can be broken down into a series of sine and cosine components. The perturbation

can be modeled as a wave in the form

$$\hat{A} = Ae^{i(\alpha x + \beta z - \omega t)}$$

where

$A = A(y)$ is the complex amplitude of the wave

α and β are components of the wave vector \vec{k} for the streamwise and spanwise directions, respectively

$\omega = \alpha c$ is the frequency of the perturbation

$c = c_r + c_i$ is the wave speed and has real and imaginary components

α and β will be real or complex if the flow is developing temporally or spatially, respectively. The imaginary component determines the stability of the flow in response to the perturbation. If

$c_i < 0$ The flow is stable

$c_i = 0$ The flow is neutrally stable

$c_i > 0$ The flow is unstable

The effect of perturbations (disturbances) that exist in the flow are similar to the instability of the ball. Situations where the disturbances are amplified are unstable, while disturbances that are damped out are said to be stable. Transition occurs due to a cascade of instabilities. It must be noted that just because a wake is

unstable does not mean that it will transition (White 1991). Likewise, transition will not happen unless the wake is unstable. In general, the viscous effects in the flow cause the damping of the disturbances, thus low Reynolds number flows are usually more stable than high Reynolds number flows. Rayleigh proved that inviscid flows with inflections in their velocity profiles are inherently unstable.

The Kelvin-Helmholtz instability theory predicts if a sheet of vortices are all rotating in the same direction, as shown in Fig. 1.2, their cross flow velocities cancel. If one is slightly perturbed (by moving it upwards) it will move into a region of higher velocity. As the vortex is displaced further away from the wake centerline, it encounters the larger velocity which will carry it further away from the centerline. In addition the vortex would experience a deformation since the velocity on the upper side is larger than on the lower side. The combination of these creates a non uniform field of vorticity that affects the other vortices. This rearrangement of vorticity in the wake results in the development of vortices of alternating signs called a Karman vortex street.

In nature, or experiments, the flow is never completely uniform without any irregularities (perturbations). As a result, according to the Kelvin-Helmholtz instability theory any wake would transition and eventually become turbulent. For incompressible flows the research on instabilities has been significant but comparatively little has been done for the compressible case.

1.2.3 Regions of the Wake

When investigating wakes one must understand spatially where we are in the wake. The x, y, and z coordinate directions refer to the streamwise, transverse, and spanwise directions, respectively. In all cases the freestream flow moves from left to right. Depending on different authors' opinions the streamwise distance has been divided into two or three regions (Bonnet and Chaput 1986). The first is the near wake region which starts at the trailing edge of the object. The second is the intermediate wake region and this can only be classified as between the near and far wake region. There is no method of distinguishing where the near wake ends and the intermediate wake begins. The last region is called the far wake and is where profiles of the flow properties (velocity, Reynolds stress) become self-similar. Self-similar means the state of the wake is only dependent upon a local property of the wake. Profiles of self-similar wakes will collapse when plotted in appropriate non dimensional form. From Panton (1984), for a wake these are

$$\frac{U_{\infty} - U}{U_{\infty} - U_c} = f\left(\frac{y}{b}\right)$$

The half-width, b, of the wake is the transverse distance measured from the wake centerline to the y location where the velocity is one-half the maximum velocity defect. The velocity defect, U_{def} , is equal to the local velocity subtracted from the freestream velocity. It is a maximum at the wake centerline.

1.2.4 Incompressible Wakes

This area of research has yielded significant results in the understanding of wakes. Due to the ease of building flow facilities, these were the first flows studied. The velocity profile for a laminar incompressible 2D wake is shown in Fig. 1.3. The velocity deficit is largest at the wake centerline. This is a result of the boundary layer fluid, which is at a lower velocity than the freestream being convected downstream. As the fluid progresses downstream more and more diffusion takes place between what was the boundary layer fluid and the freestream. As a result the velocity defect across the wake diminishes further and further downstream and gradually becomes Gaussian in shape. The velocity defect at the centerline for a flat plate can be measured according to

$$\frac{u(x,0)}{U_\infty} = \frac{0.664}{\sqrt{\pi}} \left(\frac{L}{x}\right)^{1/2} \quad (\text{White p. 260})$$

It should be noted that this is for a laminar wake that does not transition and applies to the far wake only (defined to be $x > 3L$ for a flat plate of length L).

Vorticity plays a key role in the development of the structure in of free shear layers. A mixing layer has vortices rotating in one direction (referred to as vortices having one sign) while a wake has vortices that rotate in two directions (vortices having two signs). Referring back to the velocity profile shown in Fig. 1.3 the vorticity is

$$\bar{\omega} = \nabla \times \bar{V} = \omega_x \hat{i} + \omega_y \hat{j} + \omega_z \hat{k}$$

where

$$\omega_x = \frac{\partial w}{\partial y} - \frac{\partial v}{\partial z}$$

$$\omega_y = \frac{\partial u}{\partial z} - \frac{\partial w}{\partial x}$$

$$\omega_z = \frac{\partial v}{\partial x} - \frac{\partial u}{\partial y}$$

The direction of vorticity is found from the right hand rule and is perpendicular to the plane of the rotating flow. For this case $u = u(y)$ only and the vorticity is

$$\bar{\omega} = \omega_z \hat{k} = -\frac{\partial u}{\partial y} \hat{k}$$

which is simply the negative slope of the velocity profile. By plotting the vorticity, shown in Fig. 1.4, we see the vorticity changes sign at the wake centerline thus a wake is said to possess double signed vorticity.

For 2D flows the laminar wakes stay 2D if they remain laminar. Rayleigh proved that inviscid flows that had inflection points in their velocity profile were unstable. Since the laminar wake has inflection points in both the lower and upper portions of its velocity profile it is inherently unstable. The laminar wake that transitions and becomes turbulent will not remain 2D. Breidenthal (1980) conducted

flow visualization experiments in a water tunnel for $Re = 300, 400, 2000, \text{ and } 3000$ to examine the dimensionality of wakes. He did not specify what scale he used for calculating Re . He used 3D 1.6 mm thick tapered wedges that were extended from a bluff edge plate. For low Re the boundary layers were laminar and the wake was initially laminar. The wake quickly transitioned. From the start the flow was 3D. Large scale structures were present for the low Re case but only small scale structures were present for the high Re case.

For $Re = 300$ the wake was initially laminar and then rolled up into a Karman vortex street of spanwise vortices of alternating signs. Figure 1.5 shows a Karman vortex street. The plan views of the wake centerline showed 3D horseshoe shaped structures that exhibited no growth in the spanwise direction as they convected downstream. Breidenthal called these vortex loops. After transition began the structure became blurred. There was an apparent growth during this stage more likely due to the structure starting to break apart rather than the structure increasing in size. As the Re was increased, the transition location moved upstream and at $Re = 3000$ the wake was completely turbulent with the Karman vortex street no longer present. The horseshoe shaped vortex structures in the plan view were also no longer present.

Meiburg and Lasheras (1988) also found the existence of vortex loops through both numerical simulations and flow visualization experiments. Their experiments were conducted using a 2D flat plate with laminar boundary layers for a $Re_\theta = 74$ (based on the momentum thickness). Their experiments involved

horizontal and vertical perturbations along the span with both cases showing the Karman vortex street present in the side view of the wake. Horizontal perturbations showed closed vortex loops of alternating sign aligned in the x direction similar to Breidenthal's (1980) results, while vertical perturbations resulted in the vortex loops being staggered in the x direction.

Meiburg and Lasheras (1988) proposed that the development of the vortex loops takes place as follows. First, the Karman vortex street develops and the perturbations in the flow cause the vortex line of spanwise vorticity to bow in the vertical direction. Since the velocity deficit of the wake is less further from the centerline, the bowed portion of the vortex line is carried further downstream and experiences shear. The bowing and shearing result in a reorientation of the vorticity producing a streamwise component of vorticity. The interaction with the alternating Karman vortices results in the stretching of the streamwise vorticity thereby increasing its strength. Eventually, closed vortex loops form. This is shown in Fig. 1.6. The name vortex loop is a misnomer since the loop is actually the directional vorticity result of four different components of vorticity from three vortex lines: the two Karman vortices and the bowed vortex line. There is not any rotation of the flow itself within the vortex loop. In fact, the loop creates a pocket of either upward or downward flowing fluid depending on the orientation of the loop. This pocket is evident in their flow visualization images.

Meiburg and Lasheras also concluded that the alternating Karman vortices have different strengths depending upon the spanwise location being examined.

Vortices of the same sign would have the same strength but would be either weaker or stronger than the vortices of the opposite sign. This trend continues all the way downstream. There is also a stagnation point between the Karman vortices of like sign but it is not directly in the middle. Rather, it is displaced in the streamwise direction closer to the downstream vortex.

Meiburg and Lasheras' experiments revealed that the topology of the wake can be likened to the bottom half of a corrugated egg carton. The Karman vortex street extends in the x direction with a perpendicular wave-like motion in the y direction. The closed vortex loops cause pockets that give the wake a mountain to valley structure.

For the turbulent wake the velocity deficit follows the same rule as the laminar case ($Uc \propto x^{1/2}$) in the far wake. The half-width, b , is proportional to $x^{1/2}$. The far wake here has been taken to be where $U_c \rightarrow U_\infty$. As stated, Breidenthal (1980) only observed small scale structures in the visualizations he conducted for the turbulent wake.

In the turbulent wake there is assumed a mean and a fluctuating component of the velocity. Using this assumption in the Navier Stokes equations, an additional term called the Reynolds stress is generated. The term is not actually a stress although it acts like one. The coherent structures are thought to play a crucial role because they are linked to the Reynolds stress. In boundary layers, where most of the research has been conducted for turbulence, the coherent structures are present

during periods where there are large peaks in the Reynolds stress.

1.2.2 Compressible Wakes

Although different, the compressible wake of a flat plate is similar to the incompressible wake in many ways. Chen et al (1989) used direct numerical simulations to study a time developing 2D wake and its transition for $M = 1$ and $M = 3$ with $Re = 300$ (using the half width of the wake for the length scale) in both cases. Their simulations reproduced the Karman vortex street. The amplification rates of the perturbations were varied. The most amplified rate was an antisymmetric perturbation in the streamwise direction. They concluded that the wake was initially 2D with secondary instabilities causing the wake to become 3D. It was also found that wake growth rates were suppressed at high Mach numbers due to baroclinic torque and dilatation effects. The results were quite similar to those of Mieburg and Lasheras. The development of the wake was attributed to the same physical processes proposed by Mieburg and Lasheras. The compressible simulations also found saddle points which were stagnation regions between the Karman vortices, a strain field generated by spanwise vortices, the stretching of the streamwise vorticity, and the formation of closed vortex loops similar to Mieburg and Lasheras' results.

In the side views Chen et al predicted that pressure maximum locations coincided with the saddle point regions while pressure and density minima coincided with the spanwise vortex center locations. Contour plots of streamwise vorticity for

the side view showed the vorticity initially concentrated at the wake centerline. As time progressed the vorticity took on a curvature evolving into a highly cambered airfoil with the largest gradients of vorticity being displaced from the centerline.

Plan views also showed low pressure regions aligned with the vortex cores. Chen et al found that the velocity fluctuations in the streamwise and spanwise directions were of the same order of magnitude. The plan views contained horseshoe shaped spanwise vorticity structures that developed when an oblique harmonic was included in the perturbations.

Gasperas (1989) used linear stability theory to study transition of a flat plate wake by examining the amplification rates of the disturbances by varying Mach number and Re_L . At $M = 3$ transition occurred 37% earlier for $Re_L = 20,000$ than $Re_L = 9,484$. The amplification rates of the disturbances in flows at $M=6$ were less than those at $M=3$ with transition delayed by 44% at the higher M . Using an e^N method, which is simply finding an N that fits the ratio

$$e^N = \frac{\text{final amplitude of the disturbance}}{\text{initial amplitude of the disturbance}}$$

Gasperas found that for the $M = 3$, $6.6 \leq N \leq 7.9$ but for $M = 6$ N could also be 7.8. This indicates that the e^N method for predicting transition must be investigated more thoroughly. The drawback to Gasperas's work is that in modeling the wake he used the same equations developed by Mack for a boundary layer. Since a boundary layer's velocity profile is different than a wake and the plane of a wake has a lower

layer below the centerline that interacts with the flow above the centerline, his results must be treated with some skepticism.

Breindenthal (1992) theorized the concept of a sonic eddy and the possible effects on growth rates for turbulent wakes. Noting that changes in a vortex line are only felt locally because information can only travel at the speed of sound, he defined the sonic eddy size and proposed that only sonic eddies with a rotational $M=1$ would entrain fluid. Larger eddies cannot make a complete revolution to entrain any fluid. From these assumptions he predicted the wake would stop growing at a specified distance and thereafter grow at an incompressible rate.

Bonnet and Chaput (1986) have looked at the structure of a turbulent wake using flow visualization at $M=1.975$ and $Re_L = 8 \times 10^7$. Bonnet et al (1991) conducted experiments using hot-wire anemometry for $M=0.1, 2, 4.2$ on the same plate. The supersonic flows had a $Re_L = 6 \times 10^7$. The Reynolds numbers in both experiments were based on the length of the plate in supersonic flow. The flow visualization showed only small scale structures present in the near wake and large scale structures in the far wake. The large quasi-elliptical structures were inclined at angles of up to 60 degrees from the wake centerline. Unfortunately, the region of transition from small scale to large scale structures could not be seen due to their wind tunnel design. The hot-wire anemometry confirmed the inclination of the large structures at supersonic speeds but indicated there was no inclination at subsonic speeds.

Dutton et. al (1995) proved the existence of eddy shocklets using PLMS in a turbulent mixing layer ($M_1=2.5$, $M_2=2.0$). Although the flat plate used had a bluff trailing edge, and there were other parameters affecting the flow such as the upstream recompression shock, this was still significant and was the first experimental confirmation of the shocklets. Emanating from the large structures in the flow, the shocklets were curved and seemed to coalesce into the recompression shock. The images also showed the recompression shock is not straight but bowed and was influenced by the eddy shocklets.

CHAPTER 2

PLANAR LASER MIE SCATTERING

2.1 Mie Scattering Theory

Planar laser Mie scattering (PLMS) is a laser diagnostic technique involving the scattering of laser light from small particles. Since Bohren and Huffman (1983) provide an excellent discussion in detail for those unfamiliar with PLMS, only a working theoretical description is presented to permit the reader to understand the images.

Light is an electromagnetic field and can be thought of as either a particle or a wave propagating in a particular direction. When light passes through a medium that has a different index of refraction, N , the light will be refracted (bent) changing its direction of propagation and will change its speed. The index of refraction is defined as

$$N = \frac{c_o}{c} = \frac{3 \times 10^8 \text{ m/s}}{\text{speed of light in the medium}}$$

and

$$N - 1 \propto \rho$$

where ρ is the density of the medium.

Mie theory is concerned with the scattering of light from a spherical dielectric particles of known refractive index. A dielectric material is one that is non conducting. When light in the form of an incident field encounters the particle, it induces charges (dipoles) within the material into oscillation. These dipoles then generate their own electromagnetic field which is reradiated (scattered) at the same frequency as the incident light (a particle may also absorb the light if the light is at the resonant frequency of the material). The direction of this scattered light is dependent upon the polarization of the incident field and the particle's size. Although light can be circularly polarized, the simplest case is when the light is linearly polarized, as is a laser beam.

The size of the particle relative to the wavelength of the light is an important issue. Since each particle reradiates an electromagnetic field, if there were 100 particles impacted by the laser beam, there would be 100 electromagnetic fields being reradiated. If the particle is much smaller than the wavelength of the light the scattered light from all the different particles will be in phase. This type of scattering is known as Rayleigh scattering. Since the ethanol particles in PLMS are at most $0.2 \mu\text{m}$ (discussed later) and $\lambda=0.532 \mu\text{m}$ PLMS for these experiments is close to the Rayleigh scattering regime.

There is a difference in the scattering depending on whether the polarization is parallel or perpendicular to the scattering plane. The scattering plane is defined as the plane containing the incident ray and the scattered ray. The directional

dependence of Rayleigh scattering for incident light polarized parallel to the scattering plane is,

$$I_{scat||} = \frac{9|a_1|^2}{4k^2 r^2} \cos^2 \theta$$

$$a_1 = \frac{i2x^3}{3} \frac{N^2 - 1}{N^2 + 2}, \quad x = \frac{2\pi a}{\lambda}$$

if air is assumed to have an index of refraction of 1, where

θ is measured clockwise from the direction of propagation.

a is the particle's radius

$k = \frac{2\pi}{\lambda}$ and is the wave number of the incident light

r is the radial coordinate of the scattered plane

N is the particle's index of refraction

Since the cosine function is zero at 90 degrees, there will be scattering at this angle.

For incident light that is perpendicularly polarized to the scattering plane we have,

$$I_{scat\perp} = \frac{9|a_1|^2}{4k^2 r^2}$$

and does not depend on the angle from which the scattering is being viewed. As a result it does not matter where the signal detector is placed because the light is uniformly scattered.

By assuming that the incident field is linearly polarized, that particles are

dielectric and spherical, and that we are in the Rayleigh scattering regime, the following formula for the scattering cross-section is obtained,

$$C_{sca} = \frac{8}{3} \pi a^6 \left| \frac{N^2 - 1}{N^2 + 2} \right|^2$$

where C_{sca} is how much energy is scattered per unit time per unit irradiance. Notice that C_{sca} is proportional to the particle's radius to the sixth power. As a result, a slight increase in the particle's size will result in a large increase in signal. The total scattered signal per pixel is,

$$S \equiv E_i C_{sca} n V \frac{\Omega}{4\pi}$$

where

E_i is the incident laser energy flux

n is the number density

V is the probe volume

Ω is the solid angle subtended by a pixel

The scattered signal is linearly proportional to the number density, n , of the particles, i.e. more particles per volume equals more scattered light. Also, the more irradiance (intensity I_o) the incident beam has, the stronger the scattered light will be.

2.2 Condensation and Evaporation

A vapor will tend to condense if its vapor pressure is greater than its saturation pressure at the local static temperature. The ratio of the vapor pressure to the saturation pressure is called the supersaturation ratio (SSR). In order for the molecules of the species to condense among themselves and not on dust or other foreign particles present in the flow, the SSR must be large (≥ 10). This occurs because with large SSRs there are many more particles of the liquid that have condensed compared to the number of foreign particles present. Flow traveling through an expanding supersonic nozzle has a rapid decrease in temperature as it expands. Due to the rapid cooling, the SSR can attain values significantly larger than unity. Wegener et al (1972) have shown that for $SSR > 10$ rapid condensation will take place.

Wegener et al also measured the time for the condensation process in a supersonic nozzle and is estimated to be 50 μ sec. Assuming, for the present experiments, the flow travel at Mach 1 through the entire nozzle (being conservative) the ethanol would have condensed 1.6 cm after the throat. Since the length from the throat to the nozzle exit was 11 cm, there would be sufficient time for condensation to occur even at $M = 1$.

If the condensed particles encounter a warm region they will evaporate due to the rise in the saturation pressure. The SSR accordingly decreases, and at $SSR=1$, the liquid particles will have completely evaporated.

2.3 Particle Size: An Issue

A note of caution must be taken when using seeded flows. If the seeded particles are too large, or more accurately if their response time is too slow, they will not be able to track the air molecules in the flow, thus giving a misrepresentation of the flow field structure. Clemens and Mungal (1991) used a two-color transmissometer to determine particle size mean diameter. They found that the largest size the particles could be, in an ethanol fog generated in a Mach 2 supersonic nozzle, was $0.2 \mu\text{m}$ in diameter. They also used a polarization ratio technique which measures the intensity for incident light that is polarized parallel and then perpendicular to the scattering plane. The ratio of these two measurements is a function of the particle diameter d . From this ratio it was determined that the ethanol droplets were no larger than $0.25 \mu\text{m}$ in diameter. Their studies showed that the time response for particles of this size would be much greater than large scale structures seen in a turbulent flow and can therefore track the flow.

Since Clemens and Mungal were running at approximate $P = 1 \text{ atm}$ in their test section, the number density of the ethanol was much higher compared to running at 0.027 atm for the present experiments. For the present case, therefore, the particles would be expected to be smaller than those for Clemens and Mungal because the lower mass density (hence number density) results in lower coagulation rates.

Clumpner (1971) measured the particles in a supersonic nozzle and found them to be approximately $0.01\text{-}0.02 \mu\text{m}$ in diameter. This again suggests the

particles are small enough to track the flow and that PLMS is very close to the Rayleigh scattering regime.

CHAPTER 3

EXPERIMENTAL FACILITY AND PROCEDURE

3.1 Wind Tunnel

3.1.1 Overall Design

The experiments were conducted at the J.J. Pickle Research Center at the University of Texas in Austin. The tunnel was a 5.08 x 5.08 cm Mach 3 blowdown type wind tunnel which was supplied by high pressure air and exhausted into a large vacuum tank. A schematic of the tunnel is shown in Fig. 3.1 and a photograph of the vacuum tank is shown in Fig. 3.2. To attain supersonic laminar flow, the test section was operated at low pressure ($\cong 2.7$ kPa abs) by exhausting into a vacuum. Due to the accompanying reduced density, Re_L was low enough to obtain laminar compressible boundary layers at the plate's trailing edge and a laminar compressible wake.

3.1.2 Test Section

The test section's top and bottom walls could be converged and/or diverged to compensate for the variation of the streamwise pressure gradient. For these experiments the walls were kept parallel to produce an approximately zero pressure gradient flow. The test section was square (5.08 cm x 5.08 cm) and was 31 cm long. Refer to Lachney (1995) for extensive details on the test section. A photograph of the test section with the sidewall removed and without the plate is

shown in Fig. 3.3. Note the holes which support the plate are seen midway up the side.

The plate used, shown in Fig. 3.4, was a 0.635 cm thick stainless steel tapered flat plate 27 cm in length that had a 3 degree full angle taper. The thickness of the trailing edge was 0.0762 cm. A thinner tip was not used because of possible warping in the machining process. The plate's leading edge was also tapered and began upstream of the sonic throat to prevent the generation of shocks. The length of the plate in the supersonic part of the flow, i.e. the length of the plate measured from the nozzle's throat, was 23.65 cm. The plate was attached to the sidewall of the tunnel by screws. This eliminated the need for any supports which could have generated disturbances in the flow.

Optical access to the test section was provided by six acrylic windows: two side windows, and inner and outer top and bottom windows. Originally, there was not a bottom outer window, but preliminary side view PLMS tests showed there was less background interference (fewer reflections) if the laser beam was permitted to pass through the bottom of the test section. Also, preliminary tests showed that there was significantly less background interference for sideviews if the far side window was clear rather than painted flat black. All parts of the test section except the plate and windows were painted flat black to absorb reflections.

The tunnel had two pressure transducers installed, one in the plenum and one in the test section. One measured the total pressure in the plenum and the other

measured the static pressure in the test section. An Omega PX 243 pressure transducer with a range of +103 kPa (gauge) to -103 kPa (gauge) was used in the plenum. An Omega PX241 pressure transducer with a range of -103 kPa to 0 psig was used in the test section. This latter transducer was located 3.56 cm into the test section. For reference the plate extended 13 cm into the test section.

Since this was an entirely new flow facility, it was unknown how far the plenum pressure could be reduced and still obtain Mach 3 flow. To test this, various runs were made. The tunnel was checked to see if it started, i.e. the normal shock has passed through the test section and the flow is shock free, to determine what Mach number had been attained in the test section, and to see how long the tunnel would run before unstating. It was found that the plenum pressure could be no lower than 121kPa absolute and obtain a Mach 3 flow in the test section. Maximum run times were approximately one minute for the low Re_L case. Runs up to a minute and a half in length were possible for the high Re_L case.

Sidewall pressure measurements were conducted to establish the streamwise pressure gradient and the presence of any unwanted shocks or expansions. An asymmetry in previous measurements in the test section had shown that the support screw holes in the side walls were sufficiently larger than the screws allowing the plate to shift and become misaligned. To correct this, aluminum blocks were machined and used to properly align the plate during installation. An expansion wave coming off the top inner window of the tunnel also contributed to the asymmetry of the pressure readings. This was corrected by tightening the window

so that it was flush with the test section ceiling.

3.2 Pressure Measurements

3.2.1 Side Wall Pressure Measurement Set-up and Procedure

Side wall pressure measurements were obtained by attaching a window, shown in Fig. 3.5, with 47 static pressure ports to the side of the test section. Each port was 0.83 mm in diameter and were arranged in three horizontal rows spaced 1.71 cm apart vertically. The center row was aligned with the trailing edge of the plate. The ports in each row were spaced 1.27 cm apart horizontally. Stainless steel tubes 1.6 cm in diameter and 3.8 cm long were inserted into the outer side of the ports and sealed with epoxy. Since the window was originally designed for a different length plate, measurements were made and then the window was rotated and measurements taken again to cover the entire wake region. The actual setup is shown in a photograph in Fig. 3.6.

The stainless steel tubes were connected by tygon tubing to a model 48J4 Scanivalve. The Scanivalve, which is a pressure multiplexer, could measure up to 48 ports. The stepping of the Scanivalve was controlled by a model CTLR10P/S2-26 solenoid controller. The Scanivalve was operated at a rate of 4 ports per second. The output voltage of the Scanivalve was digitized by a DT2831-G Data Acquisition board installed in a Dell 433s/M computer. This output was passed through a 10 Hz low-pass RC filter to remove noise generated by the Scanivalve. A program called PULSE7.C was used to control the stepping rate of the Scanivalve. The resulting

pressure measurement at each port was an average of 50 samples that were taken by the Scanivalve. The program also acquired and averaged 10 samples from the plenum transducer and 10 samples from the test section transducer to obtain the pressure at those locations. For additional details see Sanders (1994).

3.2.2 Pitot Probe Pressure Measurement Set-up and Procedure

Pitot pressures were measured by inserting a Pitot probe through the top inner window and into the test section. The probe is shown in the tunnel between the plate and the top of the test section in Fig. 3.6. The probe was connected to the Scanivalve similar to the side wall set-up. The Scanivalve did not switch ports because there was only one port being used (the one connected to the probe). The probe opening was 0.48 square millimeters. Its outer width and height were 1.5 mm and 0.6 mm, respectively. The inner width and height were 1.2 mm and 0.3 mm, respectively. The probe was connected to a Velmex A1506B screw motion Unislide assembly whose screw was threaded for 20 turns per inch and that had a turn knob at the top. The probe traversed vertically through the wake by manually turning the turn knob on the Unislide. One turn equaled a vertical distance of 0.05 inches. The streamwise location of the probe was changed by extracting the probe and reinserting it through another hole in the inner window. By doing this, the pressure at several locations was measured including the pressure through the flat plate's upper boundary layer. At each vertical location 50 measurements were taken and averaged. Ten pressure measurements from each transducer were also averaged and recorded with the side wall pressure measurements. This information was then

sent to the data acquisition board.

3.3 PLMS Set-up and Procedure

The PLMS injection and imaging setups are shown in Figs. 3.7 and 3.8, respectively. A 5.5 liter cylinder was filled with 95% grade ethanol. A bottle of nitrogen with a high pressure regulator was connected to the top of the cylinder with 6.35 mm copper tubing. The bottom of the cylinder had 6.35 mm tubing that passed through a control valve and connected to a Spraying Systems 1/4 LN .60 atomizing spray nozzle. The spray nozzle sprayed particles having a 35 μm mean volume diameter at a volumetric flow rate (\dot{Q}) of approximately 9 l/hr at 2.7 MPa abs. It should be noted that the flow rate specifications were incorrect from the factory (they show $\dot{Q} = 7.2$ l/hr). When the control valve was opened the ethanol (at ≈ 3.8 MPa abs) was injected into the main air supply which was at approximately 1.1 MPa abs, thus $\Delta P = 2.7$ MPa. The injection location was 3.4 m upstream of the plenum.

Initially, an injection location closer (1.65 m prior) to the plenum was tried however, the ethanol did not have enough time to evaporate before reaching the plenum. Large liquid droplets rather than a fine fog resulted. To correct this problem, the injection location was moved further upstream and two mixing enhancement devices were installed 1.77 and 1.44 m prior to the plenum. This created more turbulence resulting in enhanced mixing of the ethanol in the air. The devices consisted of a 2 cm diameter metal plate bolted to the center of a piece of perforated plate. This insured that most of the ethanol liquid droplets had

evaporated before reaching the plenum.

The laser used was a Nd:Yag laser, shown in Fig. 3.9, generating a 532 nm laser beam having approximately 60 mJ of energy. The beam was turned and focused through a spherical lens and then through a cylindrical lens which expanded the beam in one dimension only, thus turning the beam into a planar sheet. The sheet was approximately 250 μm thick at the waist (at the focus).

A Cohu 4990 series CCD monochrome video camera was used and connected to the frame grabber (Data Translation DT2851-G card) in a Dell 433s/M computer. The camera gain was turned down as low as possible and the shutter speed was set at 10 microseconds. An image acquisition/processing software package called VDO was installed in the computer. Images were acquired at 3 Hz with a maximum acquisition of 90 images (limited by the 12 megabytes of extended memory in the computer). The images were digitized to 512 x 240 pixels. During each run typically 60 images were acquired, each of which required 123 kbytes of storage memory. A total of 80 runs were made including testing the different injection locations. The far and closeup views had fields of view of 5.34 cm and 2 cm, respectively for the side and plan views unless stated otherwise. Fig. 3.10 shows a schematic of the different fields of view taken from the side. The far views were taken using a 50 mm Cannon lens with an f-number of 1.4. Close up views were taken with the same lens with a 15 mm lens extension.

A schematic of the side view imaging set-up is shown in Fig. 3.11. For the

side views the beam entered the test section from the top passing through two acrylic windows and then exiting through two acrylic windows (recall the test section had inner movable walls that had windows). The beam then passed into a cardboard box with a slit for an entrance to prevent light from reflecting back into the test section. This greatly reduced the background noise as previously discussed.

The camera was placed above the test section for the plan views and the laser sheet was brought in from the side with the sheet parallel to the wake centerline or inclined at approximately a three degree angle.

Figure 3.12 shows the laser, optics, and camera in position for the end view. Because the camera could not be placed directly at the end of the test section, it was placed as close to this location as possible as shown in Fig. 3.13. A double exposed photograph of the laser beam illuminated by cigarette smoke is shown entering the test section in Fig. 3.14. Although the photograph shows the film has slightly moved it still is a good depiction of the beam entering the test section.

After the laser was aligned and the image acquisition system was put in place, the laser was turned on and the tunnel was started. After the normal shock had passed through the test section and the flow was shock free, the ethanol was injected into the main stream.

Since the laser was on during the entire run, as soon as the fog entered the test section an image was seen on the computer monitor. The camera lens was then

adjusted to obtain a good focus. If the signal was low, the ethanol injection pressure was increased until the signal was satisfactory. Lastly, if the signal was still weak the laser energy was increased to increase the scattering, but sometimes the acrylic-glass windows could not handle the intensity and burned. If the laser sheet was passing through a burn spot on the window the refraction would create a bright spot on the image and the laser sheet would need to be slightly shifted to avoid the burn.

Typically 60 averages were acquired. After the tunnel was turned off but the laser was still on, 10 images were taken of test section and averaged, becoming the background image that was later subtracted from the 60 images. After a run was made the vacuum pump required 40 minutes to pull an adequate vacuum in the test section for another run to be made. A total of 80 runs were made using PLMS including testing injection locations and optimizing the technique.

3.4 Image Processing

Image processing was done using a public domain software package called Khoros from the Univ. of New Mexico. Khoros offers a graphic/icon user friendly interface called Cantata.

In Cantata, the user creates a flow sheet of the commands to be executed in processing the images. Since signal intensities varied from run to run each image needed to be processed individually. The processing involved subtracting the background image from the flow image. The background was the signal that was

present without the tunnel running but the laser on. Since all surfaces reflect some percentage of the incident light there will always be some background interference present.

The image was then "clipped," that is, any bright spots which were due to unevaporated ethanol droplets were reduced to allow amplifying the rest of the image. Since it was necessary to distinguish between unevaporated droplets and lesser bright regions due to flow structure, the droplets, though clipped, were left much brighter compared to any other bright regions. The unevaporated droplets appear in the images as circular bright spots. The images were next passed through a 3 x 3 pixel median low pass filter. By filtering the image the freestream was more uniform. This was not done to all images since this resulted in less sharper images, and the ability to distinguish detailed shape was sometimes more important than smoothing the images.

Since the laser beam did not have a uniform intensity distribution, but a Gaussian distribution, a laser sheet correction was made. The laser sheet correction was performed by averaging a line consisting of several rows in the freestream region across the entire image. The values at each column in this line were then divided into the rest of the image. This sheet correction would also divide out the effects of coagulation. Since the plan and some end views did not have a continuous freestream region they were not corrected for the laser sheet.

The images were then rescaled by multiplying all pixels by a constant to a

maximum of 255. In Khoros the square shape of the pixels required that to obtain the proper aspect ratio of 4:3 (horizontal:vertical dimensions) the images must be converted from 512 x 240 to 512 x 384 pixels.

CHAPTER 4

EXPERIMENTAL RESULTS AND DISCUSSION

4.1 Pressure Measurements

The two cases examined involve laminar and turbulent boundary layers at the plate's trailing edge. The plenum pressure, P_o , was 79 kPa absolute for the laminar case and 184 kPa absolute for the turbulent case. The corresponding Reynolds numbers were $Re_L = 2.4 \times 10^6$, $Re_\theta = 1800$ and $Re_L = 3.3 \times 10^6$, $Re_\theta = 3700$ for the laminar and turbulent case, respectively. The Reynolds numbers were defined as

$$Re_L = \frac{\rho_\infty U_\infty L}{\mu_\infty}, \quad Re_\theta = \frac{\rho_\infty U_\infty \theta}{\mu_\infty}$$

where

ρ_∞ is the freestream density

U_∞ is the freestream velocity

L is the plate's length

μ_∞ is the viscosity of the freestream, assumed to vary as $T^{0.7}$

θ is the momentum thickness of the wake near the plate's trailing edge

The low Re flow had $M = 2.85$ upon entering the test section while the higher Re flow was $M = 3.0$. Side wall and Pitot probe measurements were taken of the wake. Pitot probe measurements were also taken on the plate's upper surface to determine

the state of the boundary layers.

4.1.1 Side Wall Pressure Measurements

The side wall pressure measurement results are shown for both the low and high Re cases in Figs. 4.1 and 4.2, respectively. Note that the pressure is a mean static pressure and not an instantaneous static pressure. The pressure has been normalized by the plenum pressure for each port sampled. In both cases, the top row of ports is nearly symmetric with the bottom row of ports. This indicates the wake is symmetric. The middle row is aligned with the wake centerline ($y = 0$).

The plenum/test section pressure ratio indicates that the flow is at $M = 2.85$ upon entering the test section. The slight decrease in the pressure prior to the beginning of the wake confirms the flow is accelerating due to the area increase from the tapering of the plate. This is a 13% increase in area resulting in a Mach number change of 0.1 to $M = 2.95$ at the plate's edge. Since the plate's edge does have a finite thickness, there is also a slight expansion around the edge. Due to these circumstances it is difficult to determine the exact Mach number. The most accurate Mach number is found by applying the isentropic relations to the side wall pressure ratio, giving $M = 3.1$ at the plate's edge. For the high Re case the pressure ratio in Fig 4.2 gives $M = 3.2$ at the plate's trailing edge.

At any given streamwise location, the static pressure in both cases varies little in the y direction. This agrees with Lachney (1995) who found, using planar

laser induced fluorescence, that the static pressure was constant across the wake of a bluff edge plate. In both cases, there is an increase in the pressure due to the presence of a shock at about $x = 7.2$ cm. This pressure rise of 7% corresponds to a normal shock with $M_1 = 1.03$ for the laminar case. In the high Re case the pressure rise is 17% corresponding to a normal shock with $M_1 = 1.07$. These are thus weak shocks that have little effect on the flow.

Near the end of the streamwise location, there is an overall gradual rise in the pressure that is larger for the low Re case than the high Re case. This is the result of the area decreasing from the boundary layer growth on the walls.

4.1.2 Pitot Pressure Measurements

By assuming the static pressure in the y direction was constant and the boundary layer and wake were adiabatic, the Pitot pressure measurements were converted to velocity. Although Demetriades (1969) found that the local total temperature does vary across an adiabatic turbulent wake, the maximum variation of 4% is considered negligible. The Rayleigh Pitot probe formula was used to convert pressure to a Mach number which was then converted to velocity.

4.1.2.1 Pitot Probe Boundary Layer Pressure Measurements

Boundary layer pressure measurements were made with the Pitot probe system previously described. The laminar boundary layer profiles are shown in

Fig. 4.3 . These were taken at $x = -0.94$ cm. Due to system constraints, measurements could not be made exactly at the plate's tip . Since the height of the probe was 0.07 cm, only a few data points could be obtained in the boundary layer itself. The velocity boundary layer thickness, δ , defined as the distance from $y = 0$ to y where $U = 0.99U_{\infty}$, is 0.19 cm.

The turbulent boundary layer profiles are shown in Fig. 4.4. For the turbulent boundary layer case, $\delta = 0.381$ cm.

4.1.2.2 Pitot Probe Wake Pressure Measurements

Due to the limited run times of the tunnel, fine resolution probe measurements of the entire test section were not possible. Probe measurements with higher resolution of the transverse scale were made near the wake centerline. The wake grows very little. As a result, there is a region between the wake and the shock where the pressure is similar to the freestream pressure.

Low Re Case

Pitot pressure measurements of the entire transverse direction are shown in Figs. 4.5 through 4.7. We can see the edge of the boundary layer on the tunnel floor and ceilings. Accounting for the normal shock in front of the Pitot probe, the decrease in the pressure at $y = 1$ cm in Fig. 4.5 corresponds to the expansion fan which is present just before the shock. The increase in pressure in the same figure at

$y = 0.75$ cm is from the shock. The expansion fan and shock are symmetrical about the wake centerline. The shock location from the side wall pressure and probe measurements coincide.

The higher resolution probe measurements across the wake centerline are shown in Figs. 4.8 through 4.11. The half-width, b , grows from 0.158 to 0.255 cm over the region $0.69 < x < 8.13$ cm. The momentum thickness, θ , was numerically evaluated at each location using Simpson's area rule. The thickness was $\theta = 0.2$ mm and remained constant downstream.

As the probe location is moved further downstream the pressure in the wake decreases and the pressure profile starts to take on a Gaussian shape. Table 1 shows U_c , and M_{rel} for various x and x/θ locations. The largest deficit gave $U_c = 266$ m/s at $x = 0.69$ cm with $M_{rel} = 1.7$, hence the wake is very compressible at this location. The velocity deficit rapidly decreases. Just over 1 cm further downstream ($x = 1.98$ cm) the velocity deficit is small enough that U throughout the entire wake is supersonic and M_{rel} is still supersonic. M_{rel} becomes subsonic shortly thereafter. By $x = 5.08$ cm, $M_{rel} = 0.42$ and the wake is nearly incompressible and for $x > 8.13$ cm the wake is incompressible.

To determine the degree of self-similarity of the wake, velocity profiles of different streamwise locations were normalized by y/b and plotted in Fig. 4.12. The profiles collapse further downstream in the wake. For $x > 5.08$ cm the velocity profiles collapse very well.

High Re Case

The high Re case, shown in Figs. 4.13 through 4.18, exhibits the same trend as the low Re case. The shock angle, β , has expectedly decreased for the higher M flow. However, M_{rel} is always subsonic even though U is always supersonic through the wake with a minimum $U_c = 455$ m/s. The data is shown in Table 2. At $x = 0.69$ cm, $M_{rel} = 0.93$. Although becoming subsonic quicker, the velocity deficit does not continue to diminish rapidly. By $x = 5.08$ cm, M_{rel} is larger than the low Re case. A comparison of x/θ vs M_{rel} for both cases shows

$$M_{rel} = f\left(\frac{1}{x/\theta}\right)$$

and is plotted in Fig. 4.19. Normalized velocity profiles are shown in Fig. 4.20. The momentum thickness is equal to 0.3 mm

4.2 PLMS Results

All images are instantaneous unless stated otherwise. Dark sections in the images are regions of higher temperature where the ethanol has evaporated. As a result, no light is scattered and therefore no signal detected. The brighter the region, the higher the intensity of the scattered light. Regions of increased density will appear brighter than neighboring regions.

Due to the small size of the test section, the transition point on the plate moves further inward towards $z = 0$. This is a result of the junction between the corner vortices where the plate and side wall meet. At the centerline this transition region protrudes approximately 30% (1.5 cm) into the test section on each side. Away from the centerline the protrusion diminishes rapidly. As a result, the uncontaminated region at the centerline is the center 40% of the wake. Similar structure at the centerline also appears away from the centerline where the transition region protrudes less. The conclusion is that the uncontaminated region is not influenced by the transition region and therefore the data obtained from the uncontaminated region is valid.

4.2.1 Low Re Case

Side View

Instantaneous images with far and close up views were acquired. The instantaneous views were averaged to obtain a time average image of the flow. An instantaneous far view is shown in Fig. 4.21. Three close up views of the same region are shown as a composite in Fig. 4.22. The bright circular spots, seen in the freestream, are caused by large droplets of unevaporated ethanol. These droplets could not be avoided without suffering an unacceptable decrease in the scattering signal.

The dark region at the left in the far view results from the two detached laminar boundary layers which have come together at the trailing edge of the plate.

This dark region is 0.2 cm in height with each boundary layer contributing 0.1 cm. A time average of 60 images is shown in Fig. 4.23. The dark region at the beginning of the wake is the same thickness as in the instantaneous images, suggesting the laminar region is stationary. However, the thickness does not match δ from the probe measurements. The reason for this is that the upper portion of the boundary layer is not warm enough to evaporate the ethanol, thus cannot be seen. Figure 2 shows the ethanol will evaporate at $T = 231$ K. Assuming an adiabatic flow the Pitot pressure profiles can be converted to temperature profiles. A temperature plot in Fig. 4.24 at $x = 0.69$ cm shows the droplets will evaporate at $y = 0.08$ cm, which is in good agreement with the 0.1 cm indicated from the images. The growth of the wake, as one moves further downstream, can be seen in both the instantaneous and time averaged views.

Just above the evaporated region, a bright thin film can be seen and is labeled in Fig. 4.25. The film's location is still within δ . The intensity is brighter than the freestream indicating a region of compression. The film continues beyond the shock and into the wake. It weakens and then eventually diminishes around $x = 2$ cm. At this time we do not have an explanation for this effect.

Since the probe measurements provide mean values, the average of the far views would be the most accurate image to view for a corresponding shock location. The shock location shown in the Pitot pressure measurements corresponds with the shock location shown in Fig. 4.23. For example, at $x = 1.98$ cm the shock is at $y = \pm 0.635$ cm in the probe measurements and is the same for the average image.

The shock angle, β , is equal to 17 degrees. With the 1.5 degree taper, β increases to 18.5 degrees and if $\beta \cong \mu$, $M = 3.1$. This is the same result found from the side wall pressure measurements.

Eddy shocklets, indicated on Fig. 4.21, are also present. Similar shocklets were found in bluff trailing edge wakes by Dutton et al (1995). The shocklets seem to coalesce into the shock. In fact, in the close up views in Fig. 4.22 the shock is not straight but curved. A schematic of the flow is shown in Fig. 4.26. The shocklets seem to be emanating not from the top of the individual structures but from near their bow. The eddy shocklets are stronger than the shock. The density change, which is proportional to the signal increase or decrease, was 10% for the shock corresponding to a normal shock with strength $M = 1.06$. The shocklets' density increase was 30% corresponding to a normal shock with strength $M = 1.18$. This can be attributed to both the high M_{rel} near the centerline and to the expansion the flow experiences as it rounds the peak of the structure just prior to shocking. Due to the higher M_{rel} the eddy shocklets are strongest at the beginning of the wake. The eddy shocklets disappeared at $x > 3.1$ cm. This is in the vicinity of M_{rel} becoming subsonic, shown in Fig. 4.19.

The vortices on the upper section of the wake seem to be more dominant than on the lower section. This could be an asymmetry due to the 3D nature of the wake structure. The question to ask is if this applies to all images or is the wake fluctuating. Note that this is similar to Mieburg and Lasheras's (1988) findings. Correspondingly, the shocklets on the upper part of the core are stronger than on the

lower part. However, in the close up view there is no difference. This is probably due to the laser sheet passing through the wake at a slightly different z location.

Figure 4.22 shows the development and the formation of the typical Karman vortex street with the upper and lower vortices having negative and positive spanwise vorticity, respectively. The detached boundary layer fluid undergoes a deformation with the structures taking on a cambered airfoil appearance. As the wake progresses downstream, the airfoil structures continue to deform and expand transversely. The growth of the wake occurs at 5.4 degrees in Fig. 4.22 and similarly in the far view of Fig. 4.21 at 4.2 degrees.

The streamwise distance, λ_{sv} , between the centers of two consecutive vortices of like sign was measured. Since the precise location of the centers is somewhat arbitrary, λ_{sv} is an approximation. In Fig. 4.21, the far view, $\lambda_{sv} = 5.8$ mm and remains constant downstream. In Fig. 4.22, the close up view, $\lambda_{sv} = 8$ mm and remained constant. Since Fig.4.22 is a composite of three different images and λ_{sv} is the same in each image, it is unlikely that the 30% difference in λ_{sv} between the two views is a measurement error. The difference in λ_{sv} could be related to the asymmetry of the strength of the vortices in Fig. 4.21.

Returning to the close up views of Fig. 4.22, the consecutive vortices of alternating sign seem to be connected by a braid region of fluid, as found by Mieburo and Lasheras. There are also bright regions (not the circular spots) on these braids that are suspected of being regions of compression. Initially thin and well defined,

the braids become thicker and less defined as they start to break down.

Plan View with Laser Sheet Cutting the Wake Centerline

Far views cutting the wake centerline are shown in Figs. 4.27 and Fig. 4.28. In Fig. 4.27 the dark region at the left edge is the laminar boundary layer. Immediately following is the laminar wake. The light region is the freestream fluid that has been entrained into the wake. Near the trailing edge of the plate, spanwise structures at the center become convoluted and form cusps. The laminar wake starts to go unstable 5.5 mm after leaving the plate. In the close up of this region, Fig. 4.29, the wake takes on a structure where the large scale structures are separated, from center to center, by a streamwise distance of 3.5 mm. Since this view is cutting both the lower and upper vortices of the Karman vortex street the value 3.5 mm is actually the distance between consecutive vortices. This value must be doubled to obtain λ_{pv} , the distance between consecutive vortices of like sign in the plan view. Doubling gives $\lambda_{pv} = 7$ mm, in good agreement with $\lambda_{sv} = 8$ mm found in the close up side views.

Smaller circular dark structures are seen attached on the upstream side of the large scale spanwise structures by small braids of fluid similar to the side view case. These circular structures, a result of secondary instabilities in the flow, first appear in the center. By the time the wake is about 5 cm downstream, the wake has broken down and is nearly turbulent. In Fig. 4.30 regions of compression are present around most of the individual structures. These regions are similar to the

compression region seen on the braid in the side views and are possibly related.

Plan View Using An Inclined Laser Sheet

A plan view cut was also taken with the laser sheet passing through the test section at an angle of about 3 degrees measured counter-clockwise from the x-axis. As a result, the transition region extends less into the test section. A far view is shown in Fig. 4.31. The close ups are shown in Figs. 4.32 and 4.33. The images suggest the wake is a spanwise segment of the wake investigated by Mieburg and Lasheras, i.e. we only see one period of the corrugated wake structure. A 60 shot average of the far view, shown in Fig. 4.34 reveals that over time these structures are not randomly distributed but are concentrated near $z = 0$.

A dark circular region is the first appearance of any individual structures in Fig. 4.31. The next structure to appear is in the shape of a horseshoe. The horseshoe has a cavity, a concave region on its upstream side. The horseshoe structure appear very similar to those simulated by Chen et al (1989). At about $x = 2.5$ cm small-scale vortices appear on the upstream side of the horseshoe structures. These vortices are likely due to a secondary instability caused by the high strain present in the braid region. In fact, these small-scale structures appear inside the cavity of the horseshoe. In many cases the structures appear to have tails. The simulations of Chen et al (1989) did not predict the development of the small-scale structures.

The large-scale structures do not grow in spanwise length, similar to the

results of Breidenthal (1980). However, the structures do grow in streamwise length further downstream. This occurs because the laser sheet is at a 3 degree inclination but the wake grows faster at about 4.5 degrees. Therefore, the laser sheet is cutting a larger streamwise cross-section of the structures further downstream. The large structures breakdown on their upstream side while the downstream side maintains its shape longer.

The close up views, in Figs. 4.32 and 4.33, also reveal that the upstream side of the structure breaks down while the downstream side maintains its shape. Since the laser sheet enters the test section at an angle, the large-scale structures in the images are the vortices of like sign in the upper half of the wake that are cut by the laser sheet. Structure in the lower half of the wake will not appear. The spacing between the center of the large-scale structures is $\lambda_{pv} = 8$ mm in agreement with $\lambda_{sv} = 8$ mm. As in the side view case, λ_{pv} remains fairly constant in the streamwise direction.

In Fig. 4.32, the third structure's cavity has a cusp extending in the upstream direction at its center. This cusp is created by two counter rotating vortices that are drawing fluid in between the vortices. See the schematic in Fig. 4.35. This peak turns into 4 peaks in the next structure indicating the presence of 4 pairs of alternating vortices. The cavity region has a thin membrane-like appearance. The small circular dark vortices seem to be spinning and many have bright regions of compression that are on the upstream and downstream sides of the vortices. The suspected regions of compression may actually be regions of high particle

concentration in a strain region. This is possible since high intensity regions are present regardless of the magnitude of M_{rel} . Figure 4.36 shows a compression region in the cavity, which is present over the entire visible portion of the cavity. Prior to the horseshoe structure there are streamwise striations in the wake. These cannot be explained presently.

At the beginning of the region, there are faint spanwise dark regions that span the entire z direction. This suggests the wake is briefly 2D. Not all the images have a single structure along the spanwise direction. In Fig. 4.37 two structures emerge side by side. Both possessing a cavity at the rear of their structure, they seem to merge further downstream.

End View

As stated previously, end views were taken by placing the camera at an oblique angle with respect to the flow direction, looking through the side window. The spanwise field of view was 5.8 cm. A smaller field of view could not be obtained because there was too much distortion through the acrylic window. The far views did reveal the side wall boundary layers and an overall view of the structure.

The transition region near the centerline can be seen in Fig. 4.36 at $x = 0.2$ cm. The side wall turbulent boundary layer is above and below the transition region. As previously mentioned, the transition region protrudes in furthest at the

wake centerline and then diminishes. This is expected since the corner vortices where the side wall and plate meet would amplify the turbulence. Images taken from the left and right sides of the test section showed no difference in the extent of the protrusion of the transition region on either side. The dark region in the center is the laminar wake which is about 0.22 cm thick, in good agreement with the side views. Individual structures are absent since the wake is laminar.

Further downstream, at $x = 2$ cm, the wake has changed. Figure 4.39 shows there is definitely structure present but little detail is discernible. Only the largest individual structures, such as the horseshoe shape in the center, are distinguishable. The shock, bowed at different spots, appears above and below the wake. The upper shock bends in the $+y$ direction at the presence of the horseshoe structure. Directly beneath this structure, the shock bends toward the centerline. In Fig. 4.40 the horseshoe shapes appears in the lower portion of the wake. The dark region on the outside of the shock is the expansion seen in the side views. The horizontal bright straight line between the wake and the edge of the shock is a reflection off the corner of the plate where its taper begins. The white cross-hairs represent the approximate location of the laser sheet in the side and plan views.

4.2.2 High Re Case

Side View Images

Side views are shown starting with Fig. 4.41. The turbulent boundary layer

detaches from the tip of the plate. The boundary layer fluid actually passes through the shock. The turbulence in the wake causes the shock to bulge as seen in the close up in Fig. 4.42. The shock angle is about the same as in the laminar case. The shock is slightly stronger with a larger density increase across the shock. Eddy shocklets are not distinguishable as in the low Re case. This correlates with the subsonic relative Mach number of the high Re wake. A 13 image average is shown in Fig. 4.43 (because the signal in many of the images was saturated only 13 images could be averaged). The wake grows at a much higher rate than in the low Re case.

Plan View Images

Far views are shown in Figs. 4.44 and 4.45. There is no evidence of large scale structure. The turbulence is dominated by small scale structure. Individual structures are able to be distinguished but it is not possible to determine their relationship with any neighboring structures. This is in agreement with Bonnet and Chaput (1986). Close ups did not reveal anything more nor did the inclined sheet

End View Images

End view images are shown in Figs. 4.46 and 4.47. Like the plan views there does not seem to be any coherent structure to the flow.

CHAPTER 5

CONCLUSION

Compressible wakes have a similar structure to that of incompressible wakes. In the low Re case, an initially laminar compressible wake becomes unstable, producing the usual Karman vortex street. The plan views revealed horseshoe shaped structures found in incompressible wakes and direct numerical simulations of compressible wakes. Full spanwise length structures indicate the wake is briefly 2D. Eddy shocklets, not present in incompressible wakes or in the direct numerical simulations, are present. A key parameter seems to be the relative Mach number and how quickly the compressibility decreases. Eddy shocklets disappeared when M_{rel} became subsonic. Suspected weak compression regions were seen that cannot be explained. Secondary instabilities appear as small counter rotating vortices only on the upstream sides of the horseshoe structures.

The high Re case shows the turbulent wake is dominated by small scale turbulence. There is very little evidence of large scale structure. There seems to be structure in the side views whereas in the plan and end views the structure is highly random. The wake is completely 3D and turbulent from the beginning. Eddy shocklets do not appear since the relative Mach number is subsonic throughout the wake. The high Re flow, though not initially as compressible as the low Re case, retains its compressibility longer.

Table 1 Low Re case with $U_\infty = 612$ m/s and $a_\infty = 203$ m/s.

x (cm)	x/θ	U_c (m/s)	b (cm)	M_{rel}
0.69	35	266	0.158	1.7
1.98	99	374	0.127	1.17
5.08	254	526	0.19	0.42
8.13	407	560	0.255	0.25

Table 2 High Re case with $U_\infty = 635$ m/s and $a_\infty = 190$ m/s.

x (cm)	x/θ	U_c (m/s)	b (cm)	M_{rel}
0.69	23	455	0.127	0.95
1.98	66	490	0.18	0.76
5.08	170	517	0.25	0.62
8.13	271	527	0.254	0.57

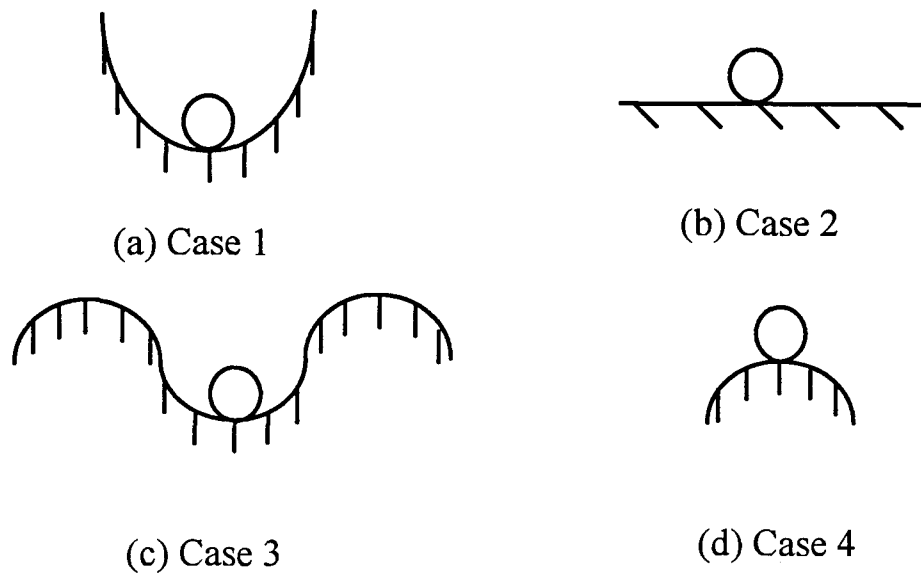


Figure 1.1 Stability of a ball.

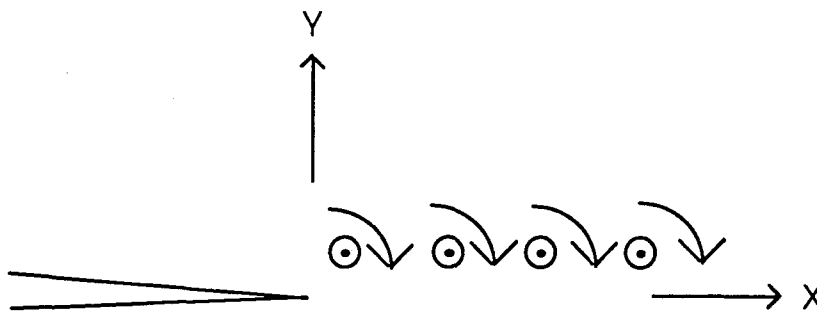


Figure 1.2 Illustration of vortices in the Kelvin-Helmholtz instability theory. Side view of the plate.

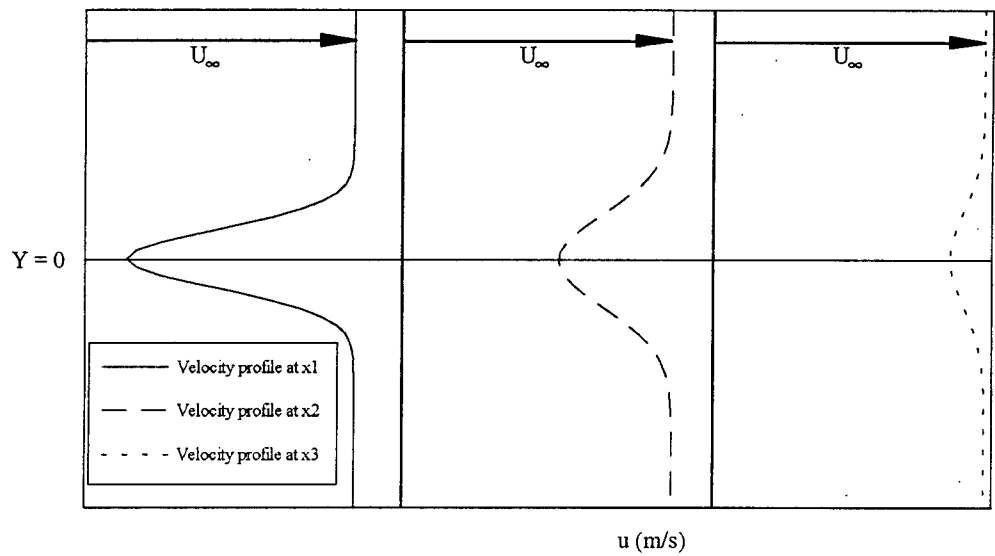


Figure 1.3 Mean velocity profiles of a laminar flat plate wake in the far wake region.

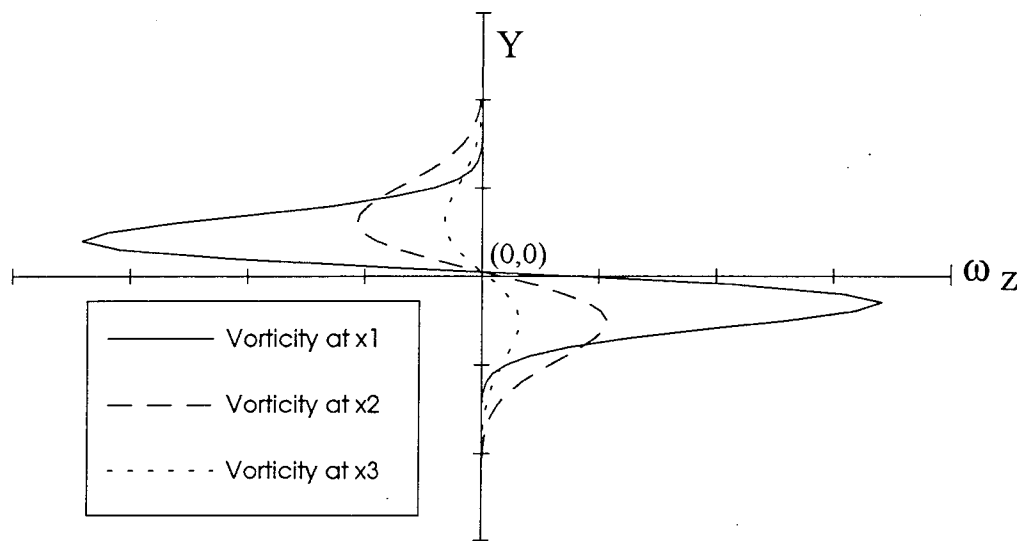


Figure 1.4 Vorticity of a laminar flat plate wake corresponding to the velocity profiles shown in Figure 1.3.

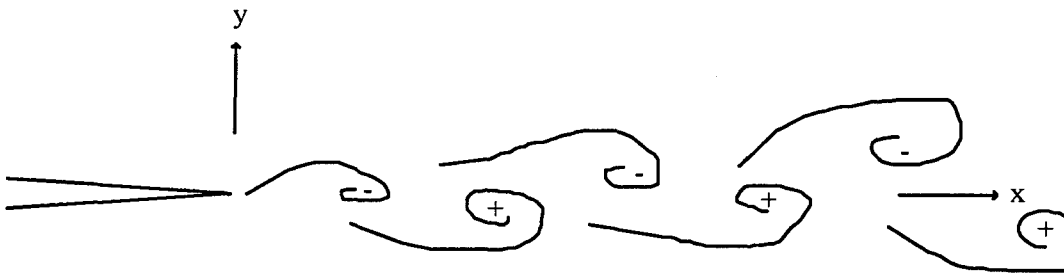


Figure 1.5 Side view showing Karman vortex street with signs of vorticity.

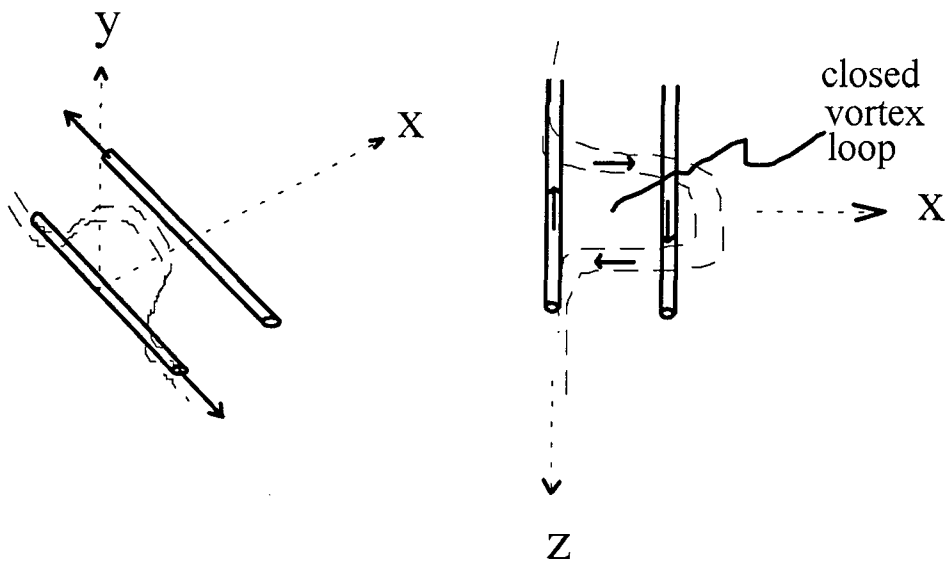


Figure 1.6 Development of a closed vortex loop. Arrows represent vorticity.

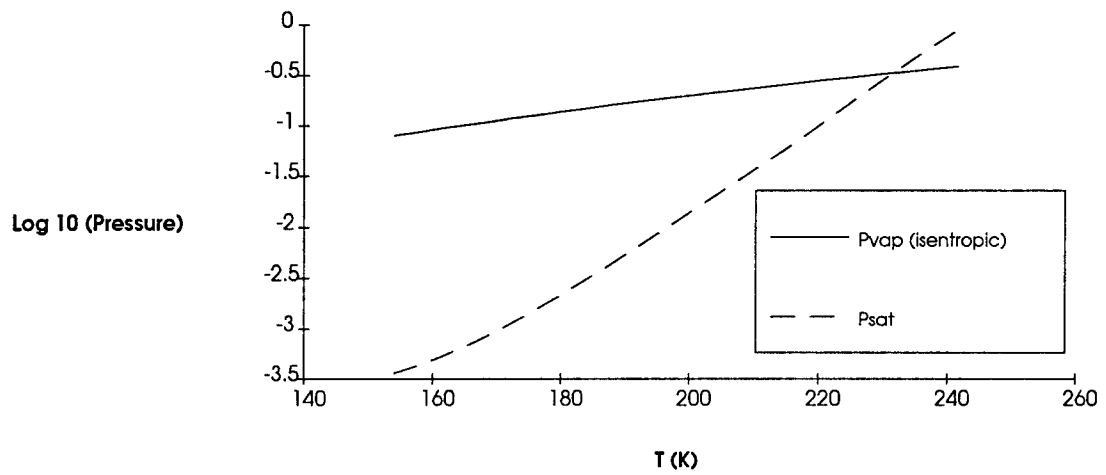


Figure 2 Theoretical plots of ethanol vapor pressure and ethanol saturation pressure for the present experiments.

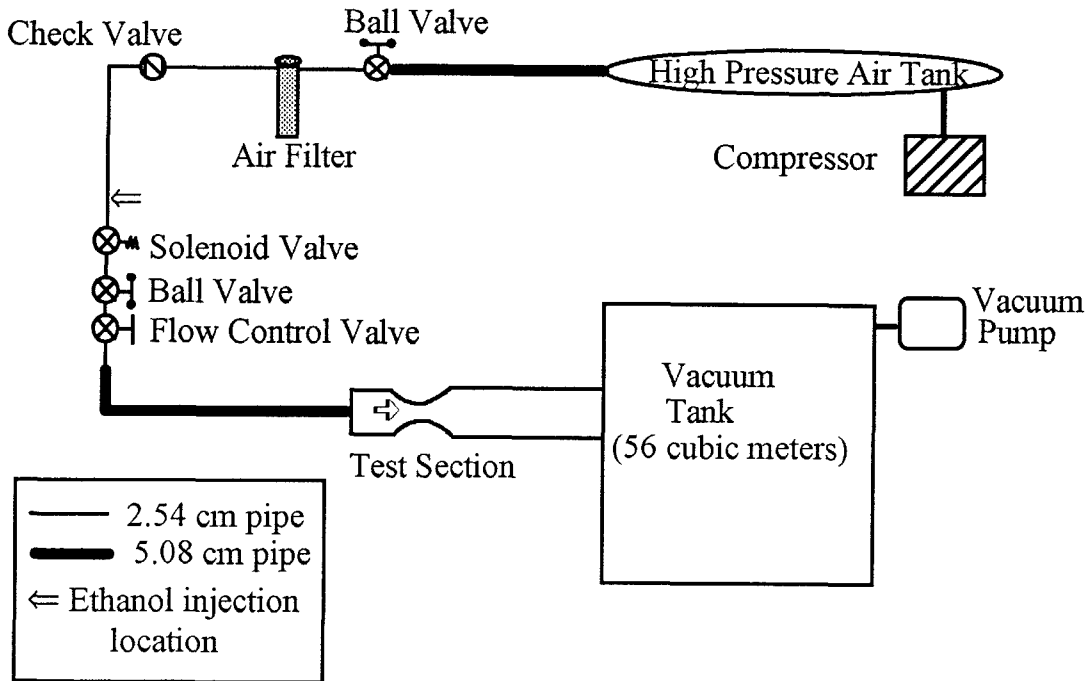


Figure 3.1 Schematic of the wind tunnel facility.

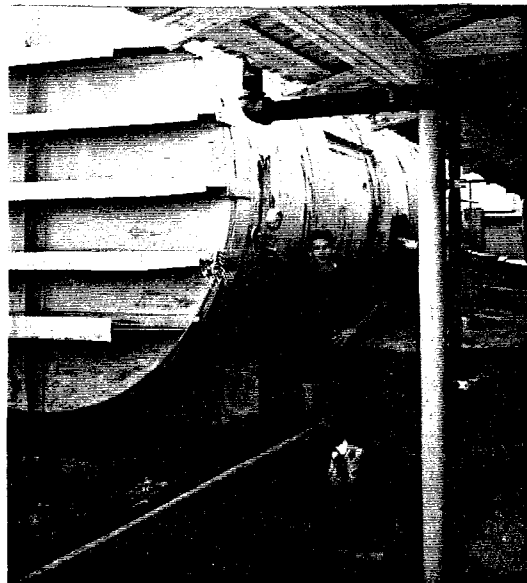


Figure 3.2 The vacuum tank of the wind tunnel facility.

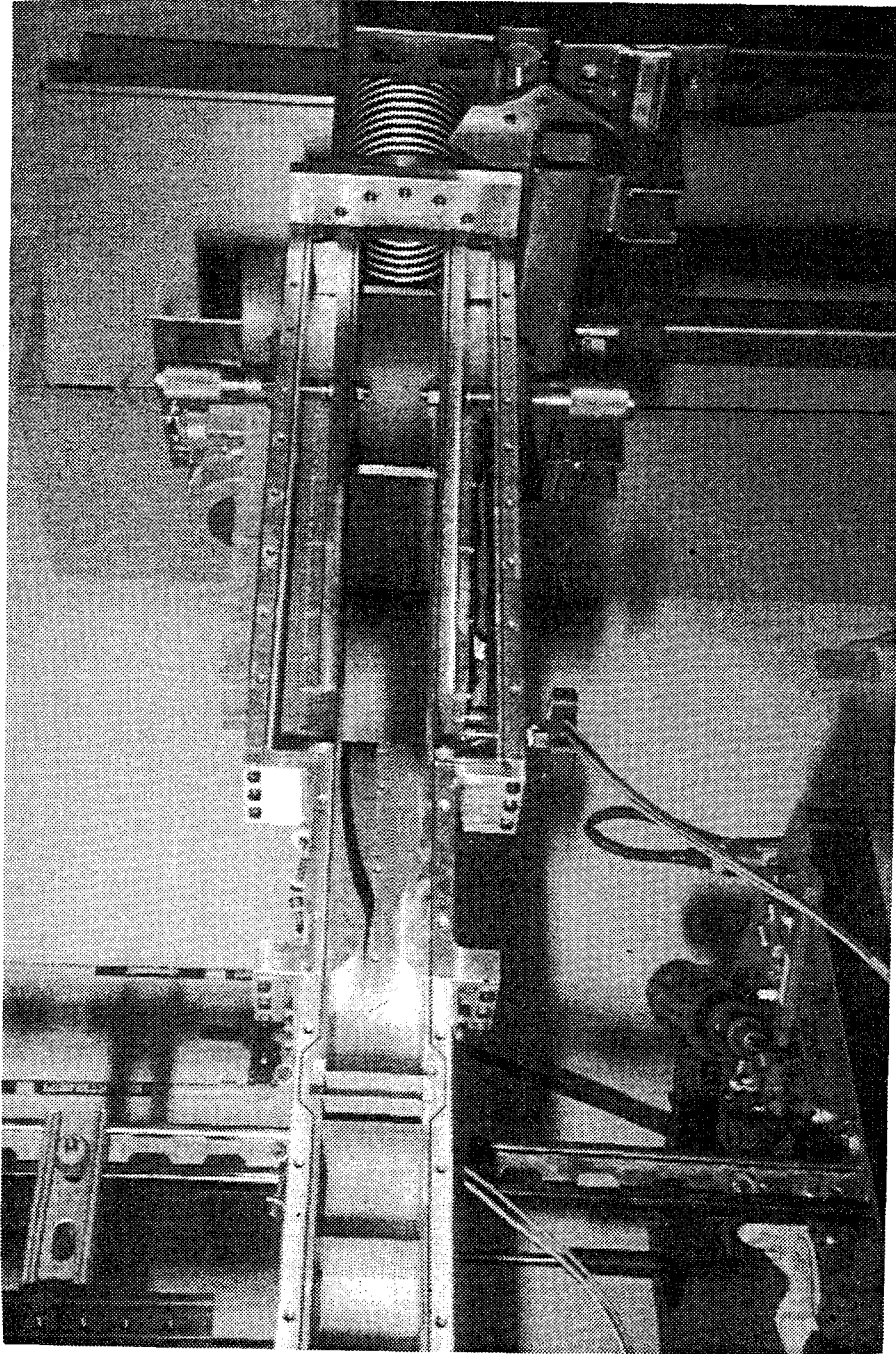


Figure 3.3 Photograph of the wind tunnel test section with side wall removed. Support holes for the tapered plate in the nozzle can be seen.

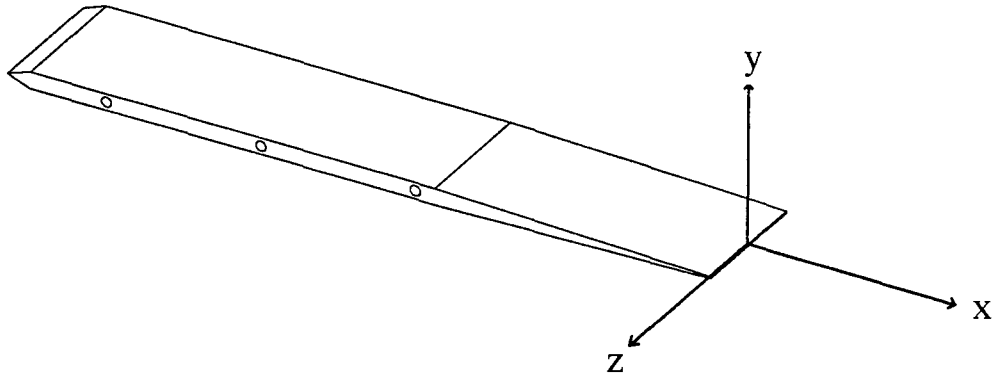


Figure 3.4 Drawing of the tapered plate with coordinate directions shown.

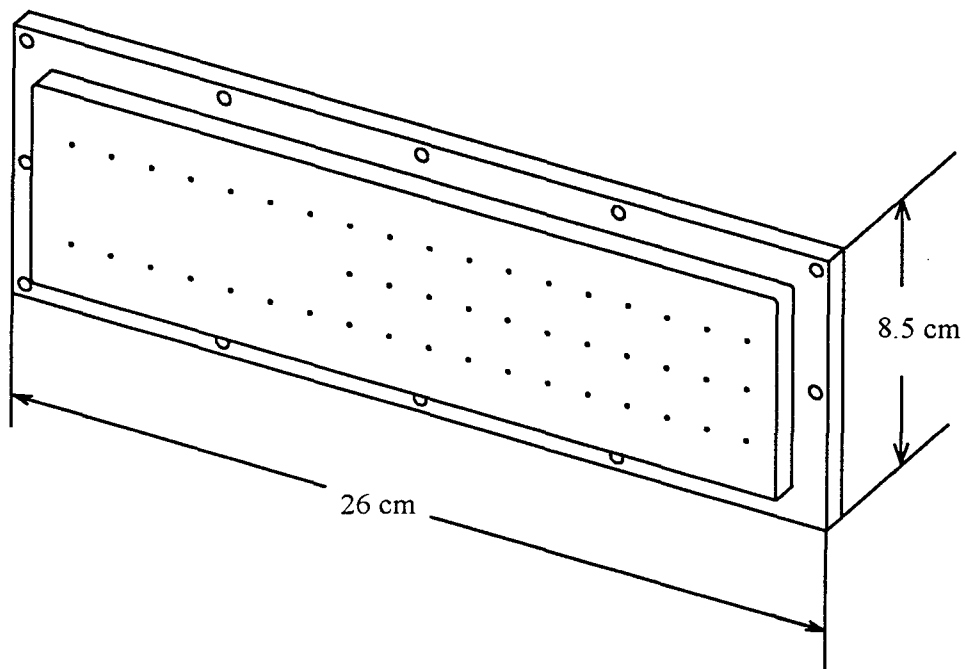


Figure 3.5 Side wall window with ports used in side wall pressure measurements.

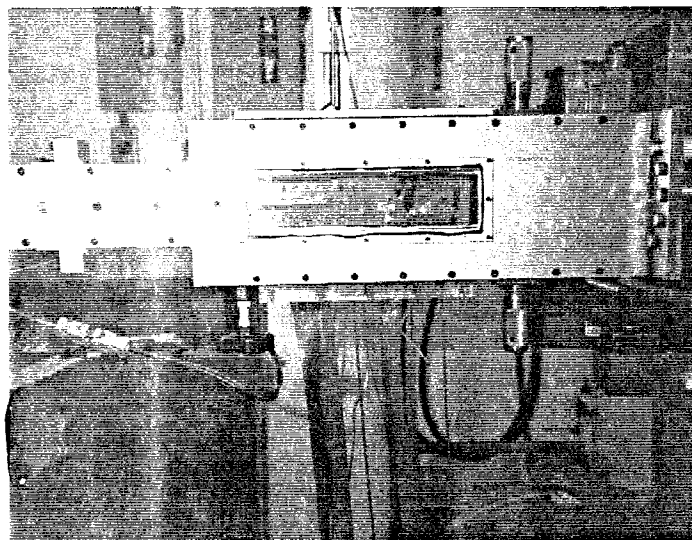


Figure 3.6 Photograph of the side wall and pitot probe pressure measurement system set-up.

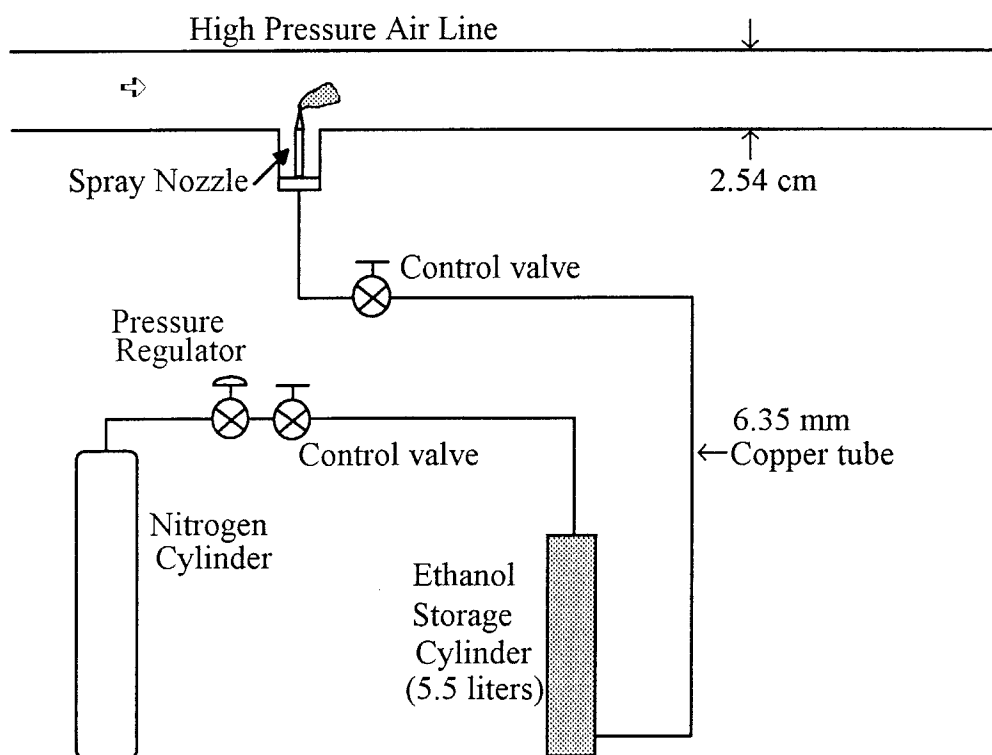


Figure 3.7 Ethanol injection system.

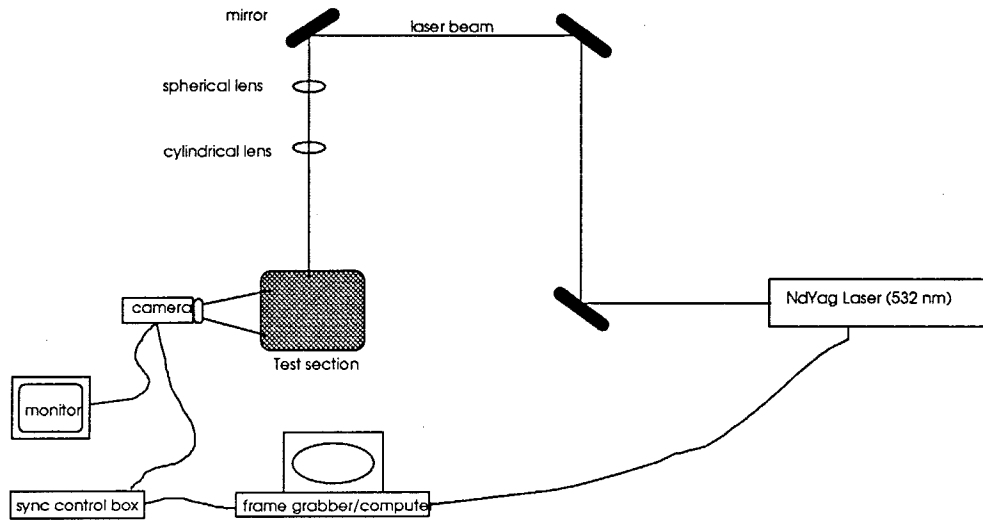


Figure 3.8 PLMS imaging set-up (side view set-up shown).

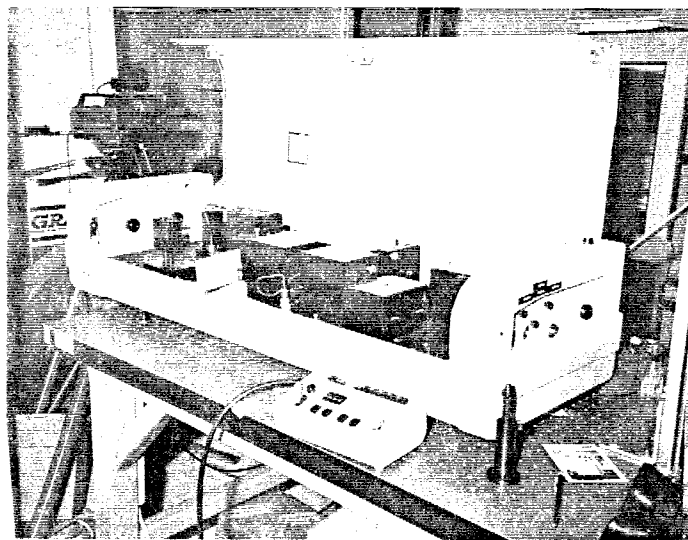


Figure 3.9 Photograph of the Nd:Yag laser that produced a 532 nm beam for PLMS.

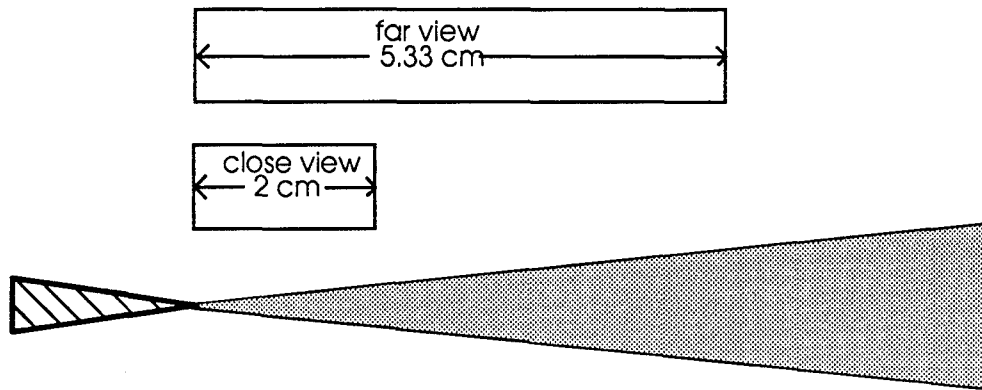


Figure 3.10 Fields of view for images acquired from the side.

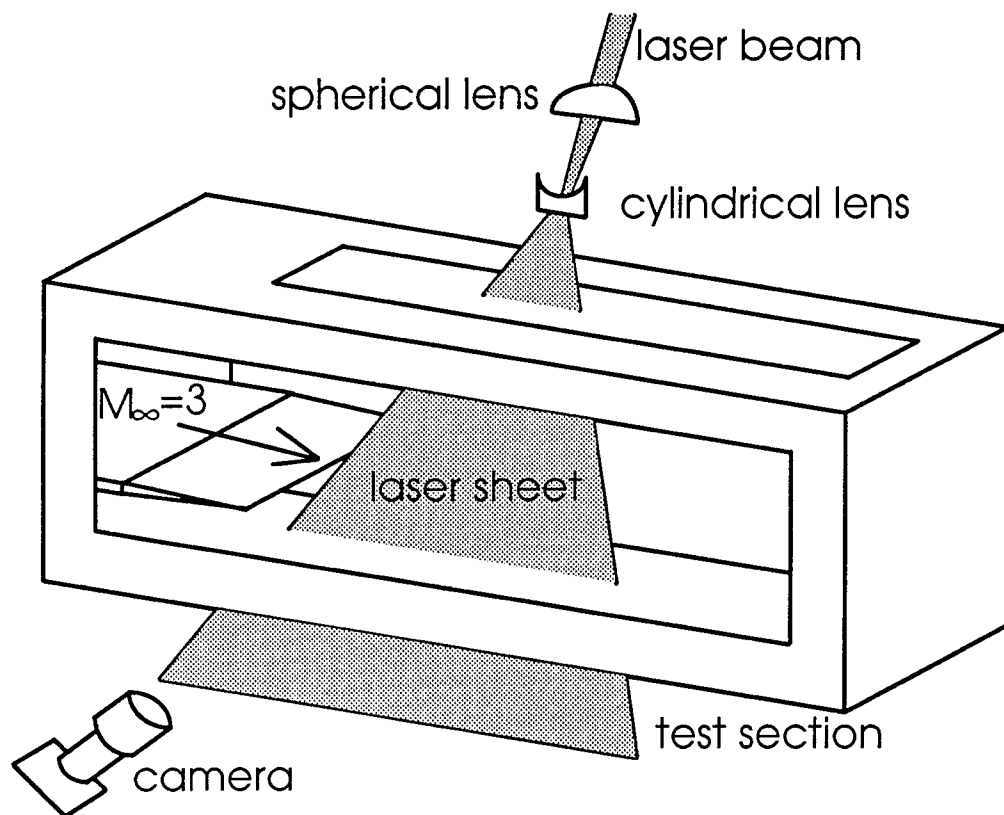


Figure 3.11 Schematic of test section for acquisition of side view images.

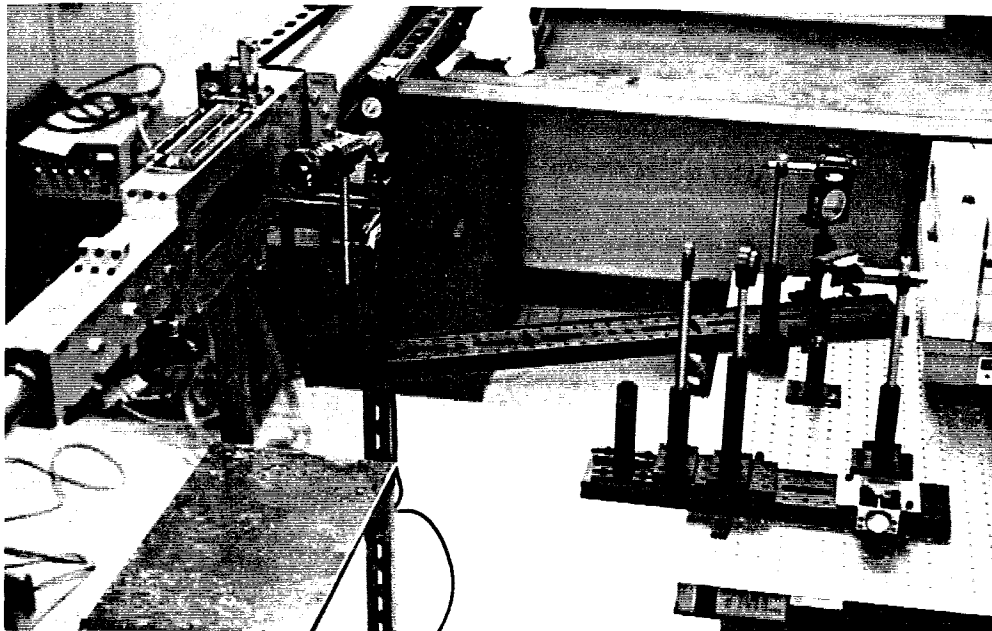


Figure 3.12 Photograph of the Nd:Yag laser, optics, and camera for acquiring end view images.

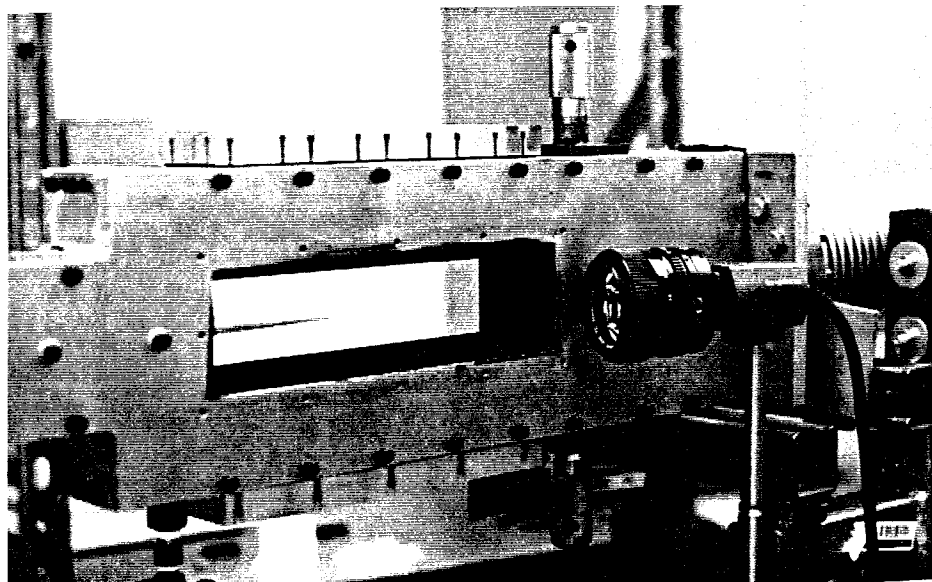


Figure 3.13 Photograph of camera placement for acquiring end view images. The side window has been removed.

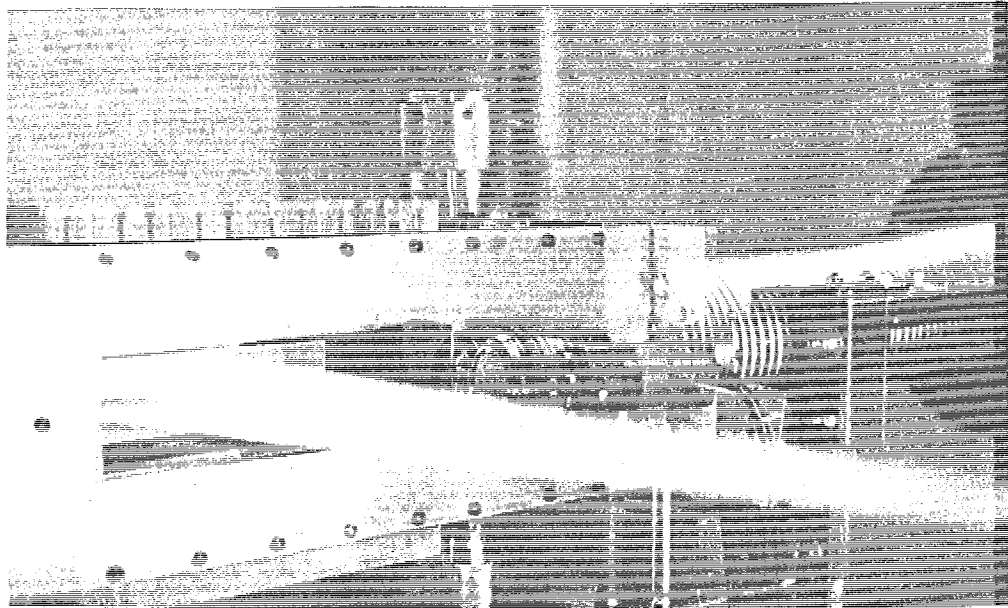


Figure 3.14 Double exposure photograph of the laser sheet entering the test section for end views.

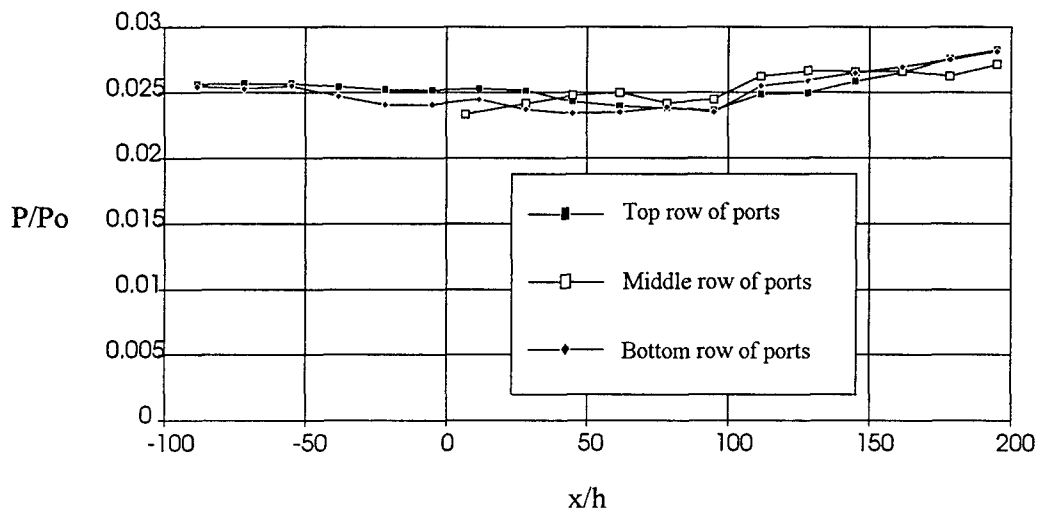


Figure 4.1 Low Re side wall pressure measurements.

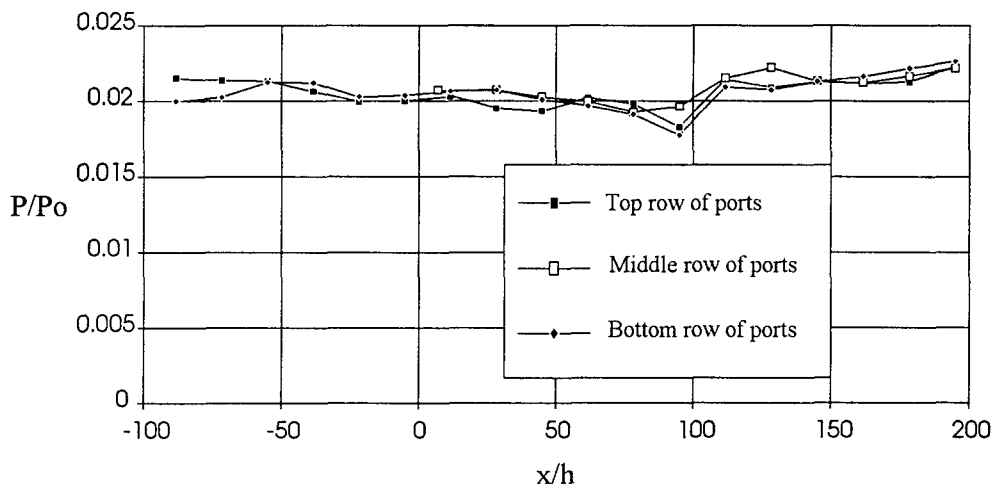
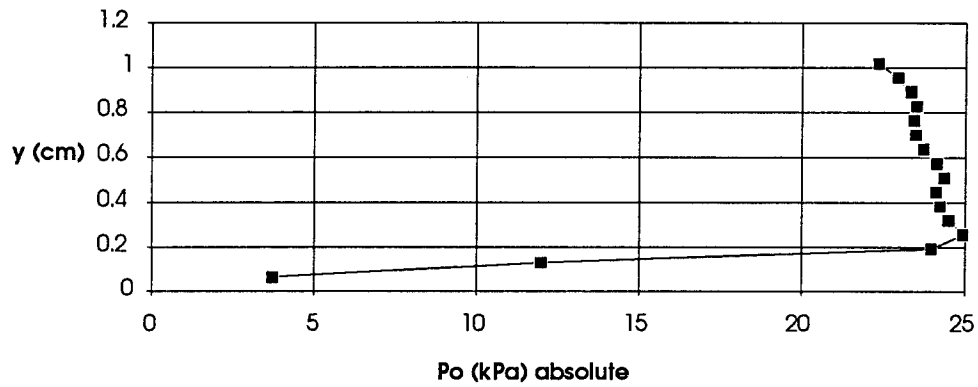
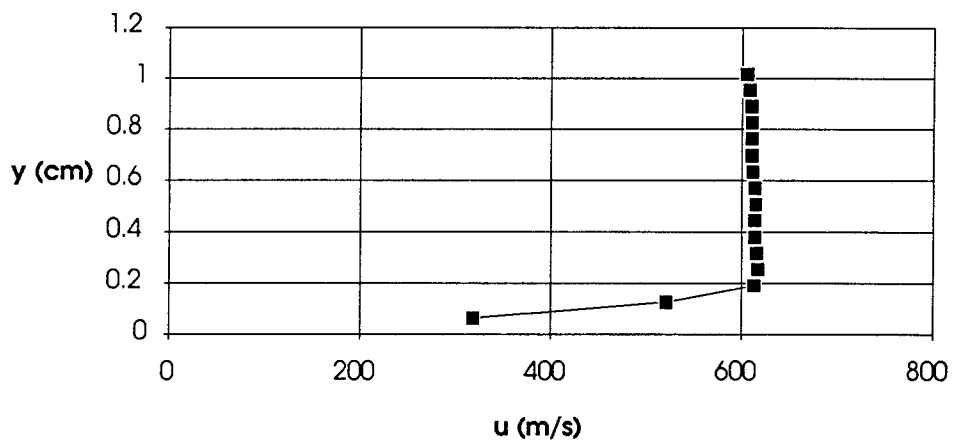


Figure 4.2 High Re side wall pressure measurements.

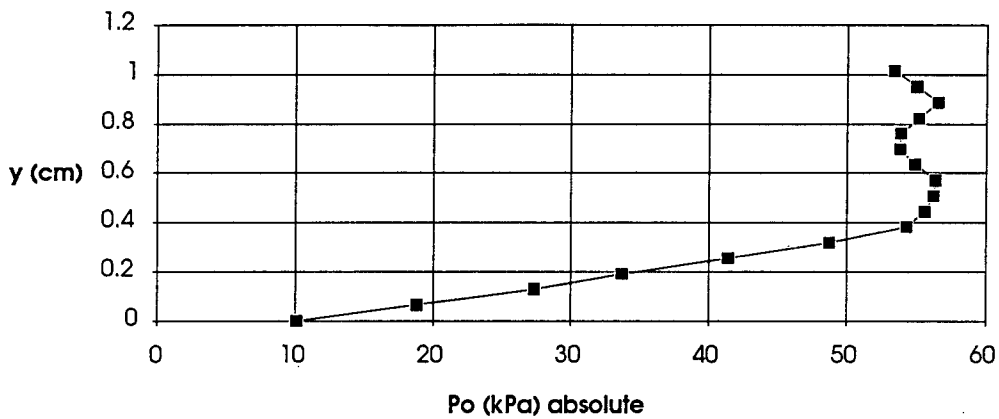


(a)

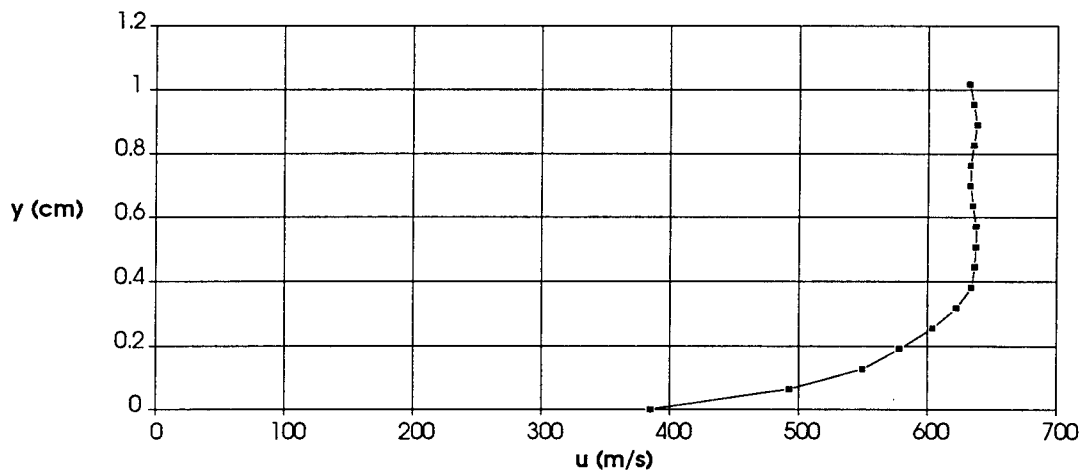


(b)

Figure 4.3 Low Re, laminary boundary layer (a) Pitot probe pressure measurements and (b) corresponding velocity profile at $x = -0.94$ cm.

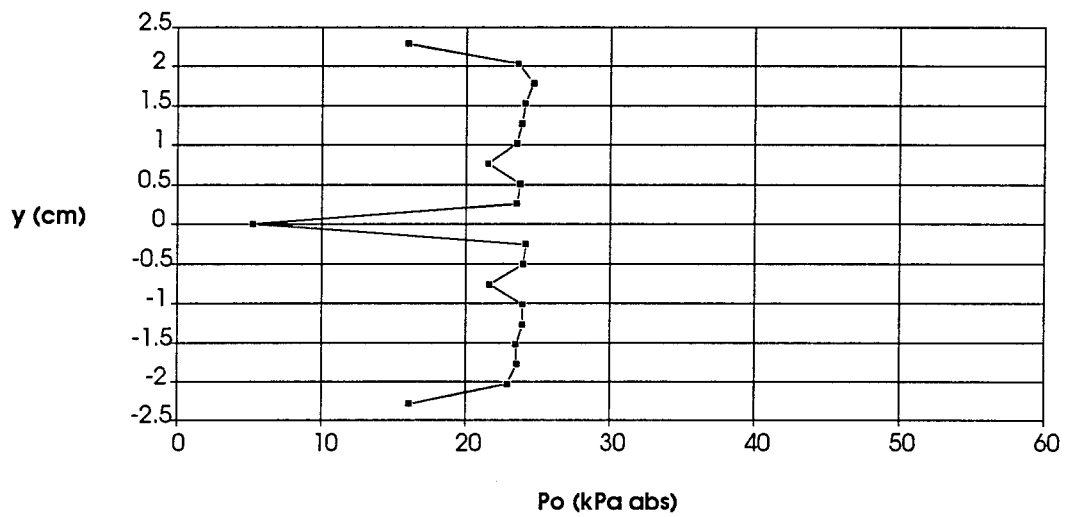


(a)

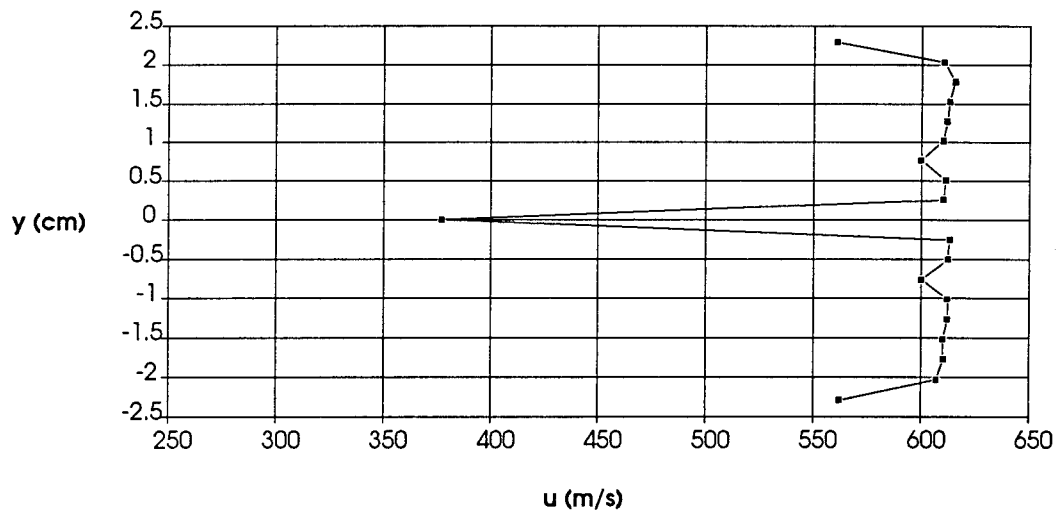


(b)

Figure 4.4 High Re, turbulent boundary layer (a) Pitot probe pressure measurements and (b) corresponding velocity profile at $x = -0.94$ cm.

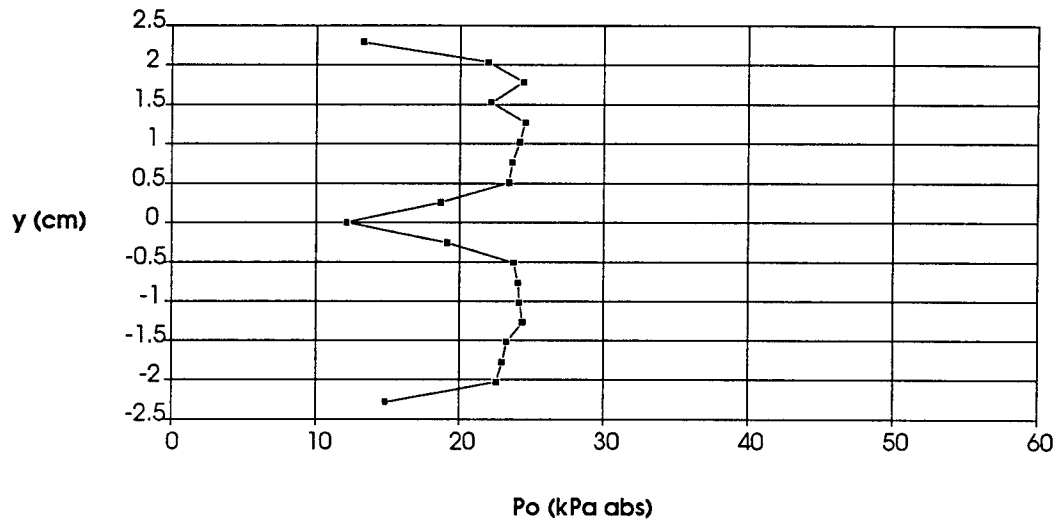


(a)

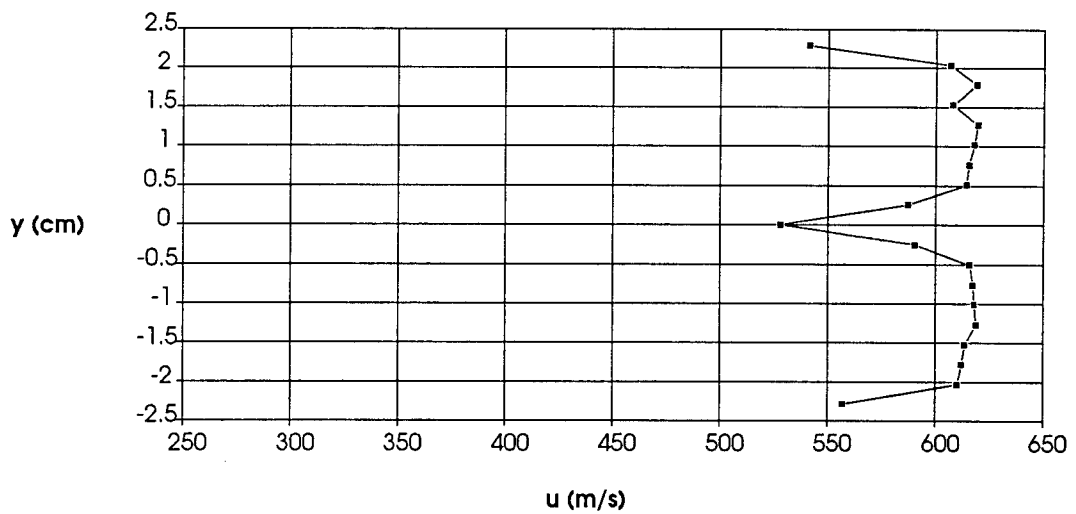


(b)

Figure 4.5 Low Re, (a) Pitot probe pressure measurement and (b) corresponding velocity profile of the wake at $x = 1.98$ cm.

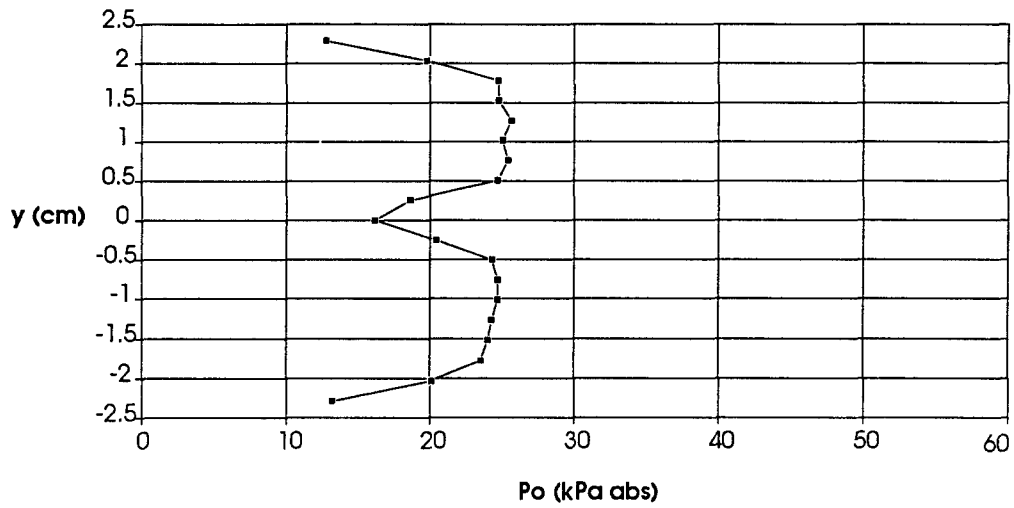


(a)

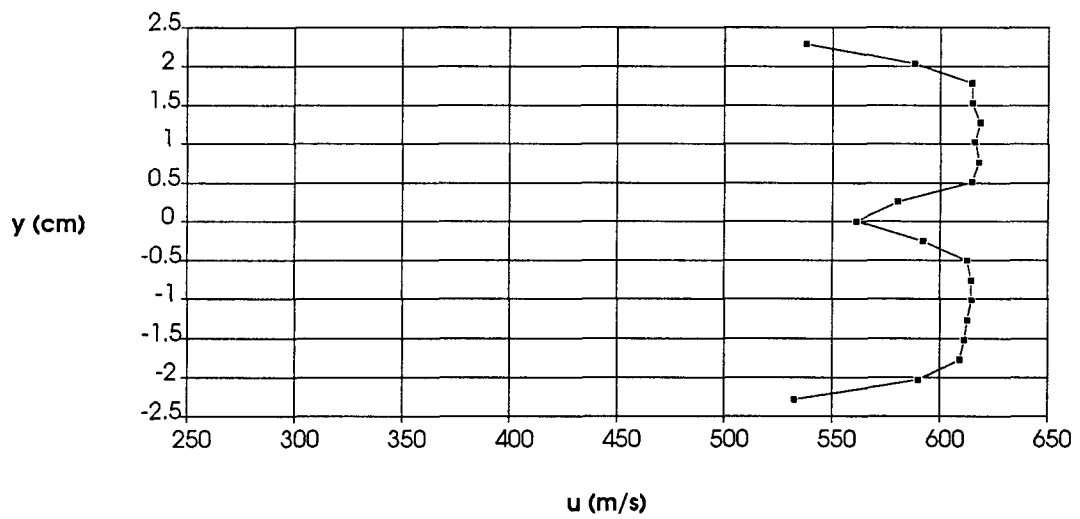


(b)

Figure 4.6 Low Re, (a) Pitot probe pressure measurements and (b) corresponding velocity profile of the wake at $x = 5.08$ cm.

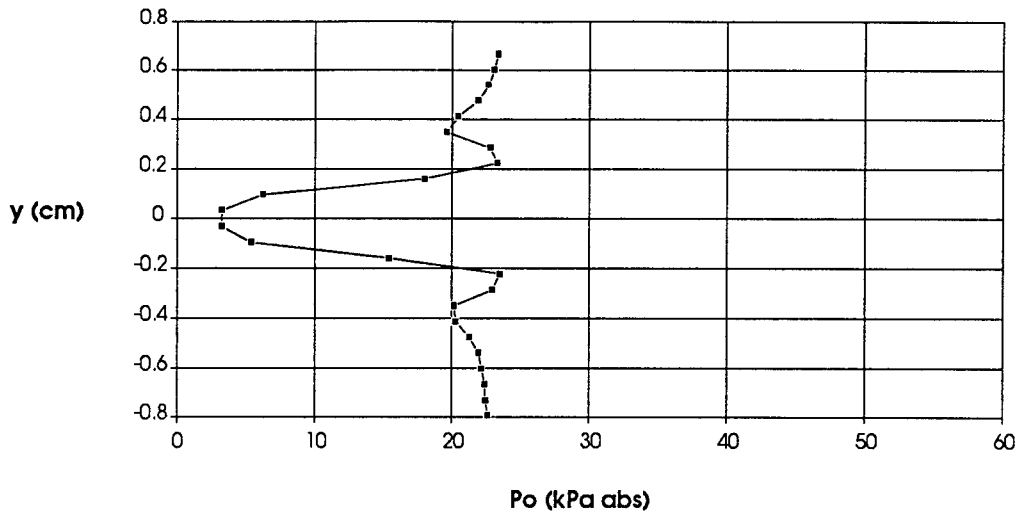


(a)

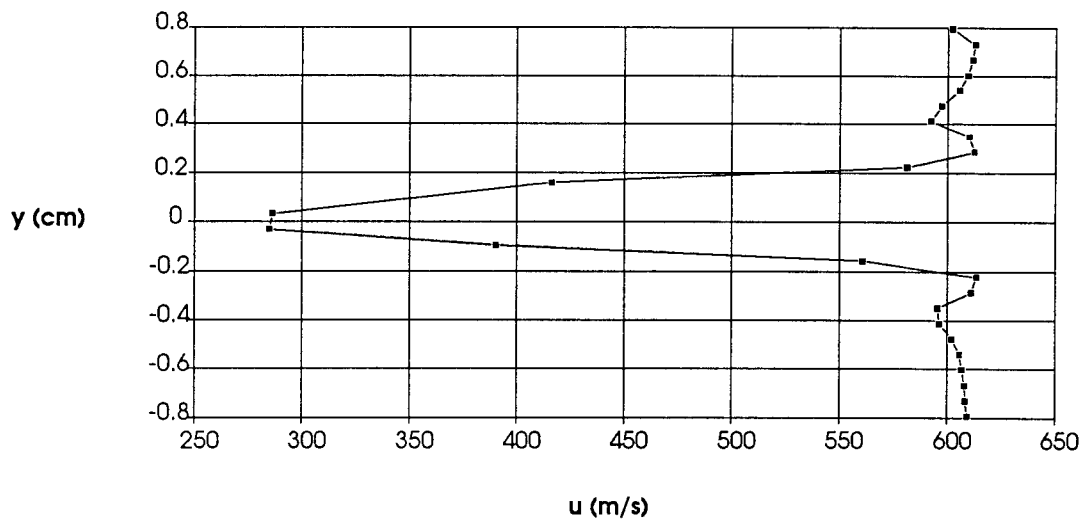


(b)

Figure 4.7 Low Re, (a) Pitot probe pressure measurements and (b) corresponding velocity profile of the wake at $x = 8.13$ cm.

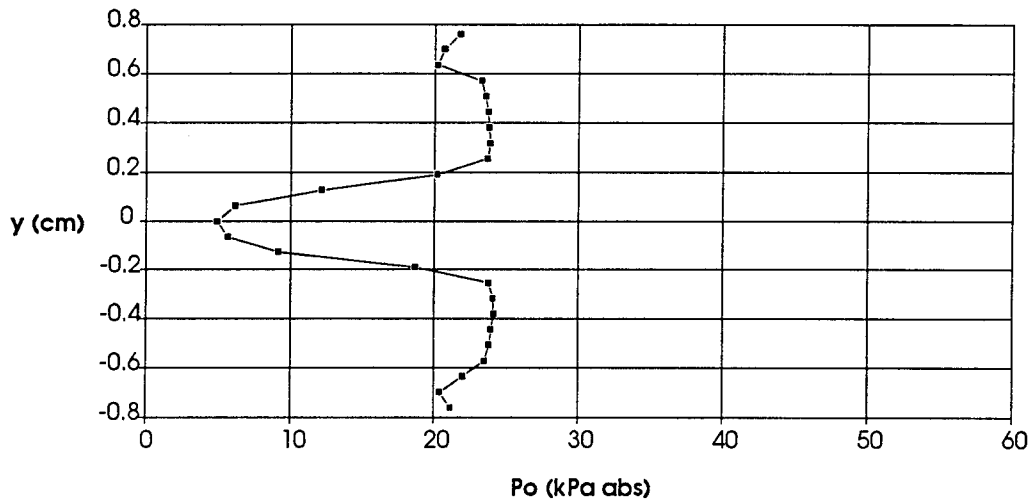


(a)

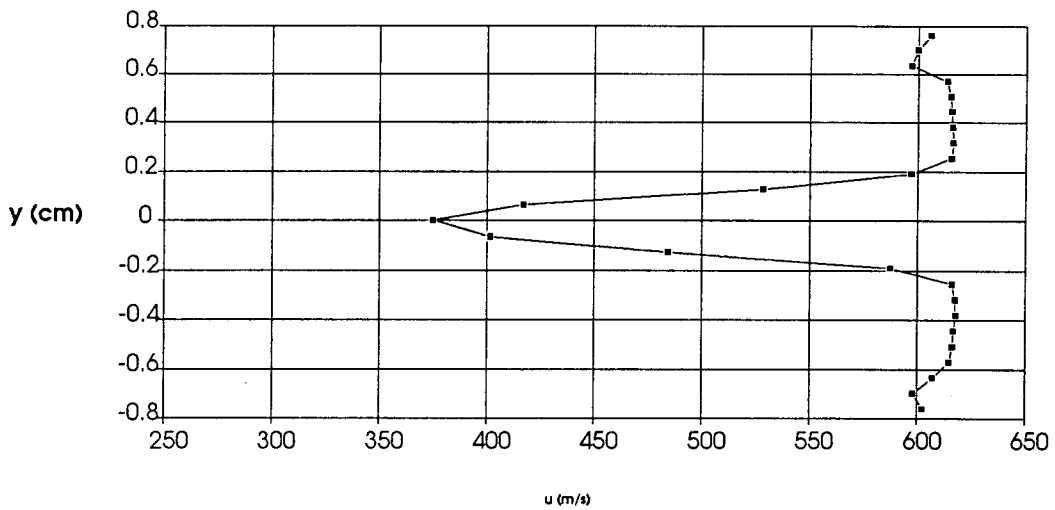


(b)

Figure 4.8 Low Re, high resolution (a) Pitot probe pressure measurements and (b) corresponding velocity profile of the wake at $x = 0.69$ cm.

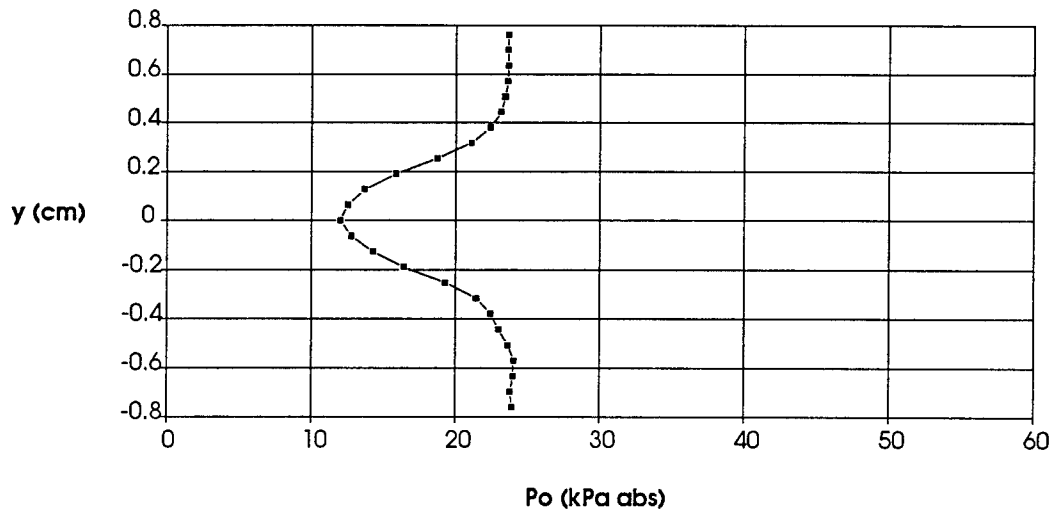


(a)

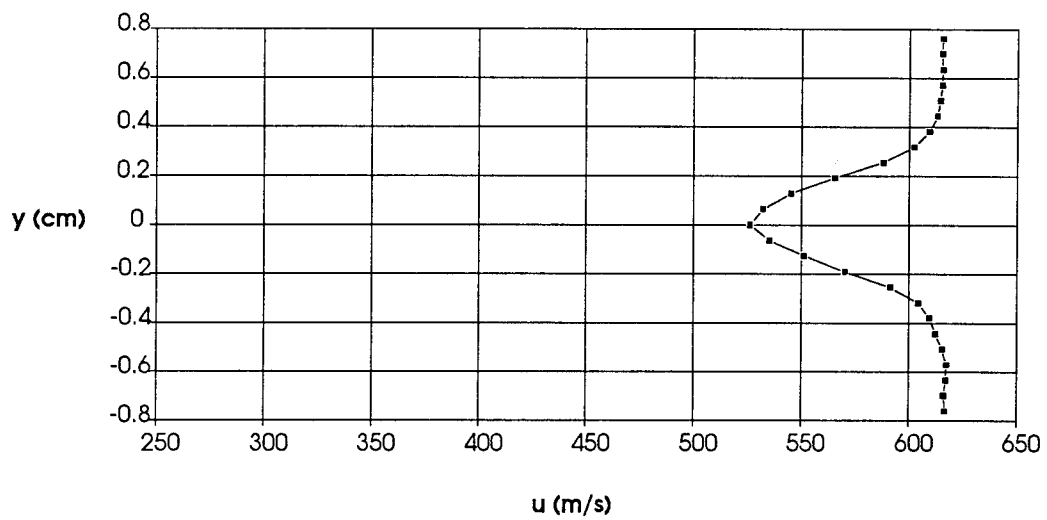


(b)

Figure 4.9 Low Re, high resolution (a) Pitot probe pressure measurements and (b) corresponding velocity profile of the wake at $x = 1.98$ cm.

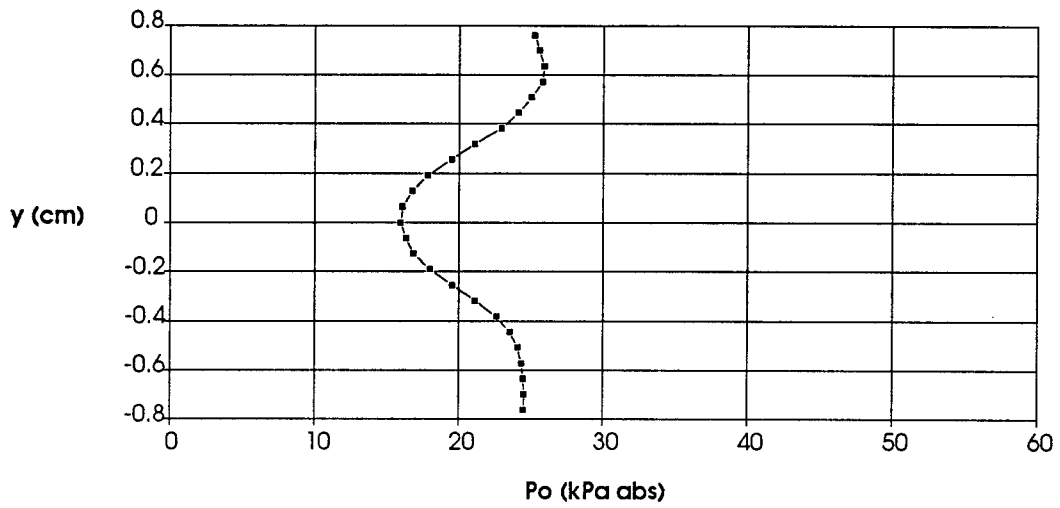


(a)

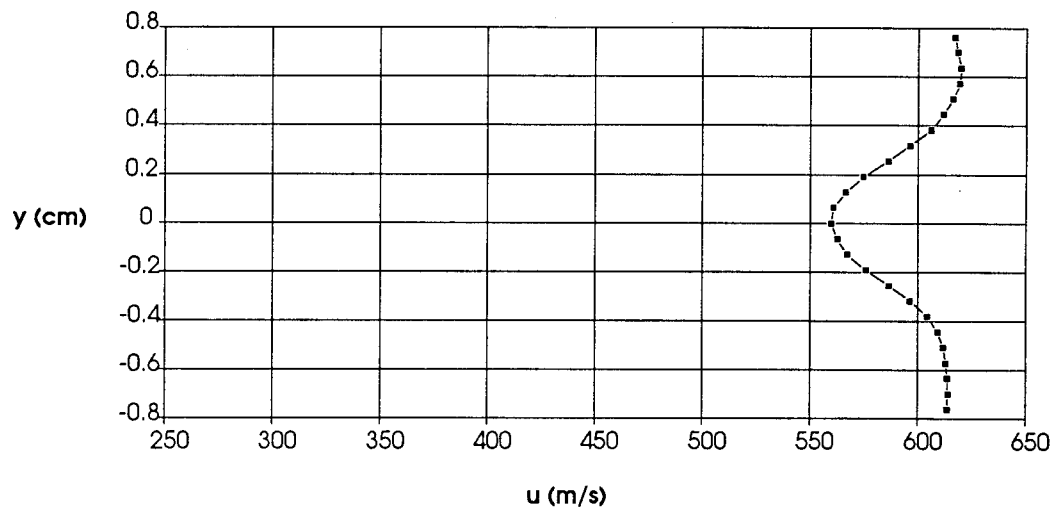


(b)

Figure 4.10 Low Re, high resolution (a) Pitot probe pressure measurements and (b) corresponding velocity profile of the wake at $x = 5.08$ cm.



(a)



(b)

Figure 4.11 Low Re, high resolution (a) Pitot probe pressure measurements and (b) corresponding velocity profile of the wake at $x = 8.13$ cm.

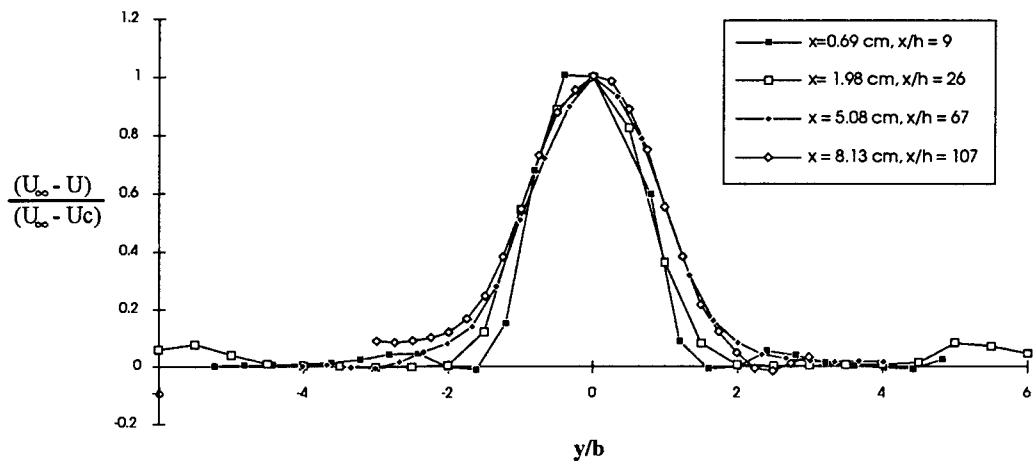
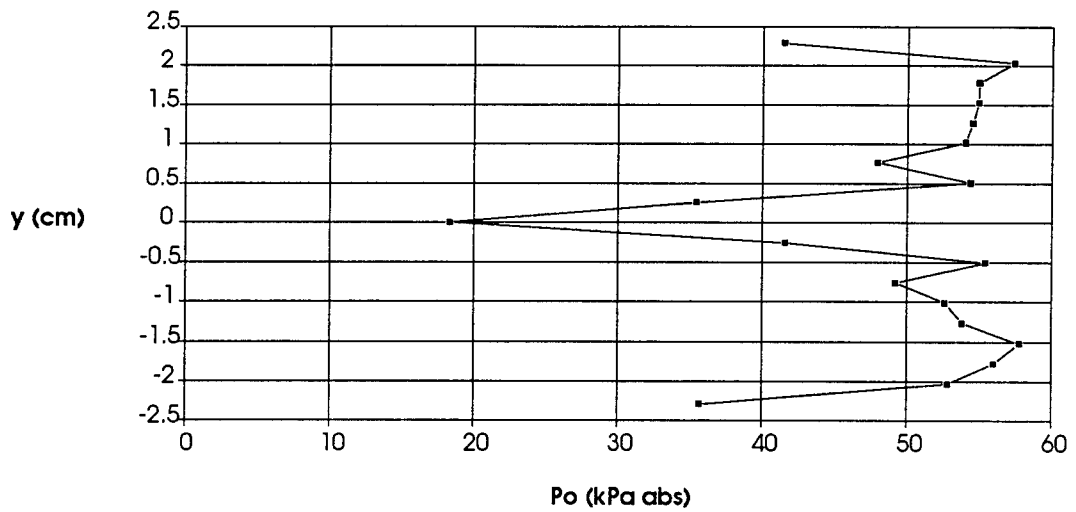
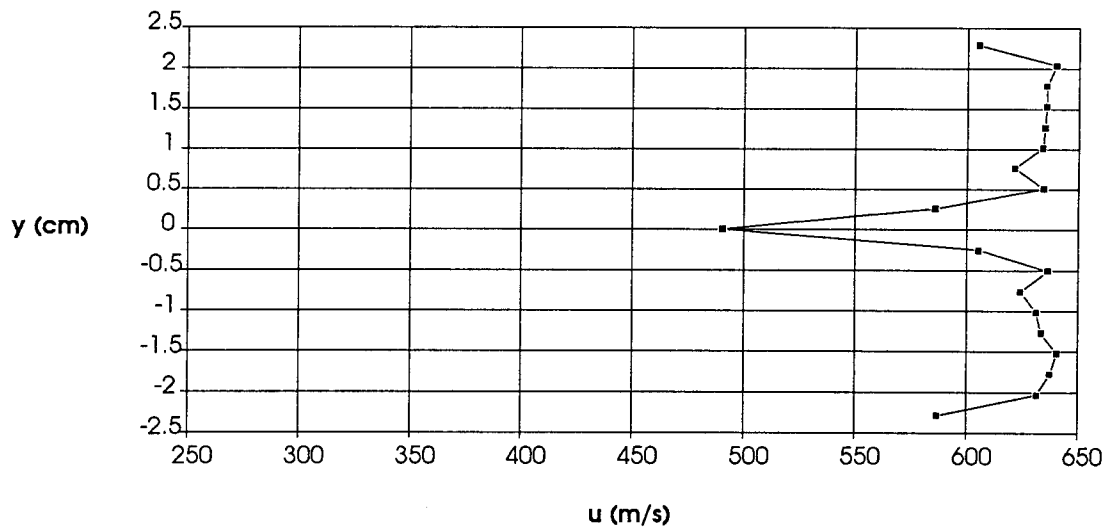


Figure 4.12 Plotted normalized scales show self-similarity of the low Re wake for $x > 5.08 \text{ cm}$.

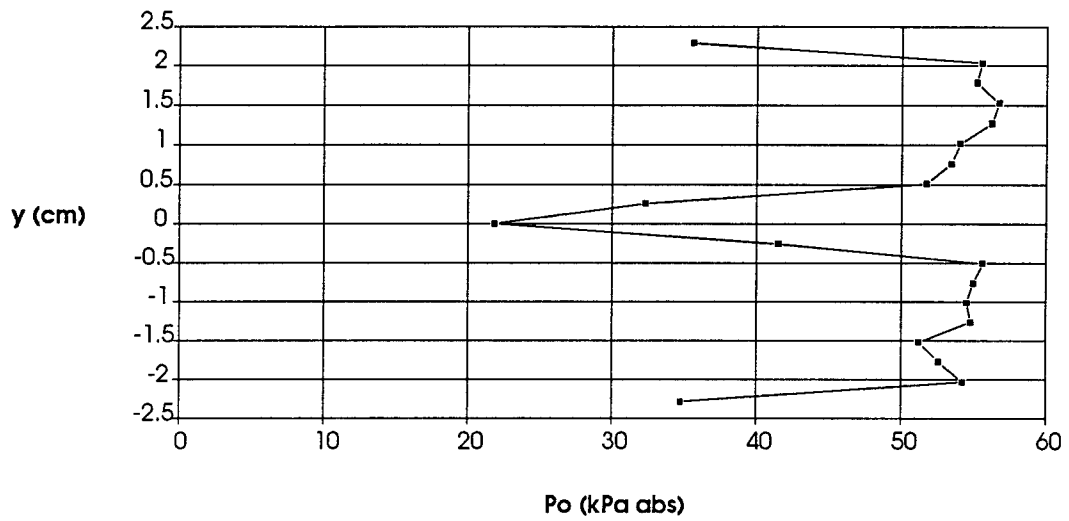


(a)

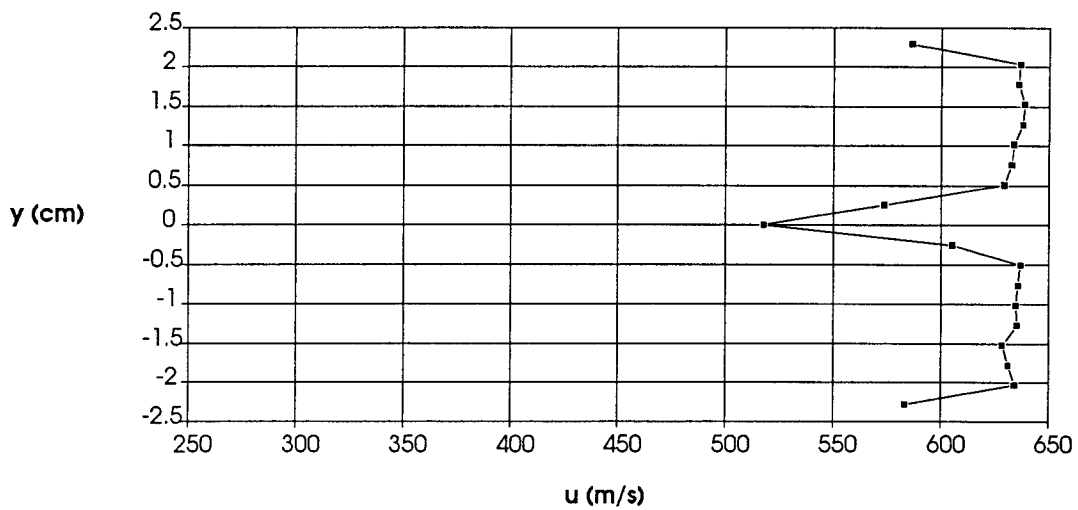


(b)

Figure 4.13 High Re (a) Pitot probe pressure measurements and (b) corresponding velocity profile of the wake at $x = 1.98$ cm.

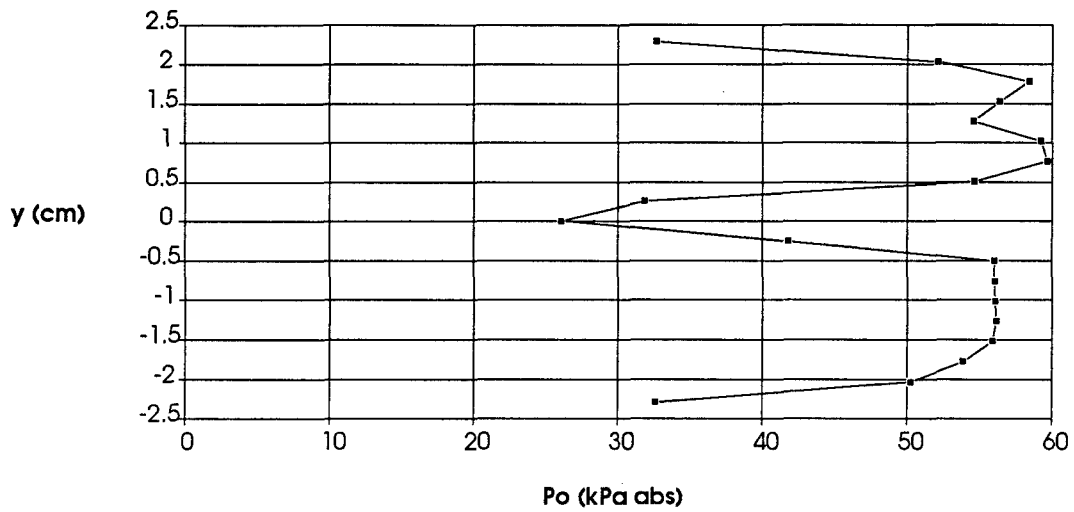


(a)

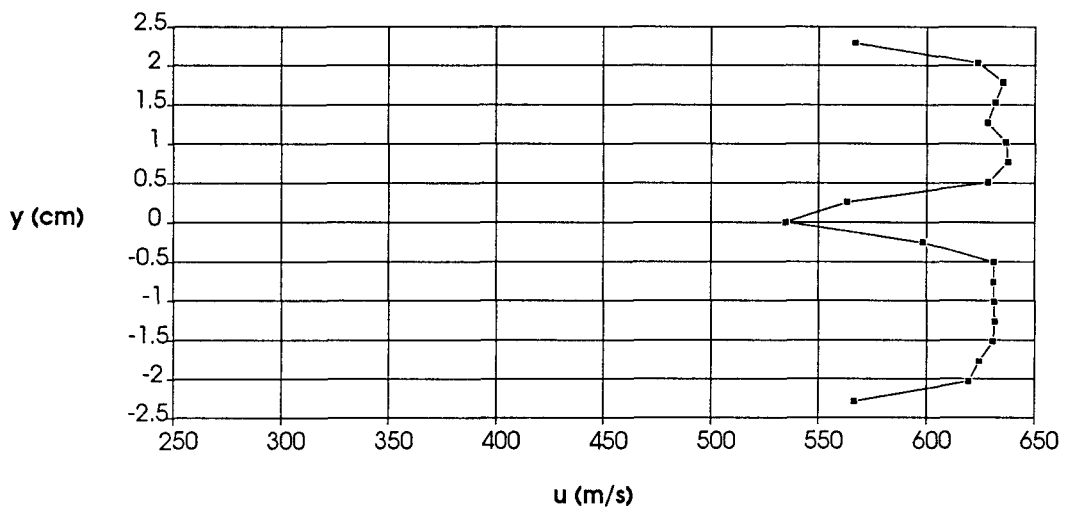


(b)

Figure 4.14 High Re, (a) Pitot probe pressure measurements and (b) corresponding velocity profile of the wake at $x = 5.08$ cm.

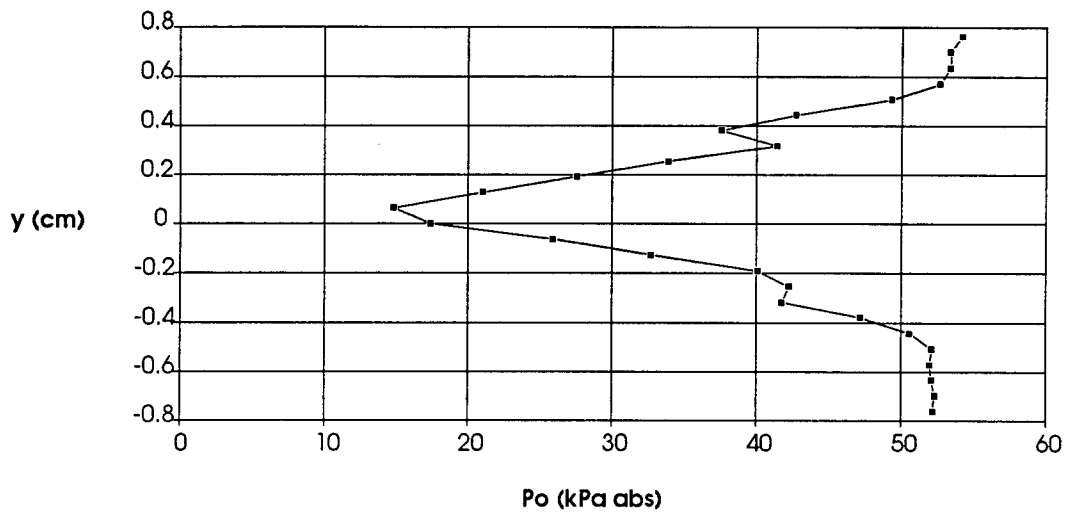


(a)

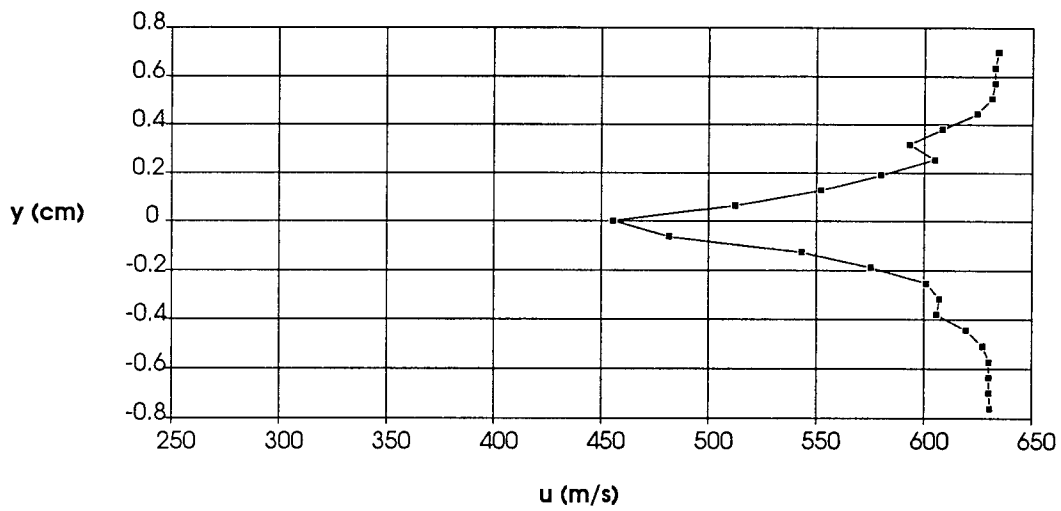


(b)

Figure 4.15 High Re, (a) Pitot probe pressure measurements and (b) corresponding velocity profile of the wake at $x = 8.13$ cm.

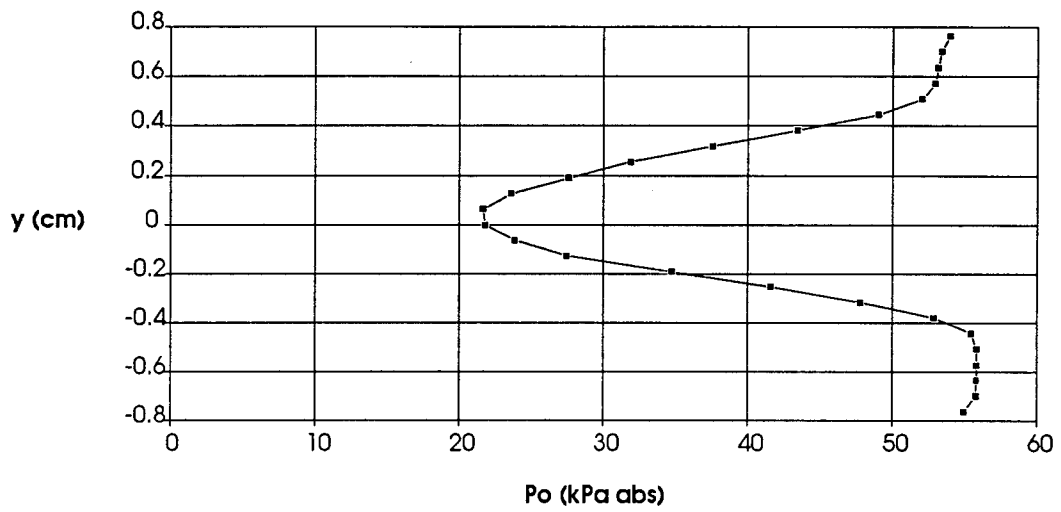


(a)

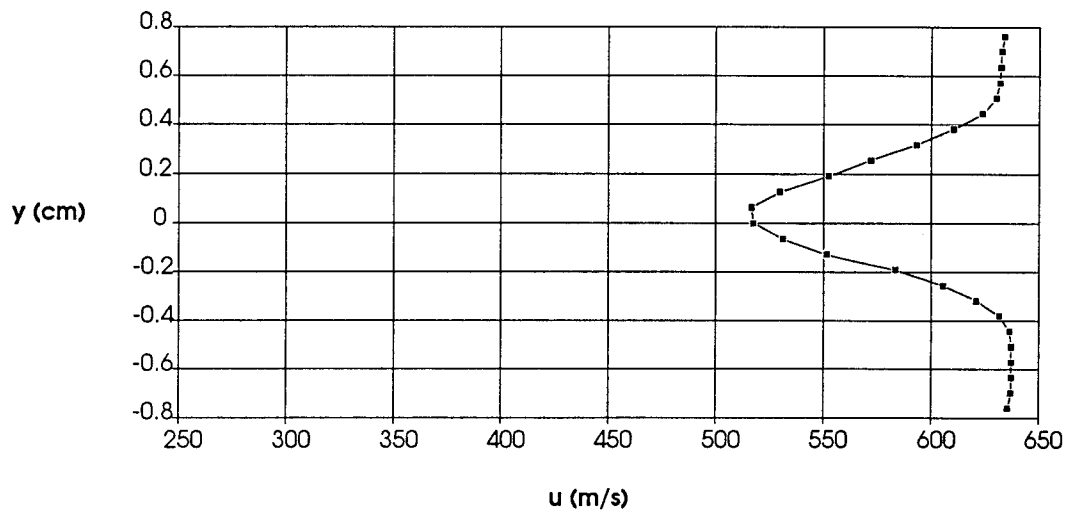


(b)

Figure 4.16 High Re, high resolution (a) Pitot probe pressure measurements and (b) corresponding velocity profile of the wake at $x = 0.69$ cm.

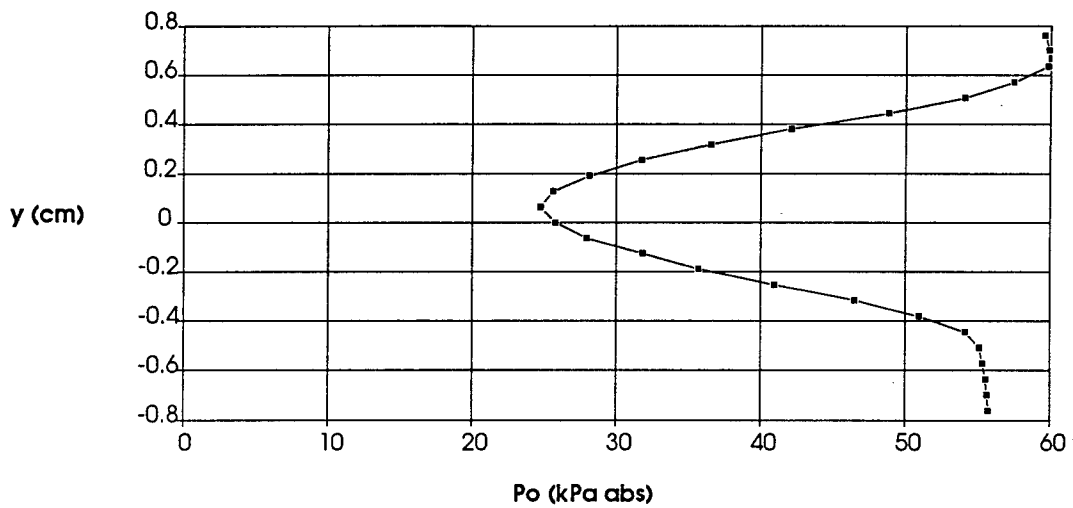


(a)

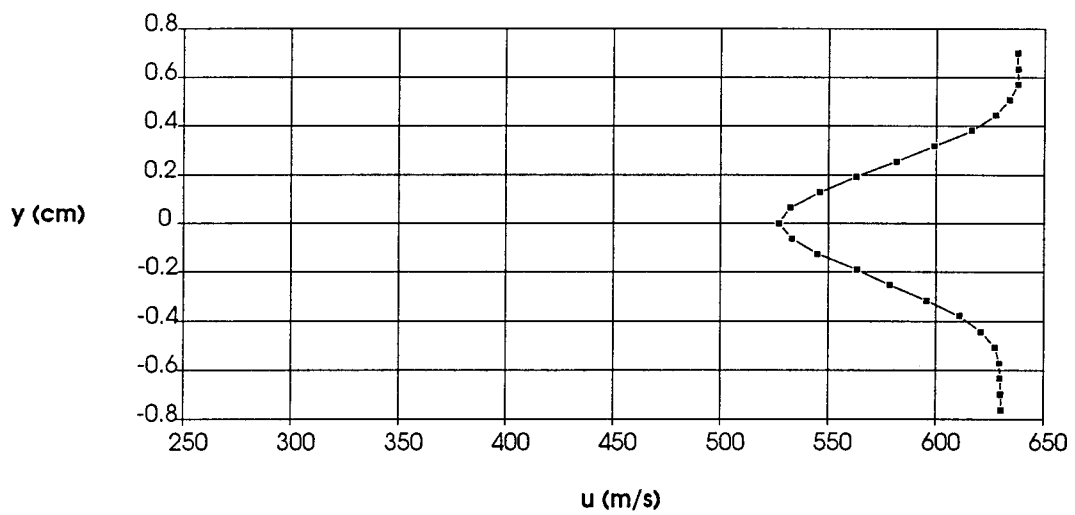


(b)

Figure 4.17 High Re, high resolution (a) Pitot probe pressure measurements and (b) corresponding velocity profile of the wake at $x = 5.08$ cm.



(a)



(b)

Figure 4.18 High Re, high resolution (a) Pitot probe pressure measurements and (b) corresponding velocity profile of the wake at $x = 8.13$ cm.

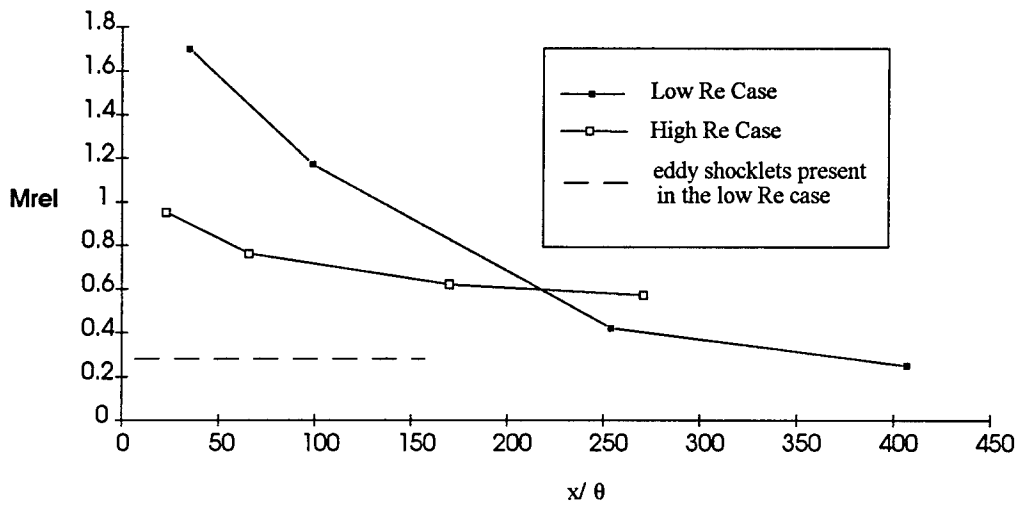


Figure 4.19 M_{rel} vs x/θ and eddy shocklets existence in the wake.

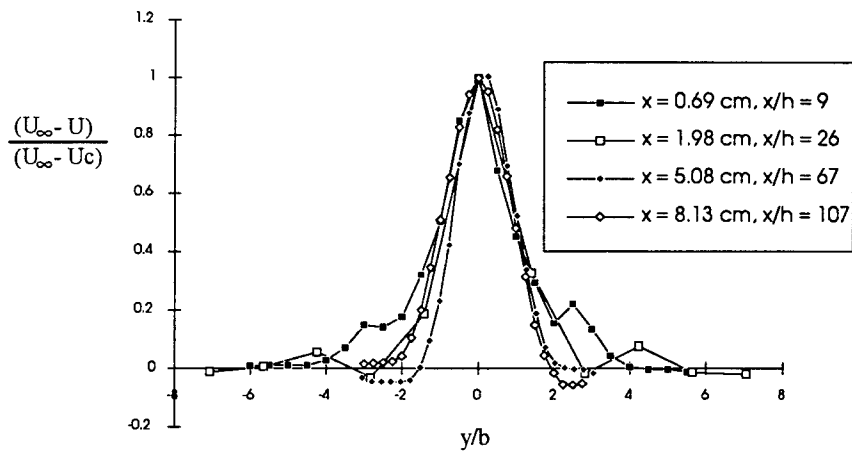


Figure 4.20 Plotted normalized scales show self-similarity of the high Re wake.

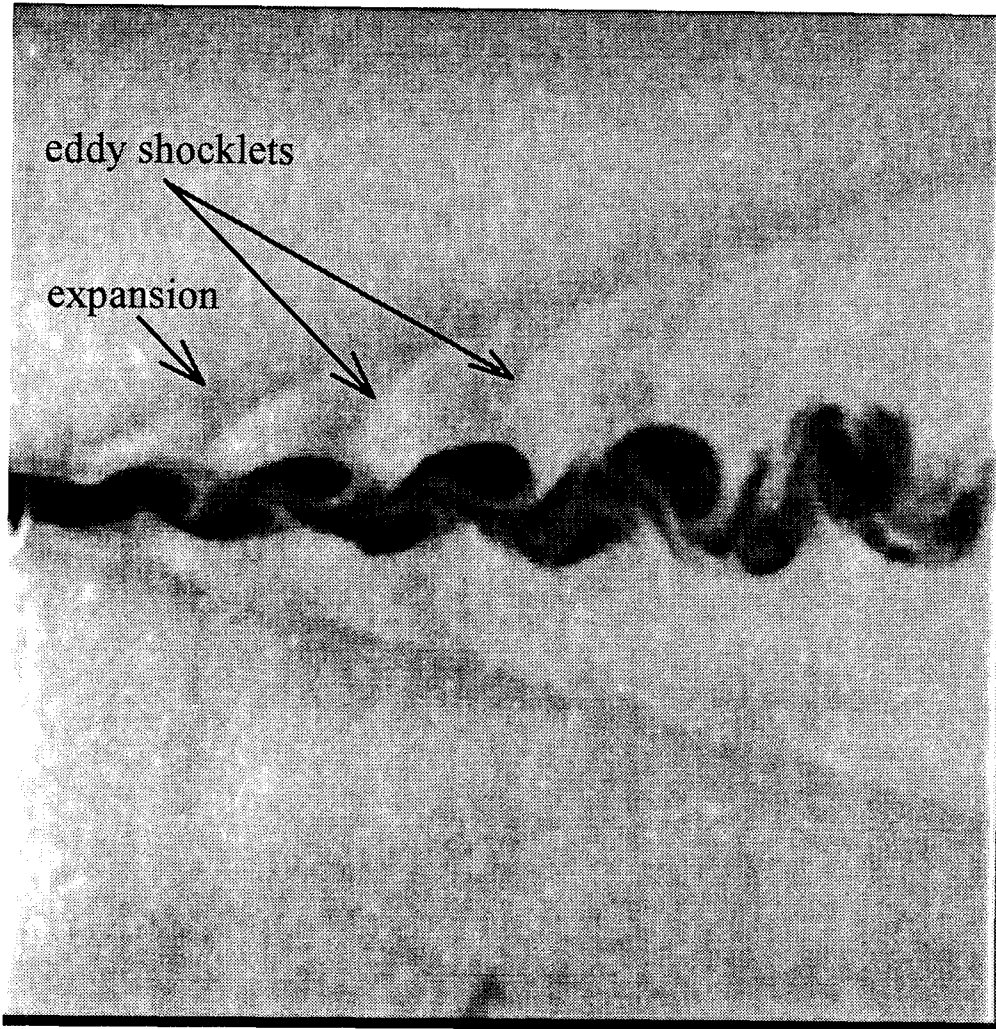


Figure 4.21 Far view taken from the side. X is from 0.58 cm to 4.45.

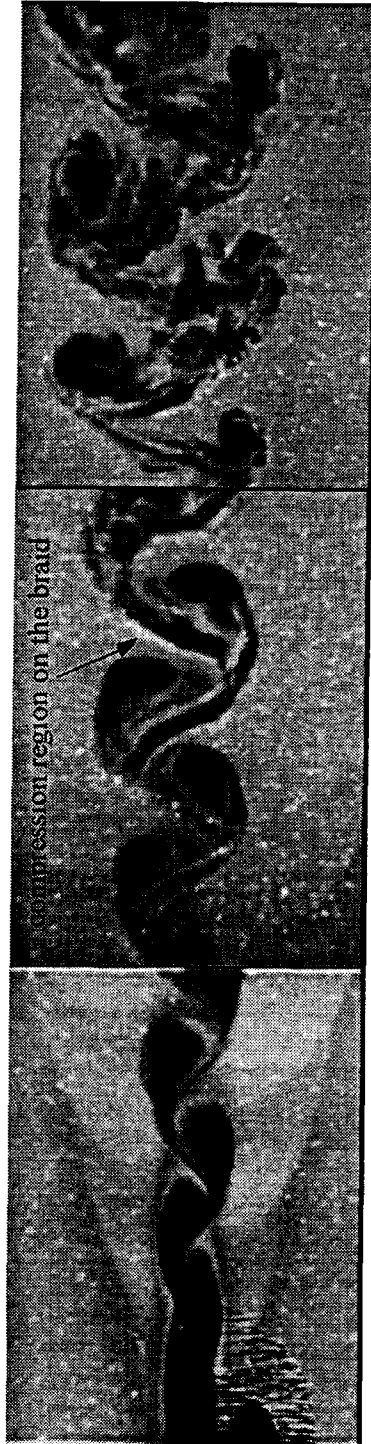


Figure 4.22 Low Re, close up side view showing $x = 0.13$ to $x = 6.22$ cm.

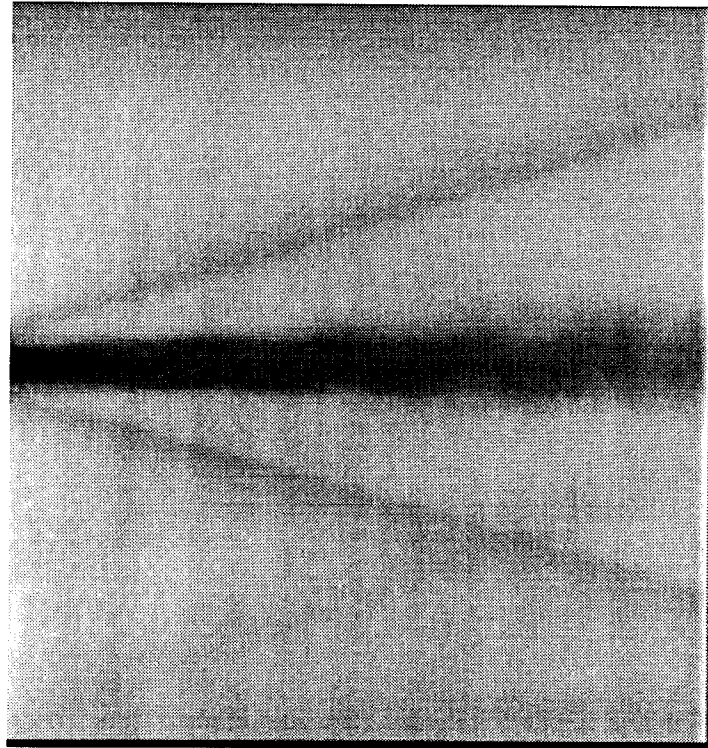


Figure 4.23 Low Re time averaged far side view. X is from 0.58 to 4.45 cm.

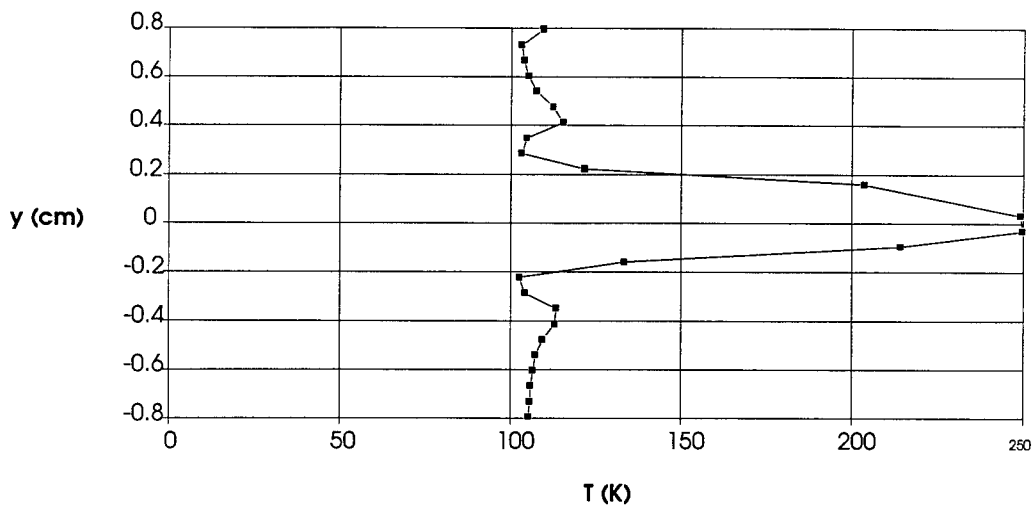


Figure 4.24 Low Re case, temperature profile across the wake at $x = 0.69$ cm. The wake was assumed to be adiabatic.

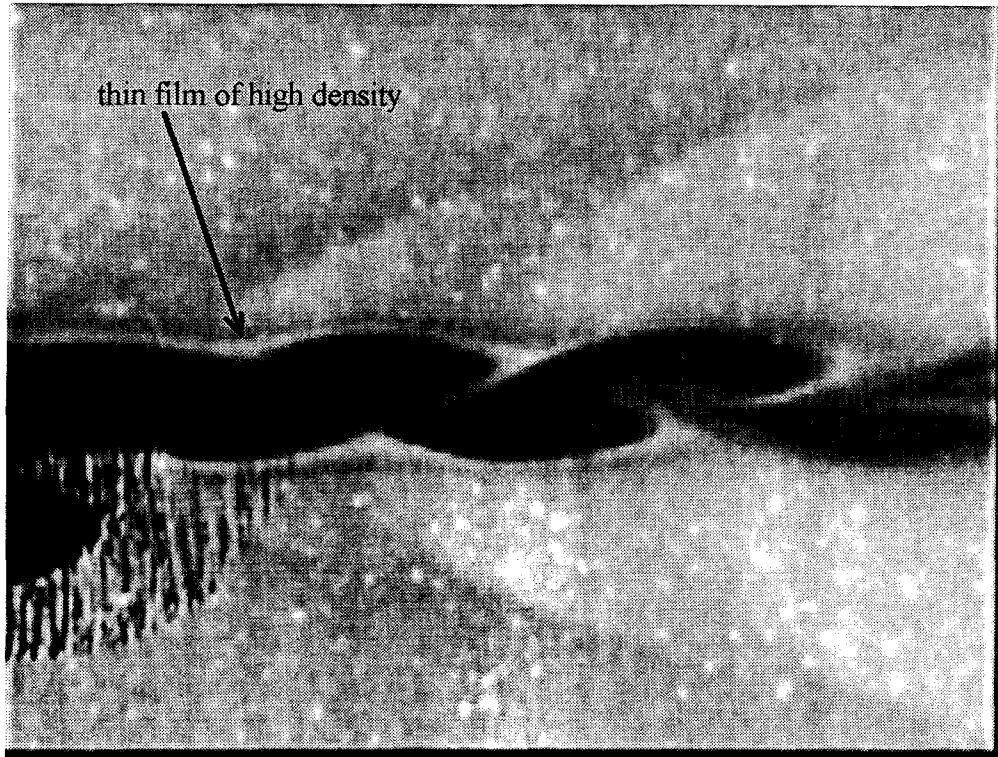


Figure 4.25 Low Re close up side view. X is from 0 to 2 cm.

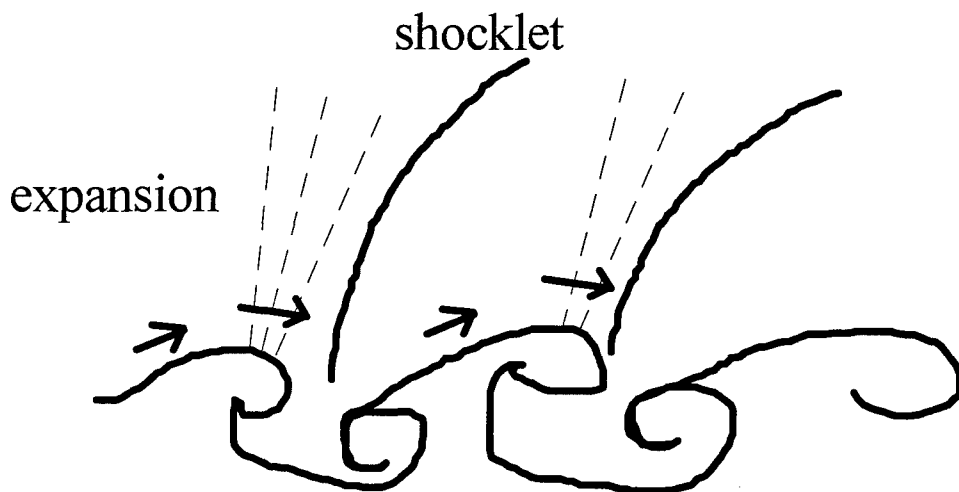


Figure 4.26 Schematic of eddy shocklets seen in the side view images. The dashed lines are expansions.

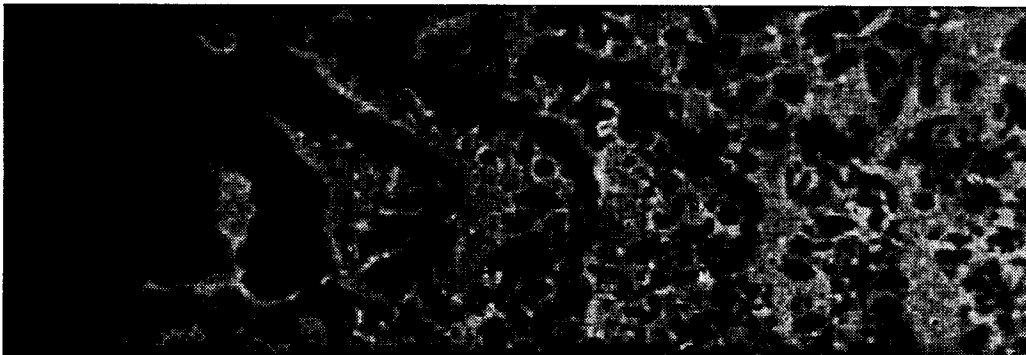


Figure 4.27 Low Re, far plan view with laser sheet level cutting the wake centerline. X is from -0.25 to 5 cm.

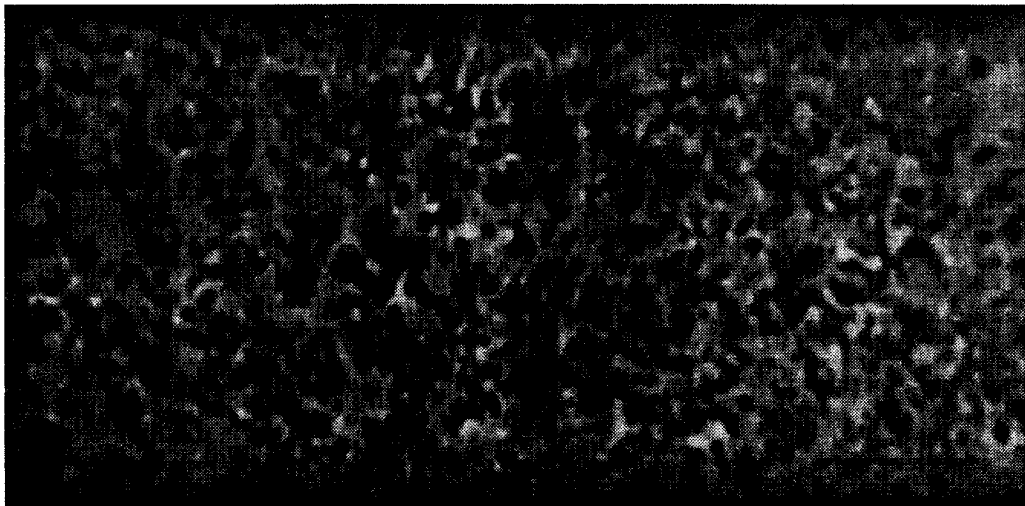


Figure 4.28 Low Re, far plan view with laser sheet cutting the centerline,
 $x = 4.8$ to 10.1 cm.

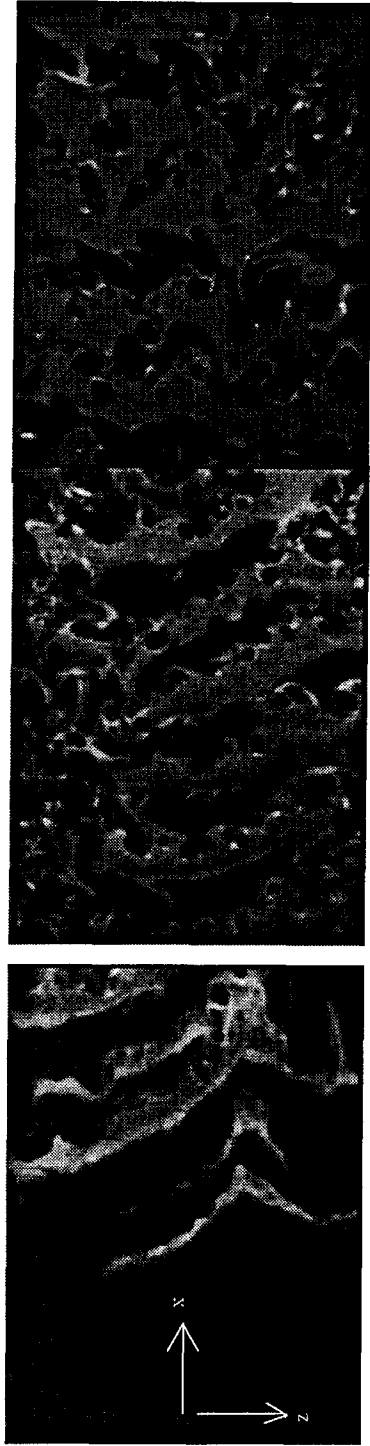


Figure 4.29 Low Re , close up plan view at the wake centerline. X is from 0 to 6.1 cm.

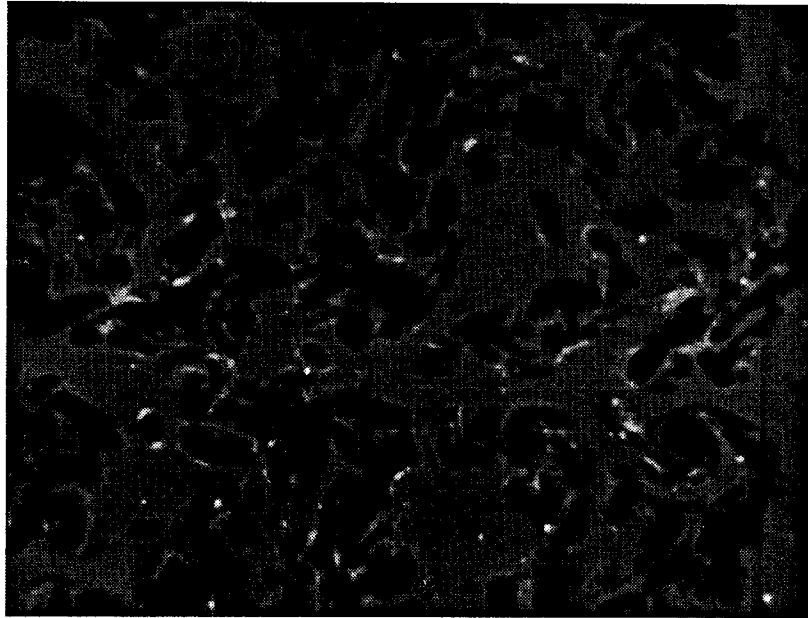


Figure 4.30 Low Re close up plan view. X is from 4 to 6.1 cm.

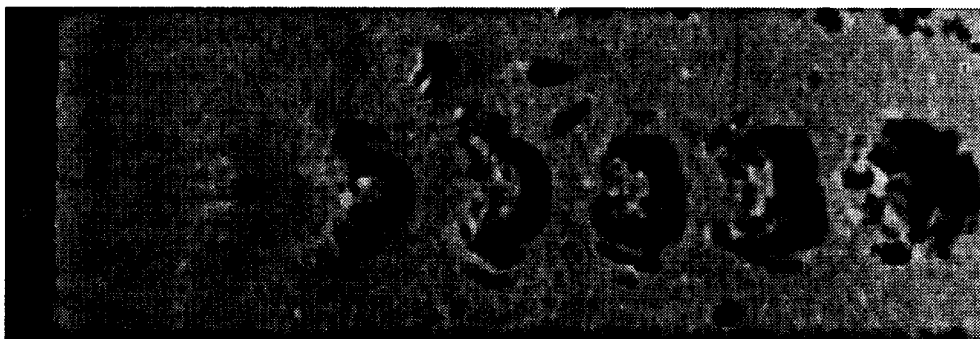


Figure 4.31 Low Re far plan view with the inclined laser sheet. X is from -0.25 to 5.08 cm.

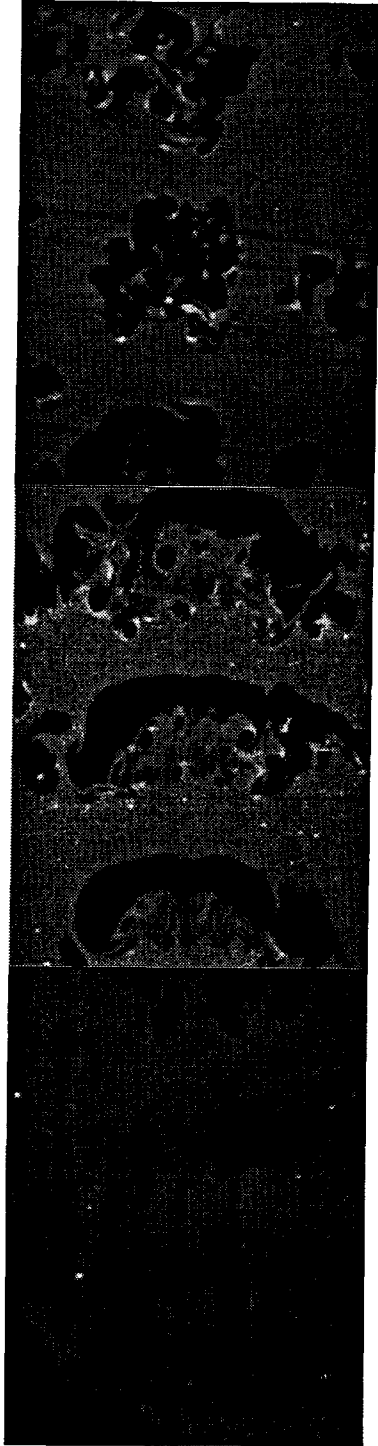


Figure 4.32 Low Re, close up plan view for the inclined laser sheet. X is from 0 to 6.1 cm.

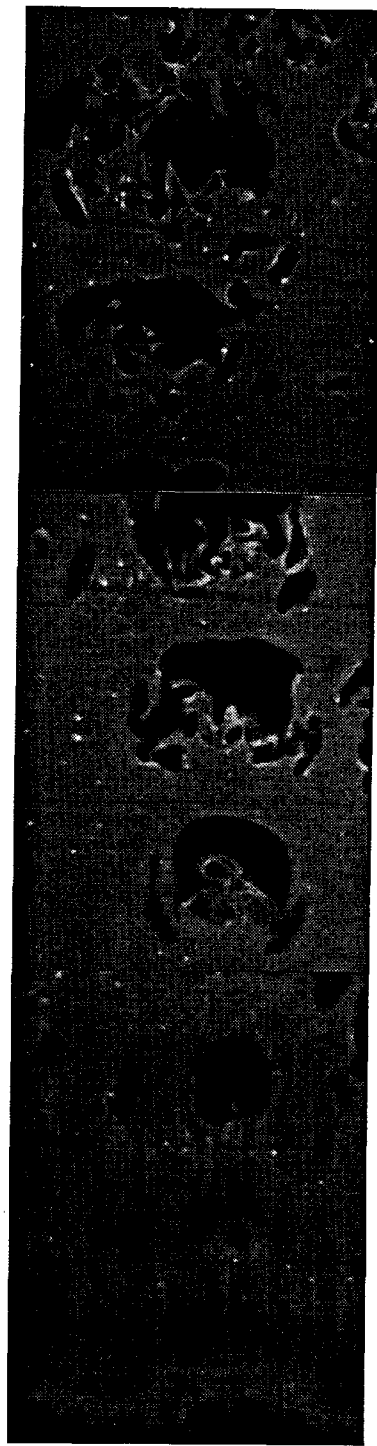


Figure 4.33 Low Re, close up plan view for the inclined laser sheet. X is from 0 to 6.1 cm.

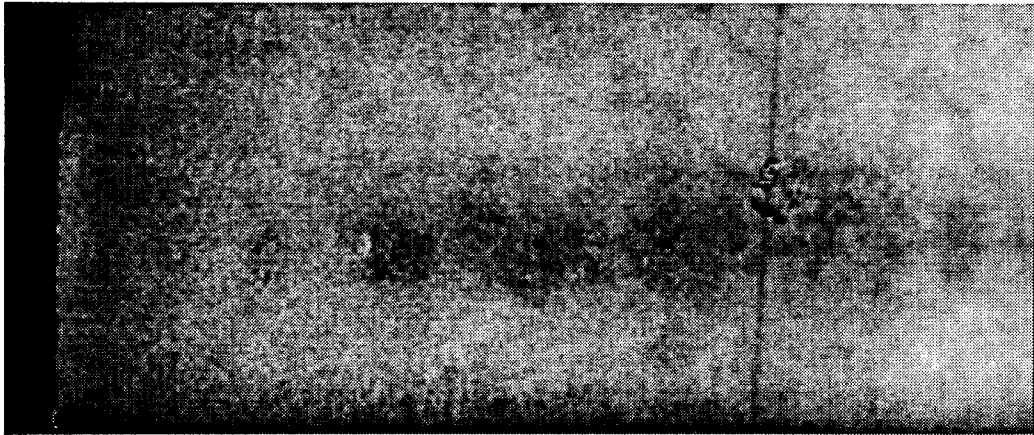


Figure 4.34 Low Re, 60 image average of the far plan view with the inclined laser sheet. X is from -0.25 to 5.08 cm.

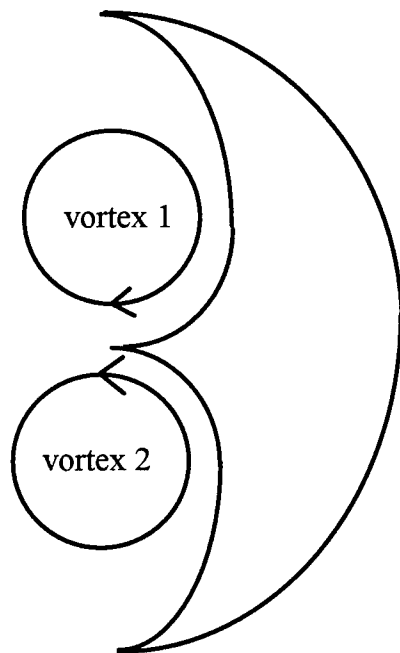


Figure 4.35 Schematic of third large scale structure in Fig. 4.32 showing counter rotating vortices enveloping boundary layer fluid.

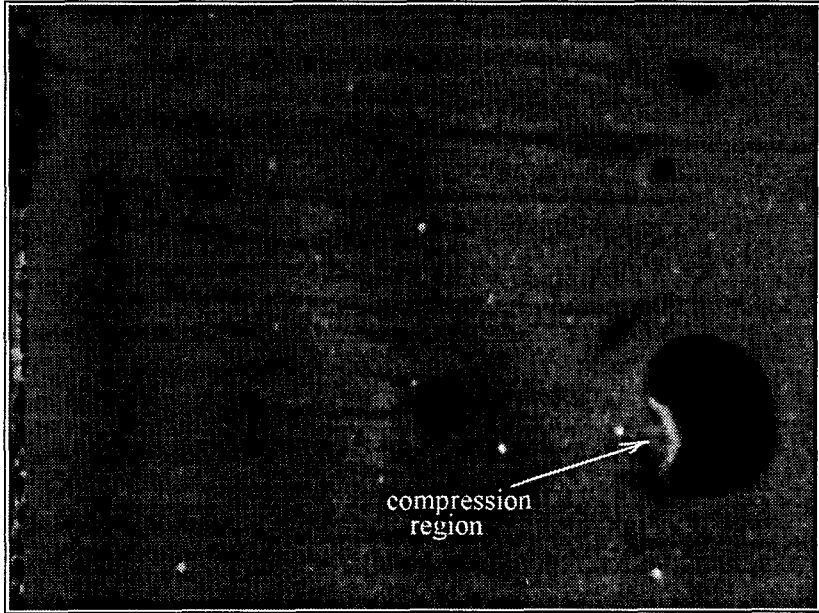


Figure 4.36 Low Re close up plan view. X is from 0 to 2 cm.

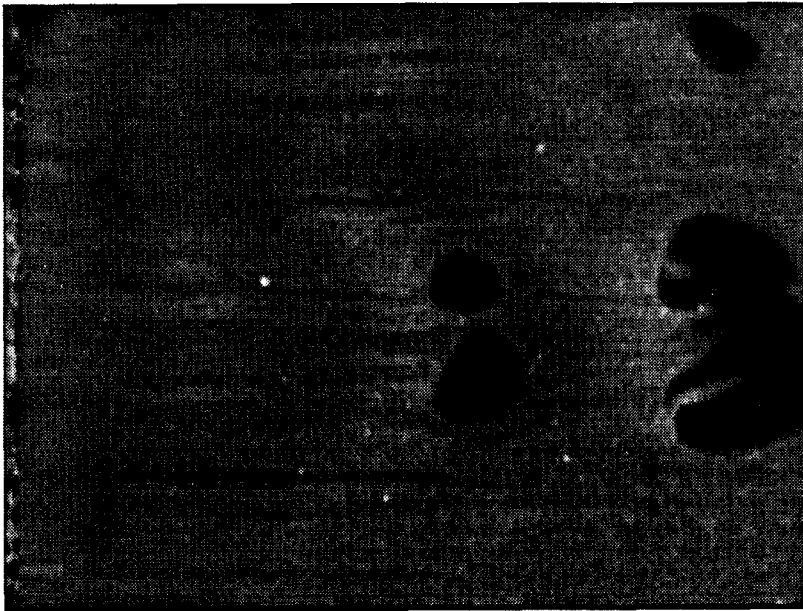
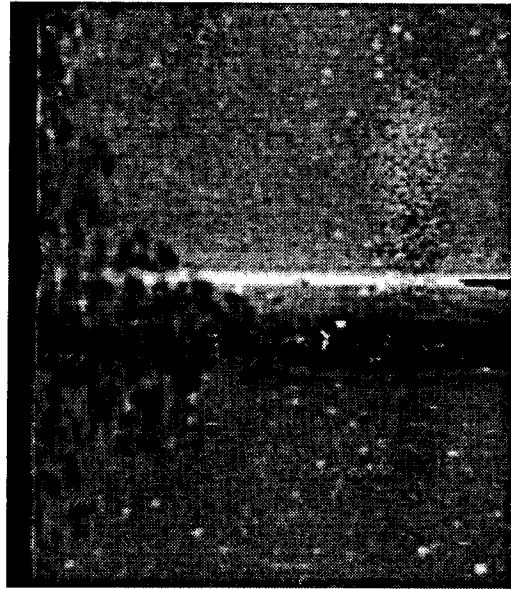
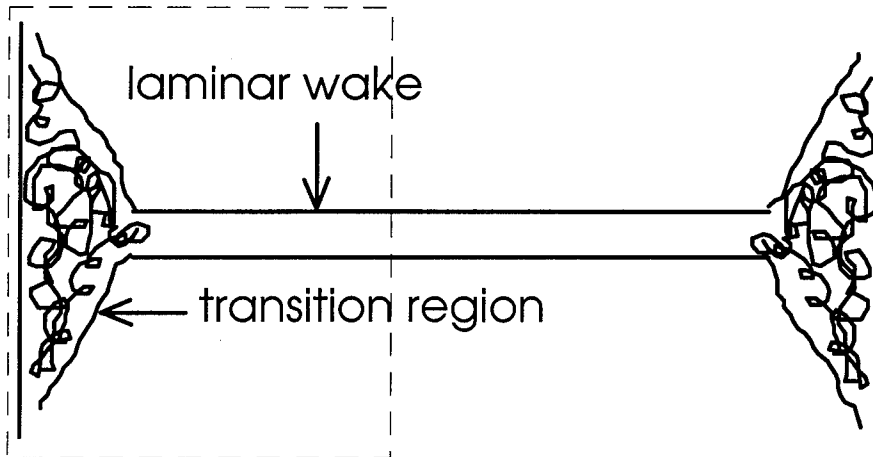


Figure 4.37 Low Re close up plan view. X is from 0 to 2 cm.



(a)



(b)

Figure 4.38 (a) Low Re , segment of an end view at $x = 0.25$ cm and (b) schematic of the entire wake in an end view. The dotted segment shows the portion of the wake shown in (a).

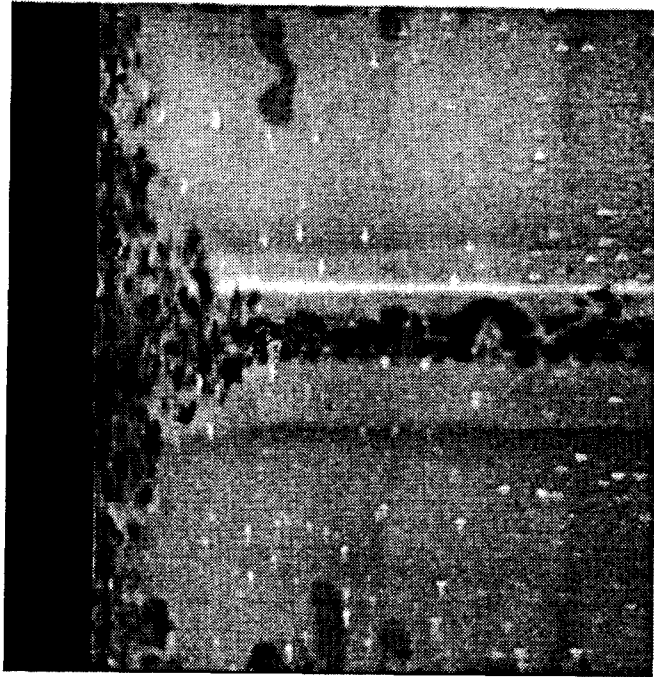


Figure 4.39 Low Re, end view at $x = 2$ cm. Spanwise field of view is 4 cm.

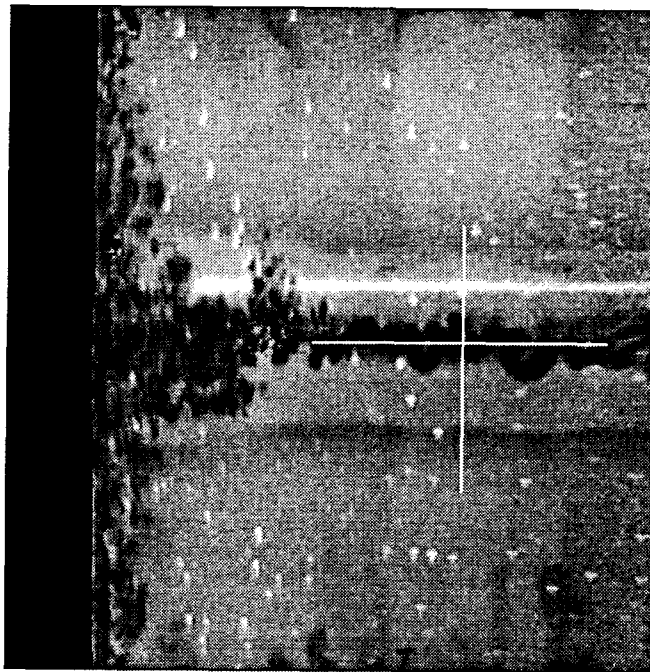


Figure 4.40 Low Re, end view at $x = 2$ cm. Spanwise field of view is 4 cm.

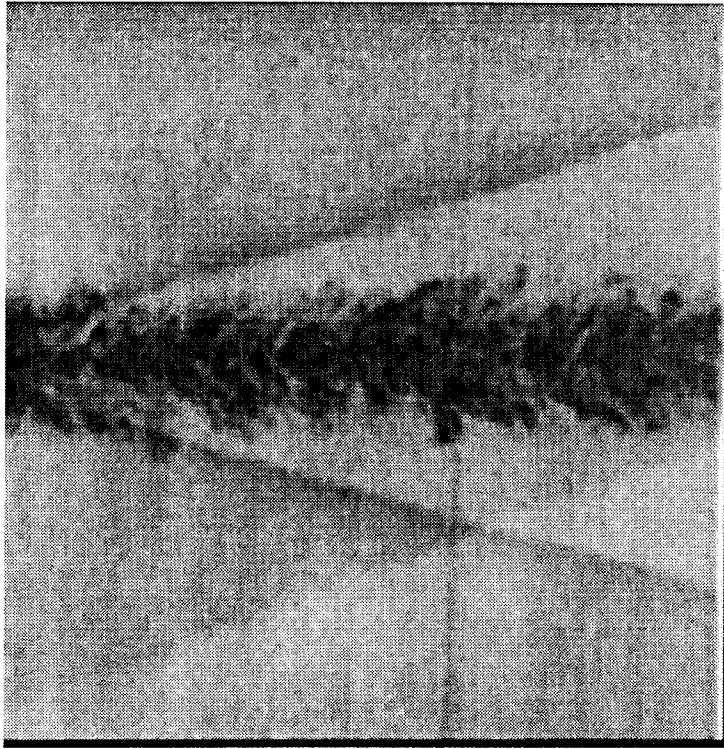


Figure 4.41 High Re, far side view. X is from 1.12 to 5.08 cm.

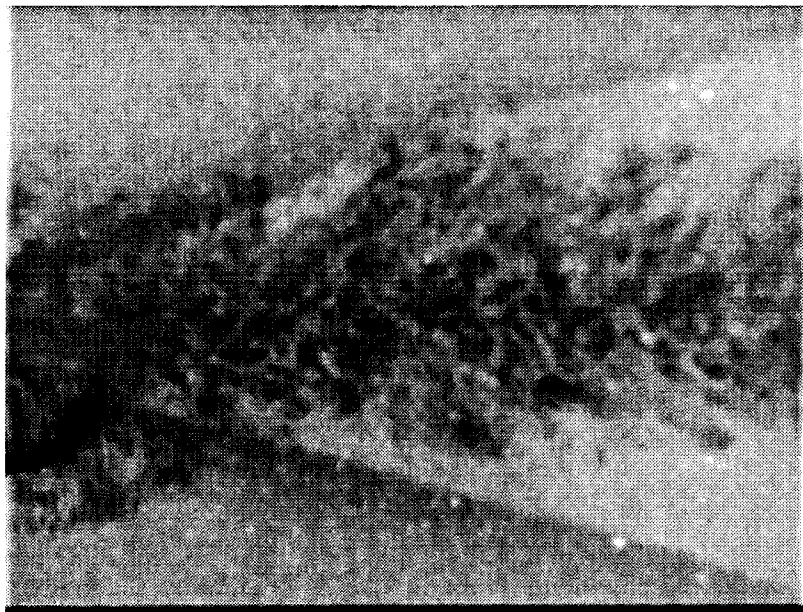


Figure 4.42 High Re, close up side view. $X = 0$ to 2 cm.

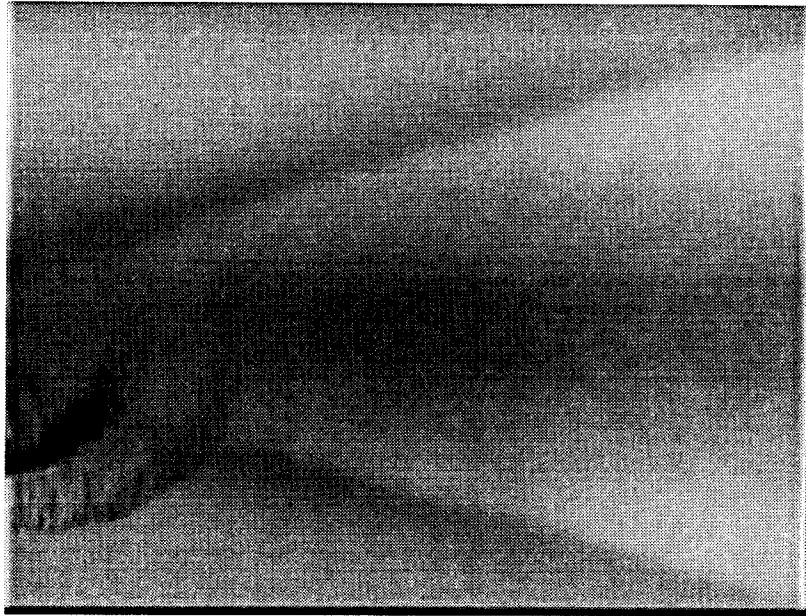


Figure 4.43 High Re, time averaged close up side view. $X = 0$ to 2 cm.

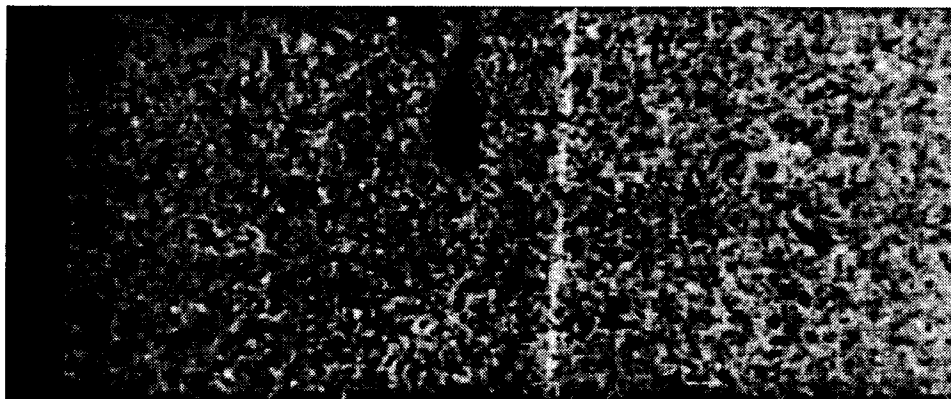


Figure 4.44 High Re, far plan view. $X = -0.25$ to 5.08 cm.

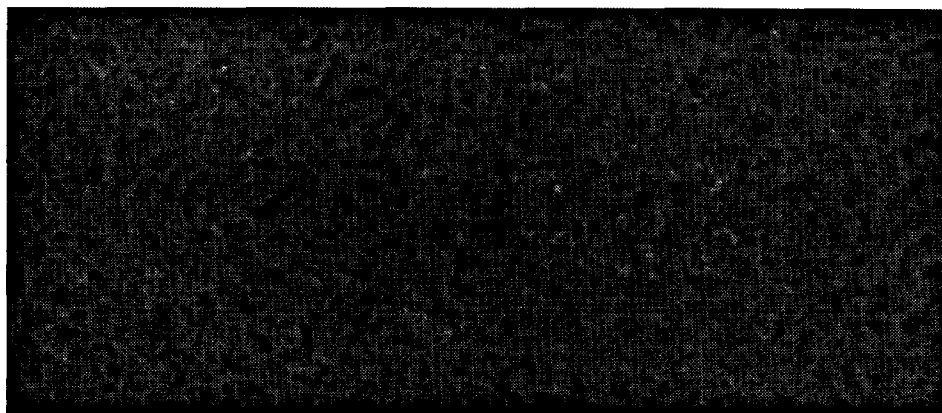


Figure 4.45 High Re, far plan view. $X = 5$ to 10 cm.

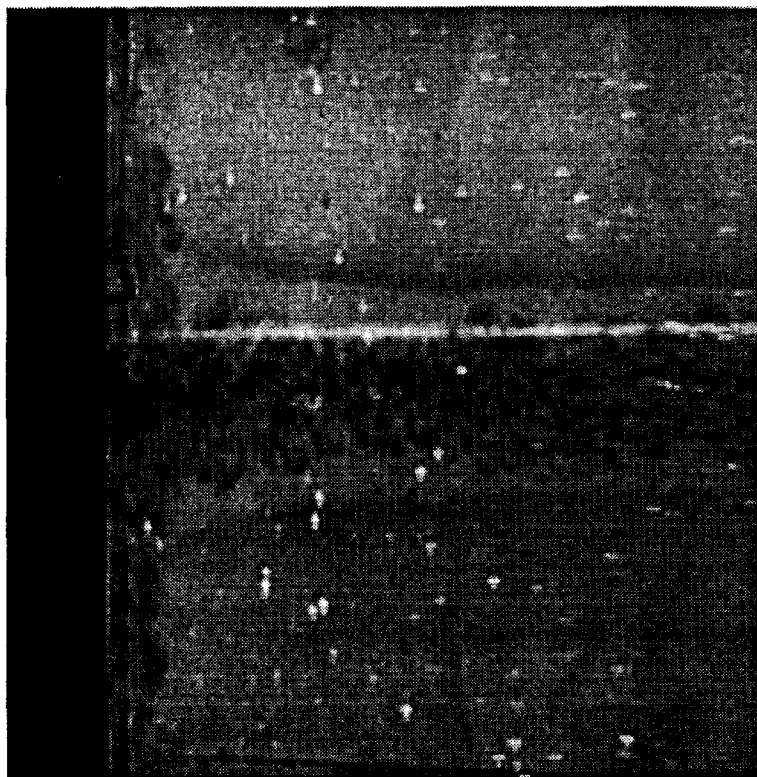


Figure 4.46 High Re, end view at $x = 2$ cm. Field of view is 4.4 cm.

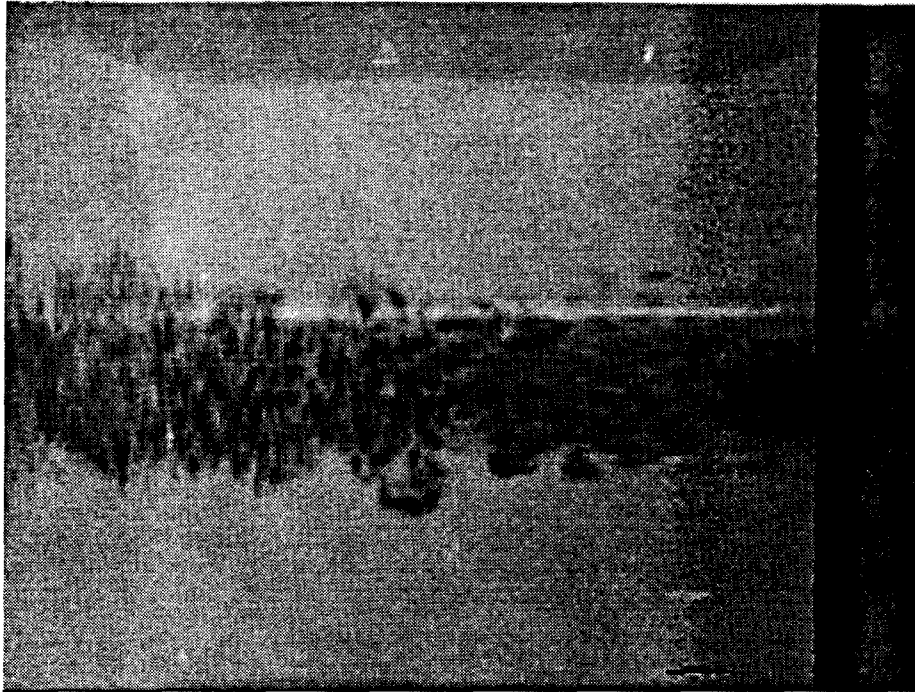


Figure 4.47 High Re, end view at $x = 4$ cm. Field of view is 4.5 cm.

BIBLIOGRAPHY

- Bohren, C.F. and Huffman, D.R. (1983) Absorption and Scattering of Light by Small Particles, New York: John Wiley and Sons, Inc.
- Bonnet, J. and Chaput, E. (1986). "Large-scale structures visualization in a high Reynolds number, turbulent flat plate wake at supersonic speed", Expts. in Fluids, vol. 4, pp. 350-356.
- Bonnet, J.P., Delville, J., Sapin, S., Sullivan, P., and Yeru, R. (1991). "Compressibility Effects in Turbulent Far Wakes", Eighth Symposium on Turbulent Shear Flows, Technical Univ. of Munich, September 9-11.
- Breidenthal, R. (1980). "Response of plane shear layers and wakes to strong three-dimensional disturbances", Phys. of Fluids, vol. 23, pp. 1929-1934.
- Breidenthal, R. (1992). "Sonic Eddy-A Model for Compressible Turbulence", AIAA Journal, vol. 30, pp. 101-104.
- Chen, Jacqueline H., Brian J. Cantwell, and Nagi N. Mansour (1989). "Direct Numerical Simulations of a Plane Compressible Wake: Stability, Vorticity Dynamics, and Topology", Report No. TF-46. Diss., Dept. of Mech. Eng., Stanford Univ.
- Clemens, Noel T. (1991) "An Experimental Investigation of Scalar Mixing in Supersonic Turbulent Shear Layers", HTGL Report No. T-274. Diss., Dept. of Mech. Eng., Stanford Univ.
- Clemens, N.T. and Mungal, M.G. (1991). "A planar Mie scattering technique for visualizing supersonic mixing flows", Expts. in Fluids, vol. 11, pp. 175-185.
- Clumpner, Joseph A. (1971). "Light Scattering from Ethyl Alcohol Droplets Formed by Homogeneous Nucleation", Journal of Chemical Physics, vol. 55, pp. 5042-5045.
- Demetriades, Anthony (1969). "Turbulent Mean-Flow Measurements in a Two-Dimensional Supersonic Wake", Physics of Fluids, vol. 12, pp. 24-32.

- Dutton, J. C., Herrin, J. L., Molezzi, M. J., Mathur, T., and Smith, K.M. (1995) "Recent Progress on High-Speed Separated Base Flows", AIAA paper 95-0472, 33rd Aerospace Sciences and Meeting Exhibit, Reno, Nevada, Jan. 9-12.
- Gasperas, G. (1989). "Transition Prediction for Two-Dimensional Viscous Supersonic Wakes", AIAA paper 89-0284, 27th Aerospace Sciences Meeting, Reno, Nevada, Jan. 9-12.
- Lachney, Eric R. (1995) "Two-Dimensional Temperature and Pressure Imaging of a Supersonic Flat Plate Wake", Master's Thesis, Dept. of Aerospace Eng., Univ. of Texas at Austin.
- Mieburg, E. and Lasheras, J.C. (1988). "Experimental and numerical investigation of the three-dimensional transition in plane wakes", J. Fluid Mech., vol. 190, pp. 1-37.
- Marks' Mechanical Engineering Handbook, 6th ed., New York: McGraw-Hill Book Company, Inc., 1958.
- Panton, Ronald L. Incompressible Flow. New York: John Wiley and Sons, Inc., 1984.
- Papamoschou, D. and Roshko, A. (1986). "Observations of Supersonic Free Shear Layers", AIAA paper 86-0162, 24th Aerospace Sciences Meeting, Reno, Nevada, 6-9 Jan.
- Saad, Michael A. Compressible Fluid Flow. Englewood Cliffs, New Jersey: Prentice-Hall, Inc., 1993.
- Sanders, Thomas (1994). "Side wall and Pitot pressure measurements of a Mach 3 turbulent wake", Report, Dept. of Aerospace Eng., Univ. of Texas at Austin.
- Wegener, Peter P., Clumpner, Joseph A., and Wu, Benjamin J.C. (1972). "Homogeneous Nucleation and Growth of Ethanol Drops in Supersonic Flow", Physics of Fluids, vol. 15, pp. 1869-1876.
- White, Frank M. Viscous Fluid Flow. New York: McGraw-Hill Inc., 1991